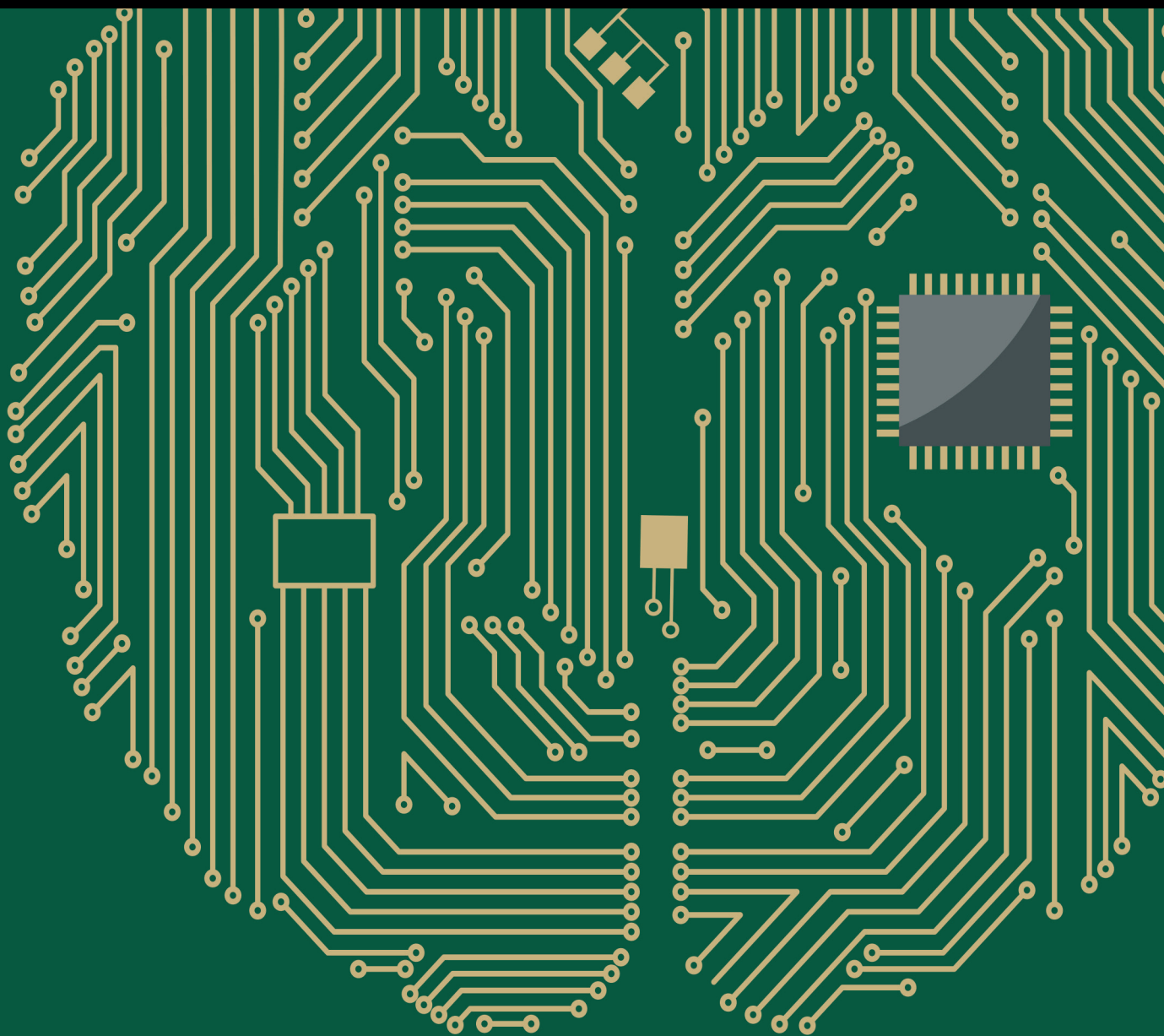


Computational Intelligence and Neuroscience

# Computational Intelligence and Neuroscience in Neurorobotics

Lead Guest Editor: Somyot Kaitwanidvilai

Guest Editors: Uma Seeboonruang, Hisayuki Aoyama, and Khemraj Emrith





---

# **Computational Intelligence and Neuroscience in Neurorobotics**

Computational Intelligence and Neuroscience

---

## **Computational Intelligence and Neuroscience in Neurorobotics**

Lead Guest Editor: Somyot Kaitwanidvilai

Guest Editors: Uma Seeboonruang, Hisayuki Aoyama,  
and Khemraj Emrith



---

Copyright © 2019 Hindawi. All rights reserved.

This is a special issue published in “Computational Intelligence and Neuroscience.” All articles are open access articles distributed under the Creative Commons Attribution License, which permits unrestricted use, distribution, and reproduction in any medium, provided the original work is properly cited.

## Editorial Board

Ricardo Aler, Spain  
Amparo Alonso-Betanzos, Spain  
Pietro Aricò, Italy  
Hasan Ayaz, USA  
Sylvain Baillet, Canada  
Roman Bartak, Czech Republic  
Theodore W. Berger, USA  
Daniele Bibbo, Italy  
Vince D. Calhoun, USA  
Francesco Camastra, Italy  
Michela Chiappalone, Italy  
Andrzej Cichocki, Japan  
Jens Christian Claussen, UK  
Silvia Conforto, Italy  
António D. P. Correia, Portugal  
Justin Dauwels, Singapore  
Christian W. Dawson, UK  
Carmen De Maio, Italy  
Sergio Decherchi, Italy  
Paolo Del Giudice, Italy  
Maria Jose del Jesus, Spain  
Arnaud Delorme, France  
Thomas DeMarse, USA  
Anastasios D. Doulamis, Greece  
Steven L. Fernandes, USA  
Juan Carlos Fernández, Spain  
Piotr Franaszczuk, USA  
Leonardo Franco, Spain  
Paolo Gastaldo, Italy  
Samanwoy Ghosh-Dastidar, USA  
Manuel Graña, Spain  
Rodolfo E. Haber, Spain  
Dominic Heger, Germany  
Stephen Helms Tillery, USA  
J. A. Hernández-Pérez, Mexico  
Luis Javier Herrera, Spain  
Etienne Hugues, USA  
Ryotaro Kamimura, Japan  
Pasi A. Karjalainen, Finland  
Elpida Keravnou, Cyprus  
Raşit Köker, Turkey  
Dean J. Krusienski, USA  
Fabio La Foresta, Italy  
Antonino Laudani, Italy  
Maciej Lawrynczuk, Poland  
Mikhail A. Lebedev, USA  
Cheng-Jian Lin, Taiwan  
Giosuè Lo Bosco, Italy  
Ezequiel López-Rubio, Spain  
Bruce J. MacLennan, USA  
Reinoud Maex, Belgium  
Kezhi Mao, Singapore  
Sergio Martinoia, Italy  
Laura Marzetti, Italy  
Elio Masciari, Italy  
Paolo Massobrio, Italy  
Gerard McKee, Nigeria  
Michele Migliore, Italy  
Paulo Moura Oliveira, Portugal  
Debajyoti Mukhopadhyay, India  
Klaus Obermayer, Germany  
Karim G. Oweiss, USA  
Massimo Panella, Italy  
Fivos Panetsos, Spain  
David M Powers, Australia  
Sandhya Samarasinghe, New Zealand  
Saeid Sanei, UK  
Friedhelm Schwenker, Germany  
Victor R. L. Shen, Taiwan  
Fabio Solari, Italy  
Jussi Tohka, Finland  
Carlos M. Travieso-González, Spain  
Lefteri Tsoukalas, USA  
Pablo Varona, Spain  
Roberto A. Vazquez, Mexico  
Meel Velliste, USA  
Mario Versaci, Italy  
Francois B. Vialatte, France  
Thomas Villmann, Germany  
Ivan Volosyak, Germany  
Cornelio Yáñez-Márquez, Mexico  
Michal Zochowski, USA  
Rodolfo Zunino, Italy

# Contents

---


## **Computational Intelligence and Neuroscience in Neurorobotics**

Somyot Kaitwanidvilai , Uma Seeboonruang, Hisayuki Aoyama, and Khemraj Emrith  
Editorial (2 pages), Article ID 6506802, Volume 2019 (2019)


## **A Thought-Operated Digital Random-Access Memory**

Lee Ben-Ami and Ido Bachelet   
Research Article (8 pages), Article ID 9684140, Volume 2019 (2019)



## **Coevolution of the Asymmetric Morphology and the Behaviour of Simple Predator Agents in Predator-Prey Pursuit Problem**

Milen Georgiev , Ivan Tanev, and Katsunori Shimohara  
Research Article (15 pages), Article ID 1538757, Volume 2019 (2019)






## **Discrimination of Motion Direction in a Robot Using a Phenomenological Model of Synaptic Plasticity**

Nareg Berberian , Matt Ross, and Sylvain Chartier  
Research Article (14 pages), Article ID 6989128, Volume 2019 (2019)



## **Spatial Concept Learning: A Spiking Neural Network Implementation in Virtual and Physical Robots**

André Cyr  and Frédéric Thériault   
Research Article (8 pages), Article ID 8361369, Volume 2019 (2019)



## **Control of a Humanoid NAO Robot by an Adaptive Bioinspired Cerebellar Module in 3D Motion Tasks**

Alberto Antonietti , Dario Martina , Claudia Casellato , Egidio D'Angelo ,  
and Alessandra Pedrocchi   
Research Article (15 pages), Article ID 4862157, Volume 2019 (2019)

## **Neurofuzzy c-Means Network-Based SCARA Robot for Head Gimbal Assembly (HGA) Circuit Inspection**

Somyot Kiatwanidvilai  and Rawinun Praserttaweelap   
Research Article (10 pages), Article ID 4952389, Volume 2018 (2019)

## **Multilayer Hybrid Deep-Learning Method for Waste Classification and Recycling**

Yinghao Chu , Chen Huang, Xiaodan Xie, Bohai Tan, Shyam Kamal , and Xiaogang Xiong   
Research Article (9 pages), Article ID 5060857, Volume 2018 (2019)

## Editorial

# Computational Intelligence and Neuroscience in Neurorobotics

**Somyot Kaitwanidvilai** <sup>1</sup>, **Uma Seeboonruang**<sup>1</sup>, **Hisayuki Aoyama**<sup>2</sup>, and **Khemraj Emrith**<sup>3</sup>

<sup>1</sup>King Mongkut's Institute of Technology Ladkrabang (KMITL), Bangkok, Thailand

<sup>2</sup>The University of Electro-Communications, Tokyo, Japan

<sup>3</sup>University of West of England, Bristol, UK

Correspondence should be addressed to Somyot Kaitwanidvilai; [somyot.ka@kmitl.ac.th](mailto:somyot.ka@kmitl.ac.th)

Received 15 May 2019; Accepted 16 May 2019; Published 1 July 2019

Copyright © 2019 Somyot Kaitwanidvilai et al. This is an open access article distributed under the Creative Commons Attribution License, which permits unrestricted use, distribution, and reproduction in any medium, provided the original work is properly cited.

Computational intelligence and neuroscience play an important role in robotics applications to improve the robot's capacities not only in increasing productivity in manufacturing but also in intelligence development so that robots can substitute human's thinking and planning capacity. Recently, neuroscience has been applied to robots to generate intelligence models with biological nervous systems. The intersection between robotics and neuroscience highlights many promising approaches and applications, for example, the neurorobots, brain-inspired algorithms and devices in robotics, and neural network-based navigation. AI leads to one of the most significant paradigm shifts and improvements in the robotics field. The principal aim of this special issue is to publish quality papers of new developments and trends, novel techniques, and innovative methodologies on the theories and applications of computational intelligence and neuroscience in robotics. Potential topics include but are not limited to the followings: neural networks for biological and biomedical robots, neuroinspired robot navigation, decision support systems in neurorobotics, intelligent fault detection and identification in neurorobotics, clustering and data analysis in neurorobotics, swarm robotics based on neural networks, and neurofuzzy control design for cooperative robots. The following paragraphs summarize the main contents of the best novelty research papers published in this special issue.

The paper "Coevolution of the Asymmetric Morphology and the Behaviour of Simple Predator Agents in Predator-Prey Pursuit Problem" by M. Georgiev, I. Tanev, and K. Shimohara concentrates on the one of the previous challenges. It introduced a new standpoint to the well-studied

predator-prey pursuit problem using an implementation of straightforward predator agents. Genetic algorithm was implemented that results in a successful capture of the prey by the team of predator agents. The results were considered towards the engineering of asymmetric small-scale for delivery of medicine, locating and destroying cancer cells, microscopic imaging, etc.

The paper "Discrimination of Motion Direction in a Robot Using a Phenomenological Model of Synaptic Plasticity" by N. Berberian, M. Ross, and S. Chartier examines the possibility of implementation of a bioinspired model of synaptic plasticity in a robotic agent to allow the discrimination of motion direction of real-world stimuli. The research started with a well-established model of short-term synaptic plasticity (STP), and then the development of a microcircuit motif of spiking neurons capable of exhibiting preferential and nonreferential responses to changes in the direction of an orientation stimulus in motion was introduced. Overall, the model presented the STP function in describing the direction selectivity and applied these in an actual robot to validate the response characteristics in experimental direction selectivity.

The paper "Spatial Concept Learning: A Spiking Neural Network Implementation in Virtual and Physical Robots" by A. Cyr and F. Thériault proposes an artificial spiking neural network (SNN). The SNN sustained the cognitive abstract process of spatial concept learning and embedded in virtual and real robots. The results showed that the robots can learn the relationship of horizontal/vertical and left/right visual stimuli. Tests with novel patterns and locations were effectively completed after the acquisition learning phase. The

results also presented that the SNN can change its behavior in real time when the rewarding rule changes.

The paper “Control of a Humanoid NAO Robot by an Adaptive Bioinspired Cerebellar Module in 3D Motion Tasks” by A. Antonietti et al. focuses on a bioinspired adaptive model by a spiking neural network made of thousands of artificial neurons to control a humanoid NAO robot in real time. The model moved forward and encoded as spikes. The generated spiking activity of its output neurons was decoded in order to yield the suitable correction on the motor actuators. With different time scales, three bi-directional long-term plasticity rules have been embedded for different connections. The neurorobot successfully learned how to compensate for the external perturbation generating an appropriate correction during the perturbed upper limb reaching protocol. Hence, the spiking cerebellar model was able to duplicate in the robotic platform how biological systems deal with external sources of error.

The paper “Neurofuzzy c-Means Network-Based SCARA Robot for Head Gimbal Assembly (HGA) Circuit Inspection” by S. Kaitwanidvilai and R. Praserttaweelap describes a decision and control of SCARA robot in HGA (head gimbal assembly) inspection. The method applied a general image processing technique, blob analysis, in conjunction with neurofuzzy c-means (NFC) clustering with the branch and bound (BNB) technique in order to find the best structure in all possible candidates to increase the performance of the entire system. The results from two clustering techniques were investigated to show the effectiveness of the proposed algorithm. Training results from the 30x microscope inspection with 300 samples showed that the best accuracy for clustering was 99.67% from the NFC clustering and for testing results showing 92.21% accuracy for the conventional Kohonen network. This system has been implemented successfully in the HDD production line at Seagate Technology (Thailand) Co. Ltd.

The paper “Multilayer Hybrid Deep-Learning Method for Waste Classification and Recycling” by Y. Chu et al. studied a multilayer hybrid deep-learning system (MHS) to automatically sort waste disposed by individuals in the urban municipal area. This system deployed a high-resolution camera capturing waste image and sensors to detect another useful feature information. The MHS used a CNN-based algorithm to remove image features and a multilayer perceptrons (MLP) method to consolidate image features and other feature information to classify wastes as recyclable or the others. The results presented the overall classification accuracy higher than 90% under two different testing scenarios. This significantly outperformed a reference CNN-based method relying on image-only inputs.

In summary, these six papers have showed the actively practical research topics in Computational Intelligence and Neuroscience in Neurorobotics. We thank all authors for submitting their papers to this special issue and recognize all reviewers for providing their expertise review and excellent comments. We hope that all papers in this special issue would contribute to the research ideas and methodology development in the related fields.

## Conflicts of Interest

We declare that there are no conflicts of interest.

## Acknowledgments

We are grateful to the editors and Prof. Hisayuki Aoyama, University of Electro-Communication, Tokyo, Japan, for hosting this special issue and their significant support during the editorial process.

*Somyot Kaitwanidvilai  
Uma Seeboonruang  
Hisayuki Aoyama  
Khemraj Emrith*



## Research Article

# A Thought-Operated Digital Random-Access Memory

Lee Ben-Ami<sup>1,2,3</sup> and Ido Bachelet <sup>1</sup>

<sup>1</sup>*Augmanity, Rehovot, Israel*

<sup>2</sup>*Faculty of Life Sciences, BIU, Ramat Gan, Israel*

<sup>3</sup>*Gonda Brain Centar, BIU, Ramat Gan, Israel*

Correspondence should be addressed to Ido Bachelet; [dogbach@gmail.com](mailto:dogbach@gmail.com)

Received 25 September 2018; Revised 23 February 2019; Accepted 15 April 2019; Published 9 June 2019

Guest Editor: Somyot Kiatwanidvilai

Copyright © 2019 Lee Ben-Ami and Ido Bachelet. This is an open access article distributed under the Creative Commons Attribution License, which permits unrestricted use, distribution, and reproduction in any medium, provided the original work is properly cited.

The capacity and reliability of biological memory could be exceeded by a constantly growing flux of information to remember and operate by. Yet, our memory is fragile and could be easily impaired, and the prevalence of memory disorders is increasing in correlation with the population's mean age. As expected, auxiliary memory devices (such as writing pads and computers) are abundant but are operated indirectly using significant effort compared with biological memory. We report a working prototype of a simplified, 4 KB random-access memory (RAM) that can be written to or read from using thought and could be embedded more seamlessly than other artificial memory aids. The system analyses EEG signals to extract attention levels, which trained subjects can use to write messages into an RFID sticker, or read from it on a display. We describe basic modes of using memory by a single subject, emulate common forms of social communication using this system, and highlight new forms of social usage and allocation of memories that are linked to specific persons. This preliminary prototype highlights the technical feasibility and the possibilities of implantable thought-operated memory devices and could be developed further to provide seamless aid to people suffering from memory disorders in the near future.

## 1. Introduction

Our ability to store and retrieve information is critical for learning, social interaction, and experience and hence for our survival [1]. However, it is also a fragile faculty and could be damaged or lost relatively easily. Memory disorders and dementia, which are hallmarks of medical conditions ranging from mild cognitive impairment (MCI) to Alzheimer's disease (AD), are a significant problem which is growing steadily [2–4], for which treatment is extremely limited and inadequate [5]. Our ability to create short-term or long-term memories could be severely damaged by head trauma, infarcts, diseases, and even the side effects of certain drugs [6].

On the other hand, biological memory could be assisted by simple means such as external documentation, e.g., by writing and audio recording. However, two challenges could be anticipated. First, the amount of information that we come across and are required to remember properly is constantly increasing, for example, the number of individuals that we

need to maintain direct contact with. Excessive flow of information could hinder the task of indirectly documenting this information. Second, auxiliary memory devices such as a notebook or mobile phone could be easily lost, stolen, or damaged and are thus of limited reliability. Information can be stored on a database which is accessible everywhere, such as a cloud, but this access requires network connectivity, which is still largely limited and discontinuous.

We could therefore envision an auxiliary memory device which is direct, in order to allow seamless documentation and retrieval of information, and has the ability to be embedded or implanted, as to reduce the chances for random loss of the memory stored on it. Such auxiliary memory could function in parallel to our native capacity to remember as a backup or failsafe system that comes into action when needed.

Comparison to other studies of artificial memory devices shows prototypes like the implanted silicon chip in the work of Berger et al. [7] that was implanted in rats and monkeys

and can process information similar to actual neurons. This chip does not store data but can serve as a prosthesis for a damaged part in the hippocampus. Another surgical implant used for patients with hearing disabilities is the Cochlear implant which provides a sense of sounds with an electric device stimulating the auditory nerve [8]. This device does not store or share data but is used to convert sound waves into an electrical stimulus of the nerve. Another study was done by Sum-Gyun Yi et al. which fabricated MoS<sub>2</sub>-based flash memory devices by stacking MoS<sub>2</sub> and hexagonal boron nitride (hBN) layers on an hBN/Au substrate and demonstrated that these devices can emulate various biological synaptic functions, including potentiation and depression processes, spike-rate-dependent plasticity, and spike-timing dependent plasticity [9]. This fabricated memory mimics the work of a synapse in a specific brain. These studies represent a variety of implant studies in the field of implants regarding memory or neural abilities. All are invasive and do not store or share data.

Another era of study deals with how psychology works or cultures created collective memory in history. These studies argue on humans' abilities to work together and using language as a mean of collaboration [10, 11]. These studies are theoretical and do not implement but show how we, as humans, collaborate and create more by using this ability.

The creation of the Internet, the cloud of data, and the Internet of things (IOT) enhance our ability to communicate wildly and store and retrieve data massively while wearing communicating devices that can monitor, store, and send data between devices and through the Internet [12, 13]. The need to help memory disabilities and IOT open the ability to create new methods of storing memory and sharing it with others thus helping and enhancing human capabilities.

In this study, we aim to do so with a new and preliminary artificial memory prototype.

Our purpose in this study was to outline and demonstrate a working prototype of such memory device. To this end, we used simple components which were wired as depicted in Figure 1(a). A commercially available headset was used to acquire EEG signals from human subjects, and a custom-written algorithm was used to extract the level of attention exhibited by each subject as previously described [14]. A controller recorded and analyzed the data in real time, and communicated with a "memory," based on a simple RFID tag, which was stuck on the subject's neck (Figure 1(b)). Based on their level of attention, the controller carried out one of four functions: none, write 0, write 1, or read. In the terms of this demonstration, the controller is a computer capable of communicating with the RFID tag, writing bits to it, and displaying its content, e.g., as simple text. The system here has been implemented using either commercially available Arduino parts, or a standard laptop computer.

There are several types of RFID tags [15], namely, passive, active, and semi active. In our experiment, we used a passive sticker that can be activated and communicated only by a near electric field. Moreover, there are different tags and protocols of near field communication (NFC). Here, we used

a MIFARE Classic ISO/IEC 14443 Type A standard which enables 4 KB memory divided to 16 sectors. Every sector holds 4 blocks of 32 hexadecimal memory digits. The first block of every sector holds a 6-digit security key ( $16^6$  options) that prevents access to the data and prevents reading or writing if it is incorrect, providing a layer of security to the communication between the controller and the memory [16].

Moreover, there are different types of RFID frequencies, the lower frequency 125/134.2 kHz is useful up to 30 cm and can create distance security; however, it is less optimal for longer distances. Frequencies of 868/959 MHz (UHF) or 2400 MHz can give longer distance abilities (3 to 100 m) [17]. In our experiment, we used a 13.56 MHz RFID circuit, which supports communication at up to 1 m.

## 2. Methods

**2.1. Subjects.** For this study, 9 subjects (5 women, 4 men, ages 18–43, average age  $31.7 \pm 10.9$  years,  $\sigma^2$  118.27) were recruited. We chose controlling attention levels since it is a parameter that is well researched and tested in EEG data and already used in other works. There are some hardware and applications that already use it in different ways like computer games or for research [14, 18, 19]. The reason for the four ranges is to create different letters and mode in a language of two digits (0/1) and to differ between read, write, and no request at all as explained in Figure 1. First, each subject underwent a short (average ~15 min) phase of training of the system until they were able to achieve specific attention of one of four levels. These levels were defined based on a scale of 0–100% attention, and each was used to code a specific function: 0–29% read from memory, 30–59% baseline for "no action" and to differ between reading and writing, 60–79% write "0" to memory, and 80–100% write "1" to memory. Each subject was allowed to achieve her/his own speed in switching between attention levels, with an average of  $3.5 \pm 1.2$  s spent at each level at the end of the training phase. Attention levels defining the ends of the scale were achieved by experiencing passive activity versus a difficult mathematical problem as previously described [14, 18, 19]. In the testing phase, the subjects were requested to read or write 0/1 by achieving the desired level of attention described above. The study design was reviewed and approved by the Institutional Review Board at Bar-Ilan University. All methods were performed in accordance with the relevant guidelines and regulations. Informed consent was obtained from all subjects prior to participating in this study.

**2.2. Hardware and Software.** EEG data were acquired using a Neurosky *Mindwave mobile plus* kit headset that provides raw-sampled wave values (128 Hz or 512 Hz, depending on hardware), signal quality metrics, eSense attention meter values (0 to 100), and EEG band power values for delta, theta, alpha, beta, and gamma.

EEG signals were obtained from neurosky mobile algorithm analysis. The Attention meter algorithm (eSens) indicates the intensity of mental "focus" or "attention." The

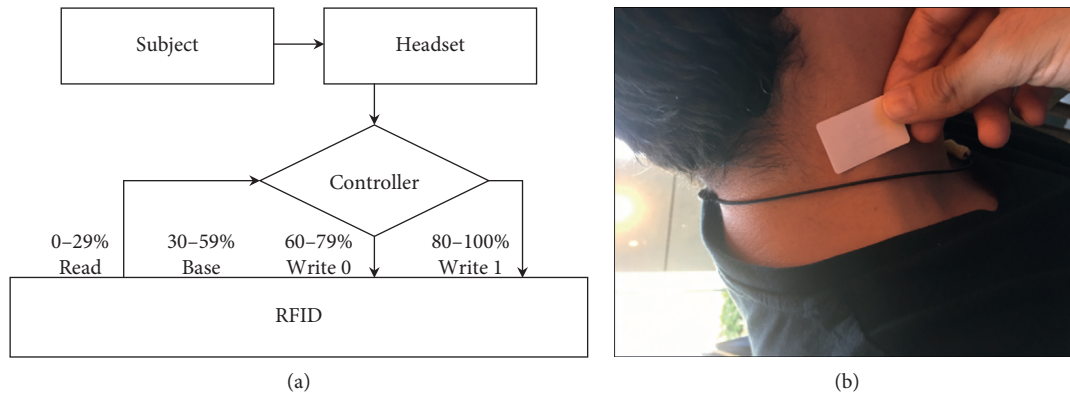


FIGURE 1: Description of the system used in this study. (a) Schematic representation. An EEG headset was used to directly acquire EEG data from the subjects. The EEG was processed and classified on a controller connected to the RFID memory circuit. Based on the attention levels measured from the subject, the controller performed a specific function on the memory: read memory content (0%–29%), no action (30–59%), write 0 (60–79%), or write 1 (80–100%). (b) The RFID memory chip as a sticker on one of the subjects of this study.

value ranges from 0 to 100. The attention level increases when a user focuses on a single thought or an external object and decreases when distracted. Users can observe their ability to concentrate using the algorithm. In educational settings, attention to lesson plans can be tracked to measure their effectiveness in engaging students. In gaming, attention has been used to create “push” control over virtual objects.

eSense Attention meter indicates the intensity of a user’s level of mental “focus” or “attention,” such as that which occurs during intense concentration and directed (but stable) mental activity. Its value ranges from 0 to 100. Distractions, wandering thoughts, lack of focus, or anxiety may lower the Attention meter level. For each different type of eSense (i.e., Attention and Meditation), the meter value is reported on a relative eSense scale of 1 to 100. On this scale, a value between 40 and 60 at any given moment in time is considered “neutral” and is similar in notion to “baselines” that are established in conventional brainwave measurement techniques (though the method for determining a Think-Gear baseline is proprietary and may differ from other methods). A value from 60 to 80 is considered “slightly elevated” and may be interpreted as levels tending to be higher than normal (levels of Attention or Meditation that may be higher than normal for a given person). Values from 80 to 100 are considered “elevated,” meaning they are strongly indicative of heightened levels of that eSense. Similarly, on the other end of the scale, a value between 20 and 40 indicates “reduced” levels of the eSense, while a value between 1 and 20 indicates “strongly lowered” levels of the eSense. These levels may indicate states of distraction, agitation, or abnormality, according to the opposite of each eSense [20].

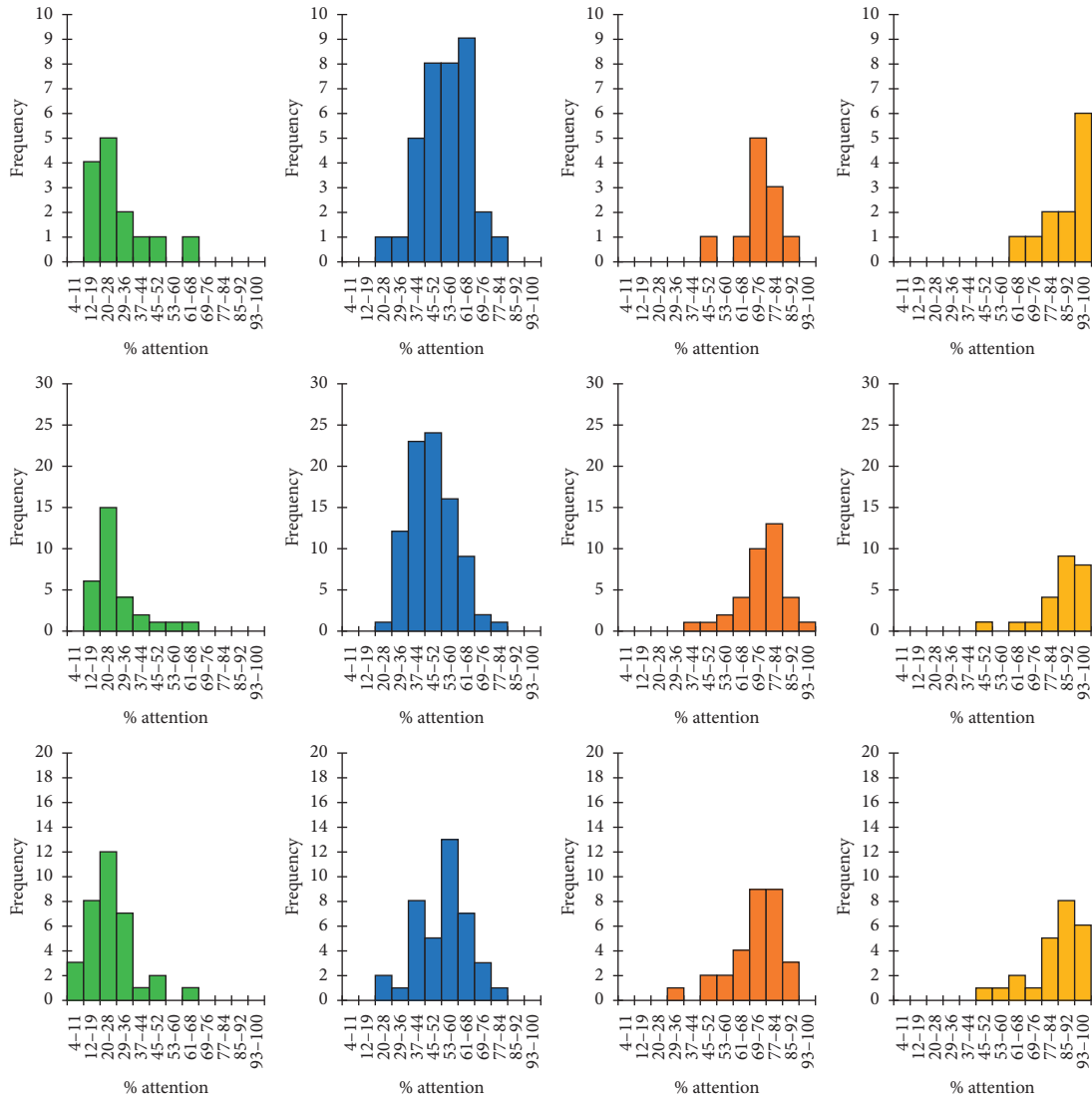
The signals were broadcast via Bluetooth to a controller for processing and classification. We used an *Arduino Uno* device connected to *BlueSMiRF silver* Bluetooth antenna, which translated the signals from the mindwave mobile headset device using a custom-written code. To process and classify the signals, an additional code was written using Arduino language (based on C/C++). The base program handles the Attention signals and determines the levels to

classify. An NFC (near field Communication) Reading/Writing antenna shield (13.56 MHz band) was connected to the controller. A *Mifare classic* RFID tag with a 4 KB memory storage was used to store the data written or to broadcast the data when reading. Arduino and NFC antenna shields were connected to a DELL I5–4200U (2.3 GHz/4 GB RAM) laptop with windows 7 operating system which was used as display monitor.

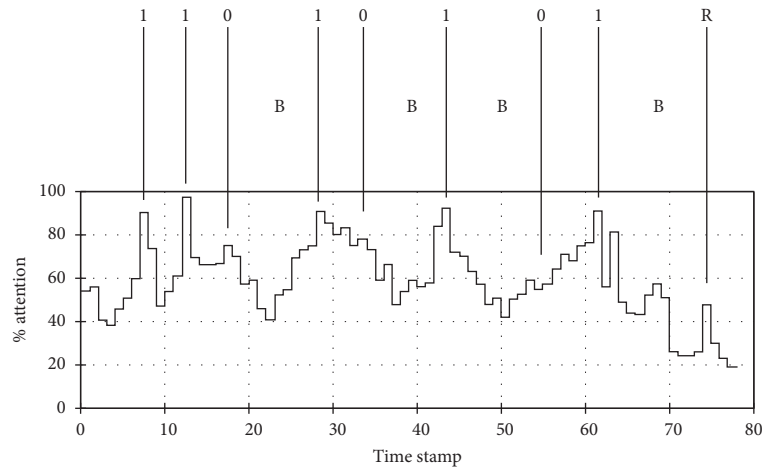
### 3. Results

Most subjects were capable of achieving desired levels of attention to be able to perform reading and writing 0/1 tasks and in a reproducible manner (Figure 2(a)). Subjects typically returned to baseline after 1 or 2 writing actions (either write 0 or write 1) and were able to maintain a maximum of 3 writing actions without returning to baseline (Figure 2(b)). Analysis of the transitions between attention levels revealed that all subjects were capable of switching rapidly between levels, achieving a velocity of up to ~80% per second, but these transitions became slower with time (Figure 2(c)), eventually reaching a maximum velocity of 5% per second after 60 seconds of writing onto the memory. Interestingly, the ability to maintain transition efficiency did not correlate with subject age, as hypothesized at an early stage of this study, bolstering the role of training in subject performance (Figure 2(d)). Only 25% of the messages were written without incorrect bits, with most messages having 1 incorrect bit (Figure 2(e)). No bias to a specific error bit (0 or 1) was found despite the unequal allocation of attention levels to the different bits.

We used the system to investigate the possibility for social communication between individuals, mediated by writing to and reading from neighboring memories. Social communication presents a prevalent framework of communication (e.g., social networks accessed via mobile devices), which we aimed to emulate using our system. Our basic purpose was to show that the system not only supports common modes of social networking, but also allows new concepts for using memory.



(a)



(b)

FIGURE 2: Continued.

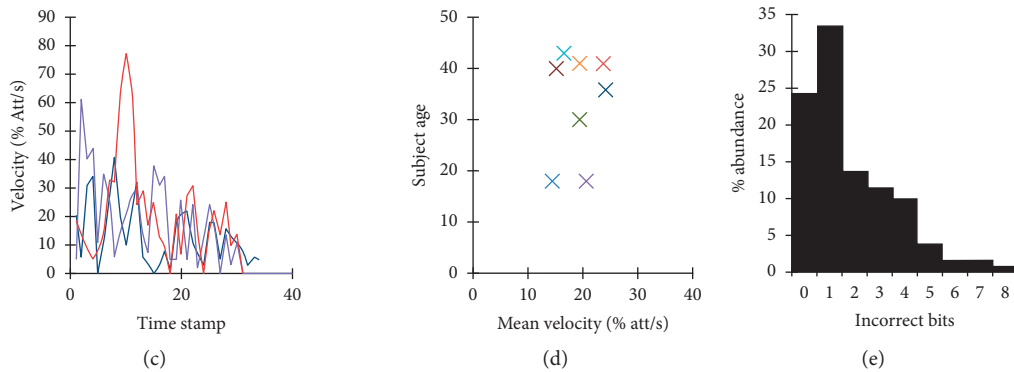


FIGURE 2: Performance of the thought-operated memory device. (a) Performance histograms of 3 representative subjects, summarizing their ability to achieve and maintain a specific attention level during 10 writing and reading tasks (green = read, blue = no action, orange = write 0, yellow = write 1); vertical coordinate, Frequency, indicates the number of times a subject reached a certain attention level; horizontal coordinate, Attention, indicates the level of attention reached divided to sections (4–11, 12–19, 20–28, 29–36, 37–44, 45–52, 53–60, 61–68, 69–76, 77–84, 85–92, 93–100). (b) A representative memory task. Here, the subject was asked to write onto her memory the string “11010101” and then read it. This specific task was carried out without errors (25% of all tasks were error-free). (c) Velocity analysis from 3 representative short tasks, showing the transition between attention levels slowing down with time. (d) A plot of mean velocity vs. subject age, showing no correlation between these parameters. (e) Analysis of the abundance of errors in writing tasks, showing that ~25% of the tasks were error-free, and ~33% of the tasks had 1 incorrect bit.

In the first series of tests described above, the basic mode of operation of this device was studied: subject A writes to A (same subject) → A reads from A (Figure 3(a)). Subsequently, two subjects (generically termed Bob and Mary) used the system to write a message from Bob to Mary, by having Bob write to Mary’s memory and Mary reading from her Memory (Figure 3(b)), and to emulate “mind reading,” by having Bob write to his own memory and Mary reading from Bob’s memory (Figure 3(c)). These tests were handled and discussed to emphasize the potential of this work not only to store and retrieve self-memory data but in order to share memories between subjects as well. Bob reading and writing his own memory is a self-memory method. Mary reading from Bob’s memory enables memory sharing from Bob’s memory to Mary’s.

Other modes that the system can support, although not investigated here, are sharing of memories between subjects (Figure 3(d)) or from a single person to a public (Figure 3(e)), two modes that are enabled in typical social networks today; however the system also supports the outsourcing of another person’s memory (Figure 3(e)), which is not a standard social networking mode. Further designs are now being tested in our laboratory that implement different compartments, accessible by authorized individuals other than the one to whom the memory is linked, which support private allocation of information for memory outsourcing.

Although the specifications were defined arbitrarily in this system (e.g., attention levels, free pace and duration between actions), similar measurements could theoretically be made in other configurations. However, several principles were implemented in this particular design. First, the attention levels were nearly evenly distributed across the complete scale. Second, the writing actions were clustered together to enable rapid transition between them. Third, writing and reading actions were separated by the baseline

range. Our findings show that the first and third principles were important in achieving reproducibility and a flowing writing uninterrupted by reading, but the second principle was less successful in ensuring that writing was not interrupted by baseline phases.

#### 4. Discussion

The prototype described here is extremely preliminary in the sense that it is motivated by seamless embedding of memory without being seamless in itself. However, this is a technical barrier that is being tackled, or has been tackled successfully in some cases. RFID circuits such as the one used here are completely implantable [15, 21–23], and their interference with existing devices such as pacemakers has been studied [22]. The portability of other components of the system is being improved towards complete implants, or at least wearable or in patch form. EEG measurements themselves could be made using sensor pads or implantable sensors [24–27], eliminating the need for a carried EEG headset. Display of the content that is retrieved from the memory could be done by means of contact lens [28, 29], or, less directly, on glasses such as Google glass. Eventually, a system similar to the one described here could be entirely implantable. Moreover, the capacity of 4 KB implemented here could certainly be increased in future designs.

The specific method of writing and reading from the device could be improved. Attention is a parameter that can be readily extracted from raw EEG signals [14, 18, 19], and our observations show that trained subjects could switch between desired levels of attention sufficiently for the system to recognize the appropriate function to be carried out. However, most (~75%) messages contained at least 1 incorrect bit. This suggests that either there is a better parameter to guide the system by or that the short training provided in this study was not sufficient. Further

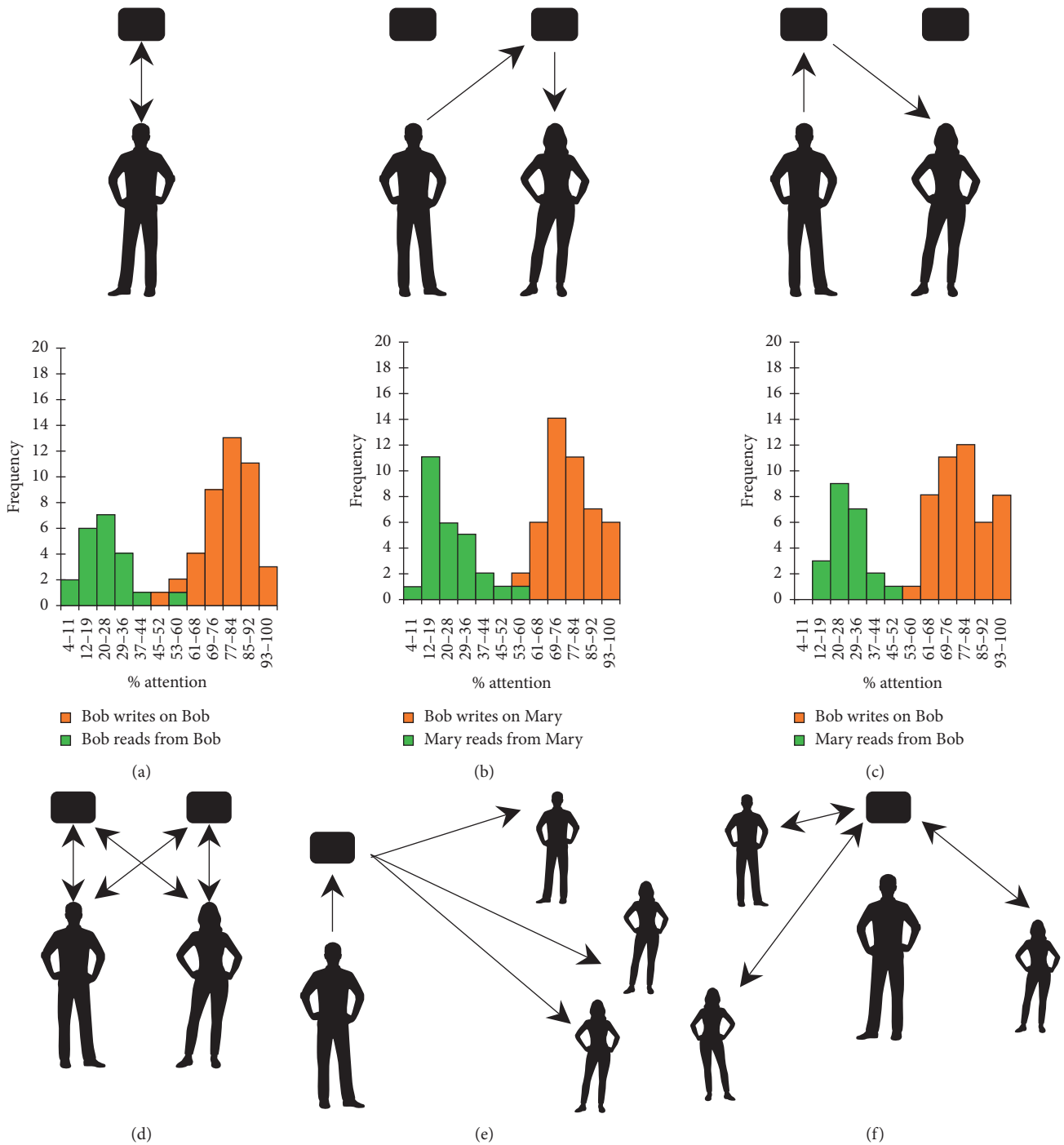


FIGURE 3: Social communication emulated with the memory device. (a–c) Three operation modes, top panels show schematic representation of the network, with histogram overlays below summarizing the reading and writing (both 0 and 1) performance achieved by the subjects during 10 tasks. Black rectangles represent memory devices. Arrow directions represent writing (arrow leading from person to device) or reading (arrow leading from device to person). (a) The basic mode of operation where same subject writes on his/her own memory and reads from it. (b) Two subjects, nicknamed Bob and Mary, emulating social communication. Bob writes onto Mary’s device, and Mary reads from her device. (c) Bob writes onto his own device, and Mary reads this content from her device. (d–f) Potential modes of social usage of the memory device described here. (d) Complete sharing of memories between two subjects; (e) sharing memories from a person’s memory to a public; and (f) a public authorized to use another person’s memory by means of outsourcing.

experiments are underway to investigate additional parameters within EEG data that could be used and to evaluate the potential precision of their utilization.

Implantable memory devices raise their own issues of privacy, possibilities for unauthorized reading, and inadvertent manipulation. Physical proximity, as required in

the described prototype, is an important protective factor but limits the social applications of such devices. To enable the full scale of uses, implantable memory devices should be designed with specific layers of security addressing these special challenges, such as interference from adjacent devices and other implants and potential attacks made against the person through the implanted device.

Comparing this work with other artificial memory devices introduced earlier shows the potential of a noninvasive prototype that can be used to store and share data between 2 or more persons and to use one mind or more as a “cloud” similar to sharing thoughts and memories in social networks or the Internet today. The ability to communicate in a standard network like NFC described here may offer a connection to other devices and may correlate to other languages in future work. In contrast, converting this prototype to an invasive one as other introduced implants may give other abilities of extending human memory and brain capacity capabilities that were not found in today’s implants [30].

### Data Availability

The data used to support the findings of this study are available from the corresponding author upon request.

### Conflicts of Interest

The authors declare no potential conflicts of interest.

### Authors’ Contributions

LBA performed experiments. LBA and IB designed the research, analyzed the data, and wrote the manuscript.

### Acknowledgments

The authors wish to thank Jonathan Giron and Prof. Eitan Okun for valuable assistance and discussions.

### References

- [1] M. W. Eysenck and M. Brysbaert, *Fundamentals of Cognition*, Routledge, London, UK, 2018.
- [2] R. O. Roberts, D. S. Knopman, M. M. Mielke et al., “Higher risk of progression to dementia in mild cognitive impairment cases who revert to normal,” *Neurology*, vol. 82, no. 4, pp. 317–325, 2013.
- [3] A. Burns and S. Iliffe, “Dementia,” *BMJ*, vol. 338, no. 1, p. b75, 2009.
- [4] D. S. Knopman, R. O. Roberts, V. S. Pankratz et al., “Incidence of dementia among participants and nonparticipants in a longitudinal study of cognitive aging,” *American Journal of Epidemiology*, vol. 180, no. 4, pp. 414–423, 2014.
- [5] World Health Organization, *Dementia: A Public Health Priority*, World Health Organization, Geneva, Switzerland, 2012.
- [6] B. L. Strom, R. Schinnar, J. Karlawish et al., “Statin therapy and risk of acute memory impairment,” *JAMA Internal Medicine*, vol. 175, no. 8, pp. 1399–1405, 2015.
- [7] T. W. Berger and D. L. Glanzman, *Toward Replacement Parts for the Brain Implantable Biomimetic Electronics as Neural Prostheses*, A Bradford Book The MIT Press Cambridge, Cambridge, MA, USA, 2005.
- [8] F.-G. Zeng, S. Rebscher, W. Harrison, X. Sun, and H. Feng, “Cochlear implants: system design, integration, and evaluation,” *IEEE Reviews in Biomedical Engineering*, vol. 1, pp. 115–142, 2008.
- [9] S.-G. Yi, M. U. Park, S. H. Kim et al., “Artificial synaptic emulators based on MoS<sub>2</sub> flash memory devices with double floating gates,” *ACS Applied Materials & Interfaces*, vol. 10, no. 37, pp. 31480–31487, 2018.
- [10] C. Alon, “Collective memory and cultural history: problems of method,” *American Historical Review*, vol. 102, no. 5, pp. 1386–1403, 1997.
- [11] W. Hirst and G. Echterhoff, “Toward a psychology of collective memory,” *Collective Memory and Collective Identity*, vol. 75, no. 1, pp. 183–216, 2008.
- [12] D. M. Wegner and A. F. Ward, *The Internet Has Become the External Hard Drive for Our Memories*, *Scientific American*, 2013.
- [13] R. Minerva, A. Biru, and D. Rotondi, *Towards a Definition of the Internet of Things (IoT)*, 2015.
- [14] S. Arnon, N. Dahan, A. Koren et al., “Thought-controlled nanoscale robots in a living host,” *PLoS One*, vol. 11, Article ID e0161227, 2016.
- [15] V. Kumar, “Implantable RFID chips,” in *The Future of Identity in the Information Society*, vol. 262, pp. 151–157, Springer, Boston, MA, USA, 2008.
- [16] K. T. Huang, “Secured RFID mutual Authentication scheme for Mifare systems,” *International Journal of Network Security & Its Applications*, vol. 4, no. 6, pp. 17–31, 2012.
- [17] D. Paret, *RFID at Ultra and Super High Frequencies: Theory and Application*, John Wiley & Sons, Hoboken, NJ, USA, 2009.
- [18] B. Hamadicharef, “Learning EEG-based spectral-spatial patterns for attention level measurement,” *IEEE Xplore*, 2009.
- [19] N.-H. Liu, C.-Y. Chiang, and H.-C. Chu, “Recognizing the degree of human attention using EEG signals from mobile sensors,” *Sensors*, vol. 13, no. 8, pp. 10273–10286, 2013.
- [20] MindWave Mobile: User Guide, 2017.
- [21] Z. Xiao, “An implantable RFID sensor tag toward continuous glucose monitoring,” *IEEE Journal of Biomedical and Health Informatics*, vol. 19, pp. 910–919, 2015.
- [22] X. Liu, J. L. Berger, A. Ogirala, and M. H. Mickle, “A touch probe method of operating an implantable RFID tag for orthopedic implant identification,” *IEEE Transactions on Biomedical Circuits and Systems*, vol. 7, pp. 236–242, 2013.
- [23] J. Mei, N. Riedel, U. Grittner et al., “Body temperature measurement in mice during acute illness: implantable temperature transponder versus surface infrared thermometry,” *Scientific Reports*, vol. 8, no. 1, p. 3526, 2018.
- [24] S. Yoshimoto, T. Araki, T. Uemura et al., “Wireless EEG patch sensor on forehead using on-demand stretchable electrode sheet and electrode-tissue impedance scanner,” in *Proceedings of the 38th Annual International Conference of the IEEE Engineering in Medicine and Biology Society (EMBC)*, pp. 6286–6289, Orlando, FL, USA, August 2016.
- [25] S. Krachunov and A. Casson, “3D printed dry EEG electrodes,” *Sensors*, vol. 16, no. 10, p. 1635, 2016.
- [26] J. Xu, R. F. Yazicioglu, C. Van Hoof, and K. Makinwa, *Low Power Active Electrode ICs for Wearable EEG Acquisition*, Springer, Berlin, Germany, 2018.
- [27] P. Grabiec, K. Domanski, D. Szmigiel, and D. Hodgins, “Electrode array design and fabrication for implantable

- systems,” *Implantable Sensor Systems for Medical Applications*, pp. 150–182, 2013.
- [28] Y. Wu, C. P. Chen, L. Mi et al., “Design of retinal-projection-based near-eye display with contact lens,” *Optics Express*, vol. 26, no. 9, pp. 11553–11567, 2018.
- [29] J. De Smet, A. Avci, P. Joshi, D. Schaubroeck, D. Cuypers, and H. De Smet, “Progress toward a liquid crystal contact lens display,” *Journal of the Society for Information Display*, vol. 21, no. 9, pp. 399–406, 2013.
- [30] E. Mattei, F. Censi, A. Delogu, A. Ferrara, and G. Calcagnini, “Setups for in vitro assessment of RFID interference on pacemakers,” *Physics in Medicine and Biology*, vol. 58, no. 15, pp. 5301–5316, 2013.



## Research Article

# Coevolution of the Asymmetric Morphology and the Behaviour of Simple Predator Agents in Predator-Prey Pursuit Problem

Milen Georgiev , Ivan Tanev, and Katsunori Shimohara

*Graduate School of Science and Engineering, Doshisha University, 1-3 Tatara-Miyakodani, Kyotanabe, Kyoto 610-0321, Japan*

Correspondence should be addressed to Milen Georgiev; [shogo@shogo.eu](mailto:shogo@shogo.eu)

Received 9 October 2018; Revised 2 March 2019; Accepted 16 April 2019; Published 6 May 2019

Guest Editor: Somyot Kiatwanidvilai

Copyright © 2019 Milen Georgiev et al. This is an open access article distributed under the Creative Commons Attribution License, which permits unrestricted use, distribution, and reproduction in any medium, provided the original work is properly cited.

Humanity has long strived to create microscopic machines for various purposes. Most prominent of them employ nanorobots for medical purposes and procedures, otherwise deemed hard or impossible to perform. However, the main advantage of this kind of machines is also their main drawback—their small size. The miniature scale, they work in, brings many problems, such as not having enough space for the computational power needed for their operation or the specifics of the laws of physics that govern their behaviour. In our study, we focus on the former challenge, by introducing a new standpoint to the well-studied predator-prey pursuit problem using an implementation of very simple predator agents. Intended to model the small-scale (micro and nano) robots, these agents are morphologically simple—they feature a single line-of-sight sensor. The behaviour of the predator agents is simple as well—the (few) perceived environmental variables are mapped directly into corresponding pairs of rotational velocities of the wheels' motors. We implemented genetic algorithm to evolve such a mapping that results in a successful capturing of the prey by the team of predator agents. However, as the preliminary results indicated, the predators that use a straightforward sensor could not resolve more than just few of the tested initial situations. Thus, to improve the generality of the evolved behaviour, we proposed an asymmetric sensory morphology of predators—an angular offset to the sensor relative to the longitudinal axis—and coevolved the amount of such an offset together with the behaviour of predators. The behaviours, coevolved with a sensor offset between  $12^\circ$  and  $38^\circ$ , resulted in both an efficient and consistent capture of the prey in all tested initial situations. Moreover, some of the behaviours, coevolved with sensor offset between  $18^\circ$  and  $24^\circ$ , demonstrated a good generality to the increased speed of the prey and a good robustness to perception noise. The obtained results could be seen as a step towards the engineering of asymmetric small-scale for delivery of medicine, locating and destroying cancer cells, microscopic imaging, etc.

## 1. Introduction

With the advancement of technology and invention of the optical and electric microscopes, the humanity started exploring the miniature world. With these new discoveries; however, new problems started to arise. To discover the solutions to them, humankind turned to creating micro- and nanomachines on their own [1]. As a species, striving to survive various lethal conditions, we are exposed to the most prominent field of use for these new nanomachines, medicine. There are many procedures that are hard to perform by a human medical doctor and for which the newly created microrobots are perfectly suited [2]. Such procedures, in which the traditional approaches could harm the

surrounding (healthy) body tissues, include brain surgery, video diagnostics in hard-to-reach places, and pinpoint drug delivery (much needed in chemotherapy). Some of the advantages that nanotechnology provides are continuous monitoring, rapid response to a sudden change in conditions, minimal trauma to the tissues, relatively short recovery time, and minimal posttreatment care [3].

In our research, we are employing a multiagent system (MAS) as the model of a team of such simple small-scale robots. The advantage of the developed MAS, compared to centralized systems with analogical functionalities, is that it offers an increased modularity, reduced complexity (offering an intuitive solution to the divide-and-conquer approach of developing and deploying complex software systems), and

flexibility to diverse software and hardware platforms. From the viewpoint of the end-users, the benefits of using MAS are the superior robustness, increased fault tolerance, scalability, and performance. The latter is especially true, as the MAS could solve (inherently parallel or distributed) problems much faster than centralized (or single agent) systems. Moreover, due to their complex, nonlinear nature, MAS could often solve problems that a single agent is unable to solve. The whole team of multiple agents is expected to exhibit a behaviour that can be regarded as an emergent (high-level) property of the much simpler (lower-level) properties of the agents, or as a whole that is “more than the sum of its entities” (Aristoteles, 384 a.C.-322 a.C.), and, therefore, could not be devised by applying the conventional top-down software engineering approaches.

Currently, there are various challenges that are slowing the progress of the real-world applicability of MAS modelling the societies of small-scale robots. One of these challenges stems from the very advantage of these robots—their small size. The physical constraints imply that these robots could not feature a complex morphology—both the sensors and moving mechanisms need to be very simple to be able to fit in the limited space of the bot’s body. The robots would be behaviourally simple too, in that their decision-making would involve no computing, but rather a direct mapping of the (few) perceived environmental states into corresponding commands to their actuators. Most likely, the communication (if any) between the individual agents would be impossible to be realized in a direct manner and would be fulfilled implicitly, through the corresponding changes in the environment. Such robots can be regarded as an ultimate case of Occam’s razor principle, applied both to their morphology and decision-making. Such simplicity further widens the gap between the available properties of the individual robots and the desired complex overall behaviour of the team of such robots as a whole. This is especially true in our case as we focus on creating bots that could traverse the human body autonomously, rather than being guided by an external force and continuously monitored [4, 5].

The factors in favour of the possible small-scale implementation of the robots considered in our work include (i) their *minimalistic implementation*, (ii) compatibility with the *fluid dynamics* at very low Reynolds numbers, and (iii) robustness of the behaviour of the robots to *Brownian collisions* (diffusion), as elaborated below.

The *minimalistic implementation* implies very simple sensors, control, and effectors of the robots. Indeed, the single line-of-sight *sensor* adopted in our work is seen as one of the examples of “extreme simplicity” in robot (agent) perceptions in the fields of multiagent systems and swarm robotics [6–11]. It could be implemented by a single (or just a few) receptor(s)—pixel (of a camera), nanoparticle, etc. The control is also very simple—a purely reactive, direct mapping of the (few) perceived environmental states into corresponding effectors’ commands. The effectors are modelled as wheels in our robots, arranged in a differential drive configuration, which is seen as the minimal configuration for robots in 2D environments that allow both linear

movement and rotational (steering) movement of the robots [6–11].

Two of the features of the wheels of the robots considered in our work are related to their compatibility with the *fluid dynamics* at very low Reynolds numbers, pertinent to the real world of small-scale robots: (i) the wheels control the movement of robots by the resulting vectors of linear velocities (rather than forces that would require the consideration of torque of motors, mass and rotational momentum of the robots, resulting acceleration, etc.) applied to each of the two sides of the robot and (ii) the changes in these velocities occur instantly (there is no coasting). We introduced these features—controlling the robot by linear velocities of wheels that change instantly—to bridge the reality gap between the model of our robots and the very low Reynolds number dynamics of the small-scale robots. Indeed, at very low Reynolds numbers, the movement of the robot is characterized by the dominance of the viscous forces over the inertial ones [12]. Consequently, the mass (and the inertia) is not a relevant factor in such a movement, and the changes of velocities of the small-scale robots would happen almost instantly. In an eventual 3D implementation, the wheels could be superseded by more general “thrusters” that model the actual propulsion source of the small-scale robots—e.g., bioinspired rotating helical flagellum and a rotary artificial molecular machine [11, 12].

The robustness to *Brownian collisions* could be achieved by just having a sufficiently large size of the robot [12]. From another perspective, as we shall elaborate later, we tested the robustness of the proposed MAS to perception noise. The effects of collision with particles subjected to Brownian motion is somehow different from just a perception noise; however, our experiment could be seen as a first step towards the verification of the system in highly dynamic, uncertain environments.

Gauci et al. [6] previously modelled similar simple robots as agents. The agents were able to self-organize in order to solve the simple robot aggregation problem. The same framework was also successfully applied for the more complex object-clustering problem [7] in which the agents need to interact with an additionally introduced immobile object. The very possibility of a team of such agents to conduct an elaborate social (surrounding) behaviour in an environment featuring dynamic objects was recently demonstrated by Ozdemir et al. [8] in solving the herding problem, where a team of simple agents (shepherds) needs to guide multiple dynamic agents (sheep) toward an a priori-defined goal.

In our study, we proposed the use of a similar team of simple agents for the solution of a different task—the well-studied, yet difficult to solve predator-prey pursuit problem (PPPP) [13–17]. In this PPPP, eight identical, simple agents (predators) are used to capture the single dynamic agent (prey).

Our objective is to investigate the feasibility of applying the genetic algorithms (GA) to evolve such direct mapping of the four perceived environmental states into respective velocities of the wheels of predator agents that result in a successful capture of the prey by the team of predator agents.

Moreover, we are interested in whether coevolving (i) the asymmetric sensory morphology—an angular offset of the sensors—of predator agents and (ii) their behaviour would result in more efficient and general capturing.

Our motive for using the proposed instance of PPPP is based on the increased complexity of the problem, compared to the previously studied tasks [6–9]. In comparison to the previously investigated domains, PPPP requires the agents to exhibit a more diverse behavioural set, including exploration of the environment and surrounding and capturing the prey. In contrast to [8], in our implementation of the PPPP framework, the emergence of such behaviours is made additionally complicated, by the introduced constraints to the sensory and moving abilities of the predator agents. Compared to the unlimited range, assumed in other works, our predators feature myopic, limited-range sensors, and their movement speed is equal to that of the prey, instead of being faster [6, 8]. Furthermore, the initial position of the predators is such that the prey is not being surrounded, which may ease the task of capturing it. This can be viewed as injecting the clustered team of small-scale robots at a certain point into the human body.

An additional motivation of our research is the recognition that while many real-world scenarios could be, indeed, reduced to the previously researched wall-following, dispersal [9], clustering [6], and shepherding problems [8], there would be few scenarios—requiring a direct physical contact with an active prey—that could be modelled by the proposed instance of PPPP [18–20]. These scenarios might include pinpoint drug delivery, surrounding and destroying (cancer) cells or bacteria, gathering around cells to facilitate their repair or imaging, etc.

The remainder of this article is organized as follows. The second section describes the entities in the PPPP. In the third section, we elaborate the GA, adopted for the evolution of predator behaviours. In the fourth section, we present the experimental results and introduce the proposed asymmetric sensory morphology of predators. In the same section, we show the results on the robustness and generality of the evolved predator agents. The fifth section discusses the advantages of asymmetric morphology and the emergent behavioural strategies of the predator agents. We draw a conclusion in the sixth section.

## 2. Entities

*2.1. Predator Agents.* Each of the eight (identical) predator agents models a simple cylindrical robot with a single line-of-sight sensor featuring a limited range of visibility and two wheels (controlled by two motors) in a differential drive configuration.

The single line-of-sight (beam) sensor provides two bits of information, where each bit encodes whether an entity—either a (nearest) predator agent or the prey, respectively—is detected (if any) in the line-of-sight within the limited range of visibility. The implementation of such sensor would consist of two photodetectors, sensitive to two different, nonoverlapping wavelengths of (ultraviolet, visible, or infrared) light reflected (or emitted) by predators

and prey, respectively. Each of these two photodetectors provides one bit of information. Equipped with such sensors, the predators could perceive only four discrete possible states— $\langle 00 \rangle$ ,  $\langle 01 \rangle$ ,  $\langle 10 \rangle$ , and  $\langle 11 \rangle$ , as shown in Figure 1—of the environment. The state  $\langle 11 \rangle$  is the most challenging one to perceive. It could be sensed, however, under the following assumptions: (i) the prey is taller than the predators and (ii) to not obscure the shorter predators, the cross-section of the prey is either much narrower than predators or (at least partially) transparent for the light to be perceived by the predators. Notice that the perceived environmental states do not provide the predators with any insight about the distance to the perceived entities, nor their total number.

In our previous work [21], we noticed that the classical morphology of the agents—in which sensor is aligned with the longitude axis of the agents—results in successful solutions of more than a few initial situations. Therefore, instead of the commonly considered straightforward orientation of the sensor of the predators, we proposed an angular (e.g., counterclockwise) offset relative to their longitudinal axis. We speculated that such an asymmetric sensory morphology would allow the predators to evolve a more efficient capturing behaviour by implementing an equiangular (proportional) pursuit of the prey, aiming at the (estimated) point of the contact with the moving prey, rather than the currently perceived position of the latter. The proposed asymmetric morphology does not compromise the intended simplicity of the agents. The main features of the agents, used during the evolution of the behaviour of prey agents, are summarized in Table 1.

The entirely reactive behaviour of the predator agents could be described as a direct mapping of each of the perceived environmental states into a corresponding rotational speed of the wheel motors. For simplicity, instead of mapping into rotational speeds (e.g., RPM) of the motors, we will assume a mapping into the linear velocities of the wheels, expressed as the percentage—within the range  $(-100\%, \dots, +100\%)$ —of their respective maximum linear velocities (10 units/s, as shown in Table 1). For example, a velocity of  $-20\%$  implies that the motor of the wheel is rotating at  $20\%$  of its maximum linear velocity, and the wheel propels the corresponding side of the robot in a backward (negative) direction with a linear speed of 2 units/s (i.e.,  $20\%$  of the maximum linear speed of the wheel). The purely reactive decision-making of the predator agents could be formally defined by the following octet:

$$A = \{V_{00L}, V_{00R}, V_{01L}, V_{01R}, V_{10L}, V_{10R}, V_{11L}, V_{11R}\}, \quad (1)$$

where  $V_{00L}$  and  $V_{00R}$  are the linear velocities (as a percentage, set within the range  $(-100\%, \dots, +100\%)$ , of the maximum linear velocity) of the left and right wheels of the agents for the perceived environmental state  $\langle 00 \rangle$ , while  $V_{01L}$ ,  $V_{01R}$ ,  $V_{10L}$ ,  $V_{10R}$ ,  $V_{11L}$ , and  $V_{11R}$  are analogical velocities for the perceived environmental states  $\langle 01 \rangle$ ,  $\langle 10 \rangle$ , and  $\langle 11 \rangle$ , respectively.

Our objective of coevolving (via GA) the behaviour and asymmetric sensory morphology of the agents could be

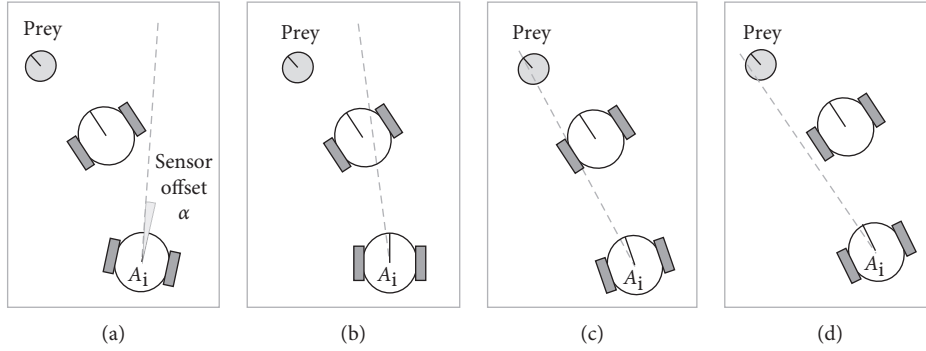


FIGURE 1: The four possible environmental states that are perceived by any given predator agent. (a) State  $\langle 00 \rangle$ . (b) State  $\langle 10 \rangle$ . (c) State  $\langle 11 \rangle$ . (d) State  $\langle 01 \rangle$ .

TABLE 1: Features of the entities used during the evolution of the behaviour of predator agents.

Feature	Predator	Prey
Number of agents	8	1
Radius (units)	8	8
Length of the axis of wheels (units)	16	16
Max linear velocity of wheels (units/s)	10	10
Max speed of agents (units/s)	10	10
Type of sensor	Single line-of-sight	Omnidirectional
Range of visibility of the sensor (units)	200	50
Orientation of sensor	Counterclockwise offset (2~40 degrees)	—

rephrased as coevolving (i) such values of the velocities, shown in the octet in equation (1), together with (ii) the angular offset of the sensor, resulting in an efficient capturing behaviour of the team of predator agents. We shall elaborate on such a coevolution in the next section.

**2.2. Prey.** The prey is equipped with an omnidirectional sensor, with limited visibility range. To balance the advantage that the omnidirectional sensor gives to the prey, compared to the single line-of-sight sensor of the predators, the viewing distance of the prey is only 50 units, compared to the 200 units of the predators. The maximum speed of the prey, however, is identical to that of the predators. These conditions would encourage the predator agents to evolve cooperative behaviours as they will be unable to capture the prey alone. Another viewpoint suggests that a successful solution to PPPP, defined in such a way, could demonstrate the virtue of the MAS as it could solve a problem that a single (predator) agent could not.

In contrast to the predator behaviours, we implemented a handcrafted behaviour for the prey. The prey attempts to escape from the closest predator (if any) by running at its maximum speed in the direction that is exactly opposite to the bearing of the predator. The prey remains still if it does not detect any predator. Table 1 shows the main features of the prey agent.

**2.3. The World.** We modelled the world as a two-dimensional infinite plane with a visualized part of  $1600 \times 1600$  units. We update the perceptions, decision-

making, and the resulting new state (e.g., location, orientation, and speed) of agents with a sampling interval of 0.1 s. The duration of trials is 120 s, modelled in 1200 time-steps. We approximate the new state of predators in the following two steps, as illustrated in Figure 2. First, from the current orientation, the yaw rate, and the duration of the sampling interval, we calculate the new yaw (orientation) angle (as an azimuth to the north) of the agents. The yaw rate is obtained from the difference between the linear velocities of the left and right wheels, and the length of the axis between the wheels. Then, we calculate the new position (i.e., the two-dimensional Cartesian coordinates) as a projection (in time, equal to the duration of the sampling interval) of the vector of the linear velocity of predators. The vector is aligned with the newly calculated orientation, and its magnitude is equal to the mean of the linear velocities of the two wheels.

### 3. Evolutionary Setup

We decide to apply a heuristic, evolutionary approach to the “tuning” of the velocities of both wheels for each of the perceived four environmental situations because we are a priori unaware of the values of these velocities that would yield a successful behaviour of the team of predator agents. As we briefly mentioned in Section 1, MAS, as a complex system, features a significant semantic gap between the simple, hierarchically lower-level properties of the agents and the more elaborate, higher-level behaviour of the whole system. Consequently, we would be unable to formally infer the values of the octet of velocities of the wheels of agents

```

// Global definitions:
type
  TEntitiy_in_MAS = record
    Yaw : float; // radians
    X   : float; // units
    Y   : float; // units
  end;
const
  Num_of_Predators      = 8;
  Pred_Max_Speed        = 10; // units/s
  Sampling_Interval     = 0.1; // seconds
  Pred_Radius           = 8; // units
var
  Predator: array [0.. Num_of_Predators-1] of TEntitiy_in_MAS;
...
// The routine Move_Predator estimates the new state of predators
Procedure Move_Predator (ID: integer; V_L,V_R: float);
// ID: the ID of the predator being currently updated, within the range [0..7]
// V_L and V_R: linear velocities of the left and right wheels, respectively.
// Calculated from the evolved genotype (as percentages of the max velocities), the values of max velocities
// (10 units/s), and currently perceived (one of the four: <00>,<01>,<10> or <11>) environmental situations.
// For the evolved sample genotype <10,15,20,25,30,35,40,45> and current situation <01> these values
// are V_L=2.0 units/s, and V_R=2.5 units/s, respectively
begin
// Step #1: Calculating the new yaw angle of the predators #ID as azimuth (to the north) in radians:
  Predator[ID].Yaw := Predator[ID].Yaw + (V_L - V_R) / (Pred_Radius × 2) × Sampling_Interva

// Step #2: Calculating the new position (X,Y) of the predator #ID:
  Predator[ID].X := Predator[ID].X + ((V_L + V_R) / 2) × sin(Predator[ID].Yaw) × Sampling_Interval;
  Predator[ID].Y := Predator[ID].Y + ((V_L + V_R) / 2) × cos(Predator[ID].Yaw) × Sampling_Interval;
end;

```

FIGURE 2: The pseudocode of estimating the new state of the moving predators.

from the desired behaviour of the team of such agents. Similarly, we are unaware of the value of the angular offset of the sensor, resulting in an efficient capturing behaviour of the agents. Moreover, the values of velocities of both wheels and the value of the angular offset of the sensor would, most likely, be dependent on each other.

Alternatively, in principle, we could have adopted another, deterministic, approach, such as, for example, a complete enumeration of the possible combinations of the eight velocities of wheels and the sensor offset. If each of these 8 velocities is discretized into, say, 40 possible integer values ranging from  $-100\%$  to  $+100\%$  and the sensor offset just into 20 values, then the size of the resulting search space would be equal to  $40^8$  or about  $1.3 \times 10^{14}$ . This would render the eventual “brute force” approach, based on complete enumeration of possible combinations of values of velocities computationally intractable.

As an alternative to the brute force search, we could apply reinforced learning (RL) in order to define the good mapping of the four perceived environmental states into the four pairs of velocities of wheels. However, MAS are complex, nonlinear systems, and there is a significant gap between the properties of the entities and the (emergent) properties of the system. RL would obtain a “reward” from

the system (i.e., the efficiency of the team of predators) and will try to modify the properties (the four pairs of velocities of wheels) of the entities. Due to the complexity and non-linearity of MAS, this is not a straightforward task. This is also related to the intra-agent credit-(or blame-) assignment problem, as we could not tell which part of the agents is responsible (and therefore—should be modified) for the bad overall behaviour of the system.

Evolutionary computing solves these challenges in an elegant way, by obtaining the fitness value from the system, as a whole (i.e., the efficiency of predators in capturing the prey) and then modifying the properties of entities (pairs of velocities of wheels of predators) via genetic operations, crossover and mutations.

Yet another challenge in RL is the delayed reward problem—the success (if any) of the system (team of predators) would occur several hundred time-steps into the trial, but might be related to the earlier behaviour phases of the team of predators—such as the dispersing (exploration of the environment) at the very beginning of the trial. Regarding the delayed reward problem, the evolution, as a holistic approach, does not care about how to achieve the success, but rather about the overall (final) outcome of the trial.

In our work, we apply GA, a nature-inspired heuristic approach that gradually evolves the values of a set of parameters in a way similar to the evolution of species in nature. GA has proved to be efficient in finding optimal solution(s) to combinatorial optimization problems featuring large search spaces [22–24]. Thus, consonant with the concept of evolutionary robotics [25], we adopted GA to evolve the values of the eight velocities of the wheels and the offset of the sensor that result in an efficient behaviour, presumably involving exploring the environment and surrounding and capturing the prey, of the team of predators. The main algorithmic steps of the adopted GA are shown in Figure 3, and its main attributes, genetic representation, genetic operations, and fitness function, are elaborated below.

**3.1. Genetic Representation.** We genetically represent both (i) the decision-making (behaviour) of the predator agents and (ii) their sensory morphology in a single “chromosome”. The latter consists of an array of eight integer values of the evolved velocities of wheels of the agents and an additional allele encoding the angular offset of their sensor. The values for the velocities are constrained within the range (−100% . . . +100%) and are divided into 40 possible discrete values, with an interval of 5% between them. The angular offset is defined in range between 2° and 40°, counter-clockwise, divided into 20 possible discrete values, with an interval of 2° between them. The decided number of discrete values (and the interval between these values, respectively) provides a good trade-off between the precision of “tuning” (i.e., expressiveness of the genetic representation) and the size of the search space of GA. The population size is 400 chromosomes. The breeding strategy is homogeneous in that the performance of a single chromosome, cloned to all predators is evaluated.

**3.2. Genetic Operations.** Binary tournament is used as a selection strategy in the evolutionary framework. It is computationally efficient and has proven to provide a good trade-off between the diversity of population and the rate of convergence of the fitness. In addition to the tournament selection, we also adopted elitism in that the four best-performing chromosomes survive unconditionally and are inserted into the mating pool of the next generation. In addition, we implemented, with equal probability, both one- and two-point crossover. The two-point crossover results in an exchange of the values of both velocities (of the left and right wheels, respectively) associated with a given environmental state. This reflects our assumption that the velocities of both wheels determine the moving behaviour of the agents (for a given environmental state), and therefore, they should be treated as a whole—as an evolutionary building block. Two-point crossovers would have no destructive effect on such building blocks. The one-point crossover is applied to develop such building blocks (exploration of the search space), while the two-point crossover is intended to preserve them (exploitation).

Step 1:	Creating the initial population of random chromosomes;
Step 2:	Evaluating the population;
Step 3:	WHILE not (Termination Criteria) DO Steps 4–7:
Step 4:	Selecting the mating pool of the next generation;
Step 5:	Crossing over random pairs of chromosomes of the mating pool;
Step 6:	Mutating the newly created offspring;
Step 7:	Evaluating the population;

FIGURE 3: The main algorithmic steps of the GA.

**3.3. Fitness Evaluation.** Our aim is to coevolve the behaviours and sensory morphology of the team of predators that are general to multiple initial situations, rather than a behaviour that is specialized to a particular one situation. To facilitate such an evolution, we evaluated each of the evolving chromosomes in 10 different initial situations. In each of these situations, the prey is located in the centre of the world. The predators are scattered in a small cloud situated south of the prey. A snapshot of a sample initial situation is shown in Figure 4. The distance of the cluster, of agents, to the prey is calculated as follows: ID of the current situation  $\times 2 +$  (random of 50 units). This helps reduce the impact of the first few evolutionary runs, when the predators are learning how to move around the environment to find the prey.

The overall fitness is the sum of the fitness values, scored in each of the 10 initial situations. For a successful situation (i.e., the predators manage to capture the prey during the 120 s trial), the fitness is equal to the time needed to capture the prey. If the initial situation is unsuccessful, the fitness is calculated as a sum of (i) the closest distance, registered during the entire trial, between the prey and any predator and (ii) a penalty of 10,000. The former component is intended to provide the evolution with a cue about the comparative quality of the different unsuccessful behaviours. We verified empirically that this heuristic quantifies the “near-misses” well and correlates with the chances of the predators—pending small evolutionary tweaks in their genome—to successfully capture the prey in the future. The second component is introduced with the intention to heavily penalize the lack of success of predators in any given initial situation.

Our PPPP is an instance of a minimization problem, as lower fitness values correspond to better performing team of predator agents. Since we are aiming to discover the best possible solution to the problem, no target fitness value is incorporated in the termination criterion of the evolution. Instead, this criterion includes the following two conditions: the number of the evolved generations is equal to 200 or the best fitness remains unchanged (stagnated) for 32 consecutive generations. Table 2 shows the main parameters of the adopted GA.

## 4. Experimental Results

**4.1. Evolving the Team of Straightforward Predator Agents.** The experimental results of 32 independent runs of the GA evolving only the behaviour of the predator agents are illustrated in Figure 5. In these runs of the GA, the sensory

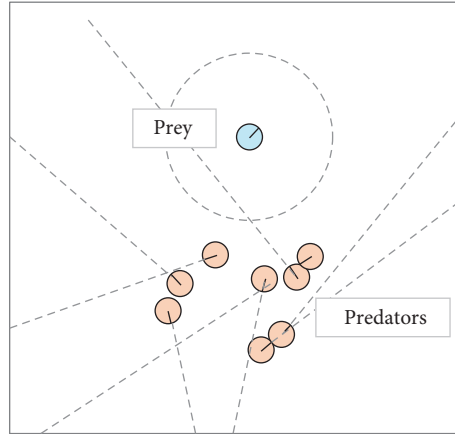


FIGURE 4: A snapshot of a sample initial situation.

TABLE 2: The main parameters of the GA.

Parameter	Value
Genotype	Eight integer values of the velocities of wheels ( $V_{00L}$ , $V_{00R}$ , $V_{01L}$ , $V_{01R}$ , $V_{10L}$ , $V_{10R}$ , $V_{11L}$ , and $V_{11R}$ ) and an integer value of the angular offset ( $\alpha$ ) of the sensor
Population size	400 chromosomes
Selection	Binary tournament
Selection ratio	10%
Elite	Best 4 chromosomes
Crossover	Both single- and two-point
Mutation	Single-point (with even distribution)
Mutation ratio	5%
Fitness cases	10 initial situations
Duration of the fitness trial	120 s per initial situation
Fitness value	Sum of fitness values of each situation:
	(a) Successful situation: time needed to capture the prey (b) Unsuccessful situation: 10,000 + the shortest distance between the prey and any predator during the trial
Termination criterion	No. of generations = 200 or stagnation of fitness for 32 consecutive generations

morphology of predators was fixed, and the sensor offset was set to 0. As Figure 5(a) illustrates, the mean value of the fitness slowly converges to approximately 60,000, indicating that, on average, only 4 (of 10) initial situations could be successfully resolved (Figure 5(b)). The best result, achieved by the evolved team of predators, is only 6 successful situations. These results suggest that the instance of PPPP featuring predators with straightforward sensors is, in general, intractable.

*4.2. Coevolving the Asymmetric Morphology and the Behaviour of Predator Agents.* As Figures 6–8 illustrate, just by adding the offset, the results in number of successful initial situations and overall fitness significantly improve compared to the evolution of the team straightforward predator agents featuring no angular offset of sensors. On average, the predators were able to resolve all 10 initial situations by 10th generation of the GA. From all 32 independent runs of GA,

there is one distinguished solution (from now on we will refer to it as the fastest evolved solution SFE) which successfully solves 8 (of 10) in the first generation. The chromosome of this solution encodes for offset of the sensor of  $20^\circ$ . This confirms the findings in our previous research [21, 26] that a team of predators with  $20^\circ$  sensor offset yields favourable results during evolution. As we will discuss later, this is also true in case of additional, unforeseen, situations and presence of perception noise. However, from all 32 solutions, this is not the one that has achieved the best overall fitness value. The best behaviour of agents (manifested by the achieved lowest of fitness value) was obtained by the solution SBF featuring a sensory offset of  $16^\circ$ . Compared to the fastest evolving solution SFE, the solution SBF evolved a bit slower and solved all 10 situations by 6th generation, achieving the terminal fitness of 369 (compared to 417 of solution SFE).

Figure 9 illustrates the angular offset of the best solutions obtained from each of the 32 independent runs of the GA. As

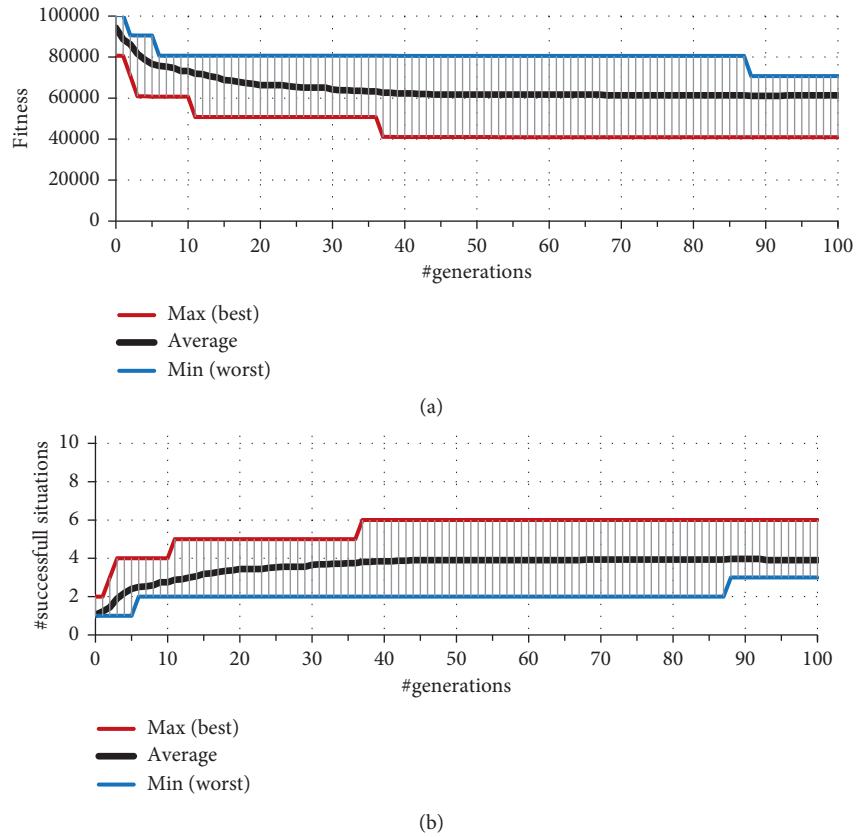


FIGURE 5: Convergence of the values of best fitness (a) and the number of successful situations (b) of 32 independent runs of GA evolving the behaviour of straightforward (without an offset of the sensor) predator agents.

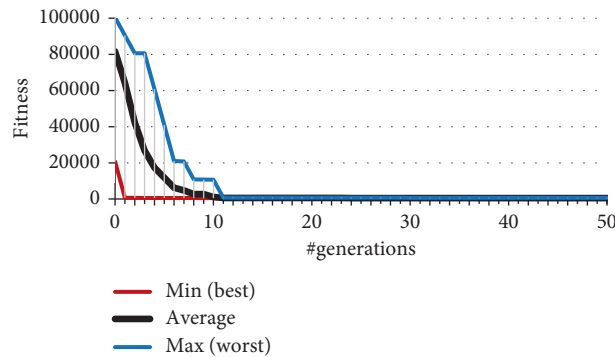


FIGURE 6: Convergence of the best fitness of 32 independent runs of GA.

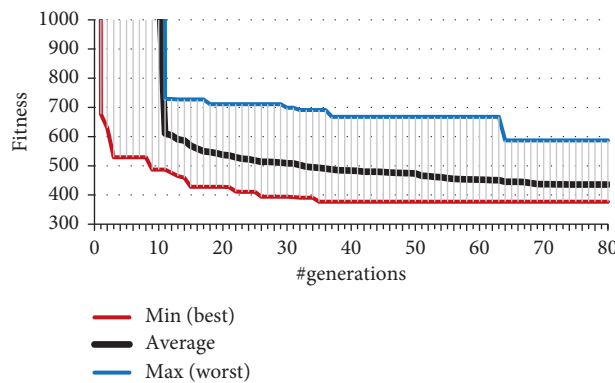


FIGURE 7: A more detailed illustration of the convergence of the best fitness of 32 independent runs of GA.



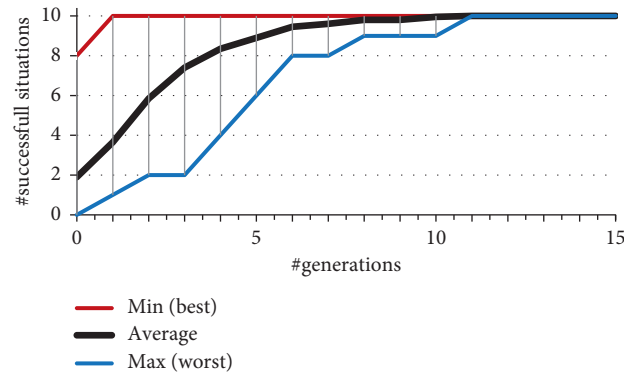


FIGURE 8: Convergence of the number of successful situations of 32 independent runs of GA.

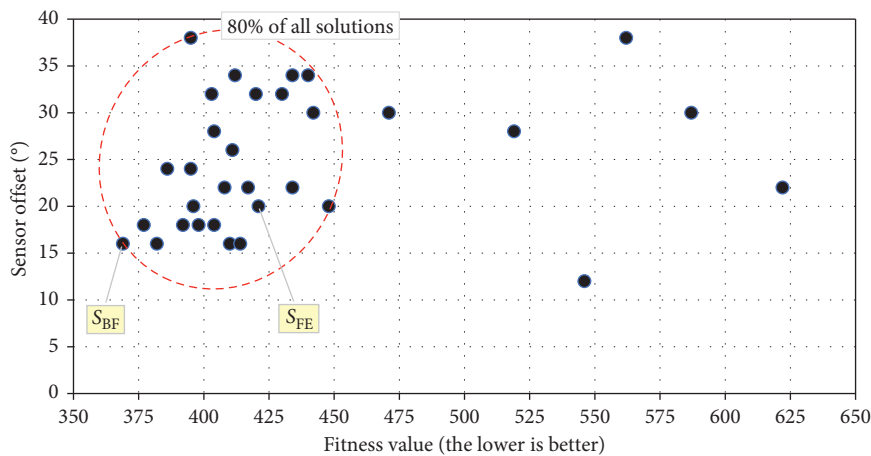


FIGURE 9: Sensor offset and the fitness value of all 32 solutions obtained from 32 independent runs of the GA. The fastest evolved and the best overall solutions are denoted as solutions SFE and SBF, respectively.

seen in Figure 9, the fitness of 80% (i.e., 26 of 32) of solutions is in the range between 369 and 448, i.e., the team of agents could capture the prey (on average over all 10 situations) between 36.9 s and 44.8 s into the allocated 120 s of the trial. The fitness of the worst solution is 622, meaning that the team of predator agents captures the prey, on average, at 62.2 s, i.e., around the middle of the 120 s trial. Moreover, as Figure 9 illustrates, for a particular value of the sensor offset, there are multiple solutions with different fitness values, meaning that there are variations in the behaviour of the morphologically identical predators and that the sensory asymmetry is only a precondition for an efficient capturing behaviour of the predators. Analogically, very similar fitness values could be achieved by predators featuring different sensor offset, suggesting that the combination of both (i) the morphology and (ii) the behaviour, rather than a particular instance of each of them, is important for the success of the behaviour of predator agents.

The breakdown of the number of the successful situations and the sensor offset of all 32 solutions are illustrated in Figure 10. As depicted in Figure 10(a), the sensor offset of 90% (i.e., 29 of 32) of solutions is within the range ( $15^\circ, \dots, 35^\circ$ ). There is no evolved solution that features a sensor offset lower than  $10^\circ$ , which confirms experimentally our initial hypothesis about the beneficial effect of the asymmetric

morphology of predators on the efficiency of their behaviour. The statistical characteristics of all 32 solutions are shown in Table 3.

**4.3. Generality of the Evolved Solutions.** To assess the generality of the evolved behaviour of the predator agents, we will examine how their performance (i.e., the number of successfully resolved initial situations) degrades with the increase of the speed of the escaping prey. We tested all 32 solutions, obtained via the GA (for the speed of the prey equal to 10 units/s), for speeds of the prey, unforeseen during the evolution, of 12, 14, 16, 18, and 20 units/s, respectively. The number of initial situations successfully solved by each of the 32 solutions for each of the considered speed of the prey is shown in Figure 11. The mean (over the whole range of speeds of the prey) of the successfully solved situations by each of these solutions, and its breakdown are depicted in Figure 12. As these figures illustrate, one of these solutions, denoted as  $S_{MG}$ , is most general in that it features no degradation in the number of successful situations with the increase of the speed of the prey. Moreover, its fitness value remains under 500 (i.e., the agents capture the prey earlier than 50 s into the 120 s trial) for all considered speeds of the prey. As shown in Table 4, the sensor offset of  $S_{MG}$  is  $24^\circ$ .

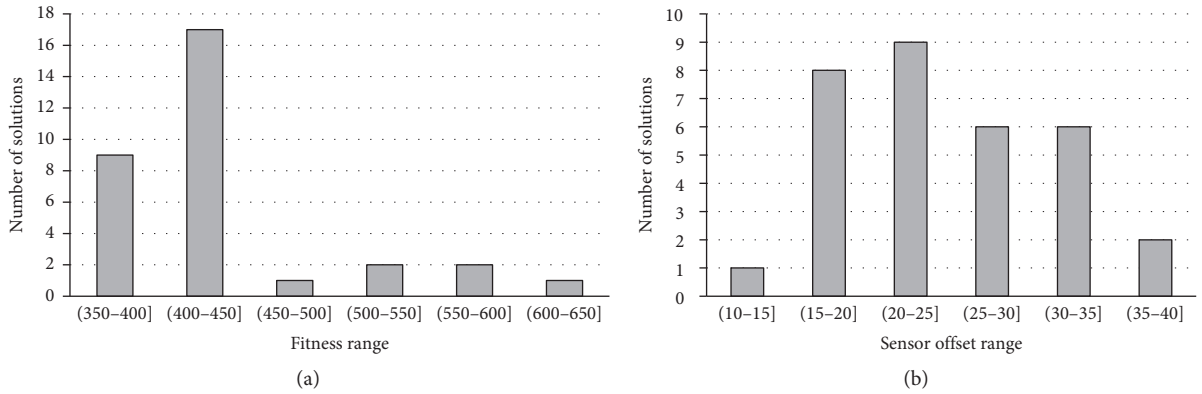


FIGURE 10: The breakdown of the number of the successful situations (a) and the sensor offset (b) of all 32 solutions obtained form 32 independent runs of the GA.

TABLE 3: Statistical characteristics of the 32 solutions obtained form 32 independent runs of the GA.

Parameter	Value
Mean of the best fitness values	436
Standard deviation of the best fitness value	63
Mean of the sensor offset (°)	24.7
Standard deviation of the sensor offset (°)	7.2

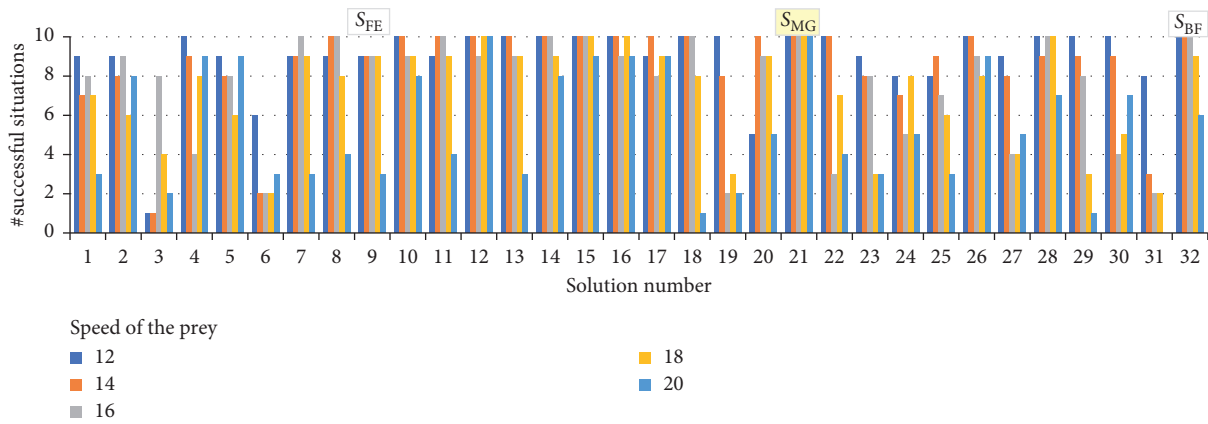


FIGURE 11: The number of successfully solved situations by the evolved 32 solutions for the speed of prey being increased from 10 to 12, 14, 16, 18, and 20 units/s, respectively.

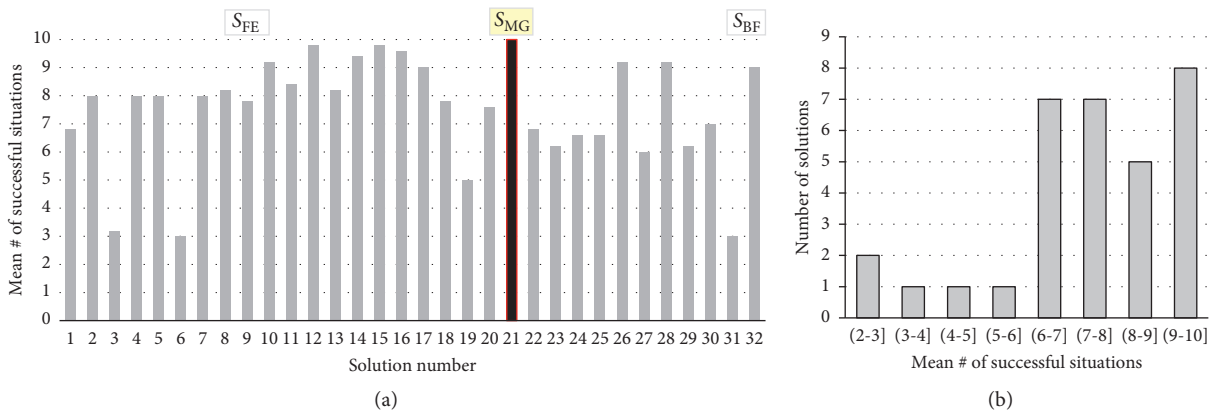


FIGURE 12: Generality of the evolved 32 solutions to the changes in the speed of prey from 10 to 12, 14, 16, 18, and 20 units/s: the mean number of successfully solved situations (a) and its breakdown (b).

TABLE 4: Genotype of evolved solutions: the fastest evolved (SFE), with the best fitness (SBF), most general (SMG), most robust to FP (SMRFP), and FN (SMRFN) noise.

Solution	Fitness	$V_{00L}$ (%)	$V_{00R}$ (%)	$V_{01L}$ (%)	$V_{01R}$ (%)	$V_{10L}$ (%)	$V_{10R}$ (%)	$V_{11L}$ (%)	$V_{11R}$ (%)	Sensor offset $\alpha$ ( $^\circ$ )
$S_{FE}$ (#9)	417	30	95	100	90	-80	-75	50	-95	22
$S_{BF}$ (#32)	369	-95	80	90	85	-90	-90	100	90	16
$S_{MG}$ (#21)	382	-95	80	95	90	-90	-90	60	-10	24
$S_{MRFP}$ (#11)	404	-70	70	90	85	-100	-100	65	70	18
$S_{MRFN}$ (#14)	421	30	100	100	95	-75	-70	100	100	20

**4.4. Robustness to Perception Noise.** We evaluated the robustness of the 32 evolved solutions, evolved in a noiseless environment, to a random perception noise. We introduced two types of noise—a false positive (FP) and a false negative, respectively. The former results in either of the two bits of perception information to be occasionally (with a given probability) read as “1” regardless of whether an entity is detected in the line-of-sight of the predators or not. False negative noise (FN) results in readings of “0” even if an entity is seen. We focused on these types of noise as we assume that the perception subsystem of predators, yet being rather simple, would require an appropriate thresholding of the sensory signal. A combination of unfavourable factors, such as incorrectly established threshold and variable noise levels in the environment or in sensors, would result in the considered two types of perception noise. Figures 13 and 14 show the degradation of the number of successfully solved situations by all 32 solutions for different amount of FP and FN perception noise, respectively.

As Figures 13 and 14 illustrate, neither the fastest evolved solution  $S_{FE}$  nor the solution with the best fitness  $S_{BF}$ , which we previously discussed, features a good robustness to perception noise. On average, they solve 6.25 initial situations each, with the introduction of either FP or FN noise. Both solutions yield similar results with the difference between them being that  $S_{BF}$  is more robust to FP noise while  $S_{FE}$  is better in case of FN noise. Instead, the solutions  $S_{MRFP}$  and  $S_{MRFN}$  (featuring a genotype as shown in Table 4) emerge as most robust to FP noise and FN noise, respectively. Solution  $S_{MRFP}$  manages to solve the tests with FP noise perfectly, while maintaining satisfactory performance in the tests with FN noise, being able to solve on average 8.25 initial situations, depending on the level of FN noise. On the contrary, the agents controlled by  $S_{MRFN}$  solve the situations with FP noise perfectly, while being able to solve an average of 9.5 initial situations in the situations with FN noise, resulting in the best overall performance. The sensor offset of  $S_{MRFP}$  and  $S_{MRFN}$  is  $18^\circ$  and  $20^\circ$ , respectively (Table 4).

## 5. Discussion

**5.1. Advantage of Asymmetric Morphology.** We have shown that introducing an angular offset to the viewing sensor facilitates a more effective behaviour of the team of agents and increases the efficiency of evolution of such behaviour. The experimental results suggest that the behaviour, evolved with a sensor offset of  $20^\circ$  (in solution  $S_{MRFN}$ ), is most robust to noise and is close enough in terms of fitness to the best-performing team of agents in noiseless environments. The

fitness of  $S_{MRFN}$  is 421 compared to 369 of  $S_{BF}$ . While  $S_{MG}$  shows best results in the generality test, with perfect score in all initial situations, it falls short in the noise robustness test. This leads us to believe that  $S_{MRFN}$  is an example of a good combination of coevolved behaviour and asymmetric morphology of the predator agents. On average,  $S_{MRFN}$  manages to solve 9.57 and 9.65 situation in the generality and robustness tests cases. The angular offset of  $20^\circ$  of  $S_{MRFN}$  provides a good trade-off between the tangential and radial (i.e., towards the prey) components of the speed vector of the chasing predators.

The beneficial effect of the sensor offset is that it helps the chasing predator to implicitly determine the position of the prey if the latter disappears. Having a counterclockwise displacement means that most of the time the disappeared prey, due to the parallax induced by the movement of the predator, would be to the left, and consequently, a slight turn to the left would allow relocating it again. Therefore, one of the virtues of the sensor offset is in the *more deterministic direction* of the disappearance of the prey, almost certainly to the left, which in turn facilitates a faster rediscovery and consequently, a more reliable tracking of the latter by the predator. Moreover, as shown in Figure 15, the chase by the predator featuring an asymmetric morphology would result in a characteristic *circular trajectory* of both the predator and the prey. With the rather challenging but realistic assumption that initially the prey is not being surrounded by the predators (as illustrated in Figure 4), such circular trajectories would facilitate the surrounding as the prey would be shepherded (driven) by a single predator towards the pack of the remaining predators.

**5.2. Emergent Behavioural Strategies.** Following our previous work on coevolving behaviour and morphology [27], in this section, we review the behavioural strategies, emerging from the team of agents controlled by the evolved solution that is most robust to noise, the solution has the greatest success rate, the solution  $S_{MRFN}$ . The values of the evolved velocities of motors and the sensor offset are shown in Table 4. The team of predator agents manifests the following three types of behaviours, executed in three consecutive phases of the trial: (i) *exploring* the environment by distancing themselves from each other (controlled by velocities  $V_{10}$ ) or circling around until they find a peer or the prey ( $V_{00}$ ), (ii) *shepherding* (driving) the prey (by some of the predators) in an circular trajectory ( $V_{01}$ ), and (iii) *capturing* the prey ( $V_{11}$ ). Figure 16 illustrates the different phases the agents go through in the process of catching the prey. A

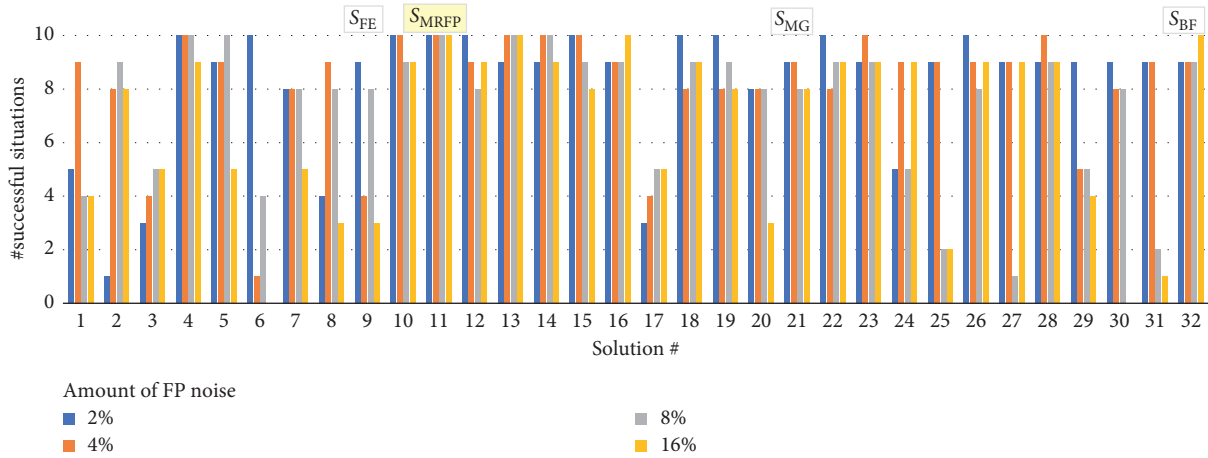


FIGURE 13: Robustness to FP noise of each of the 32 evolved solutions.

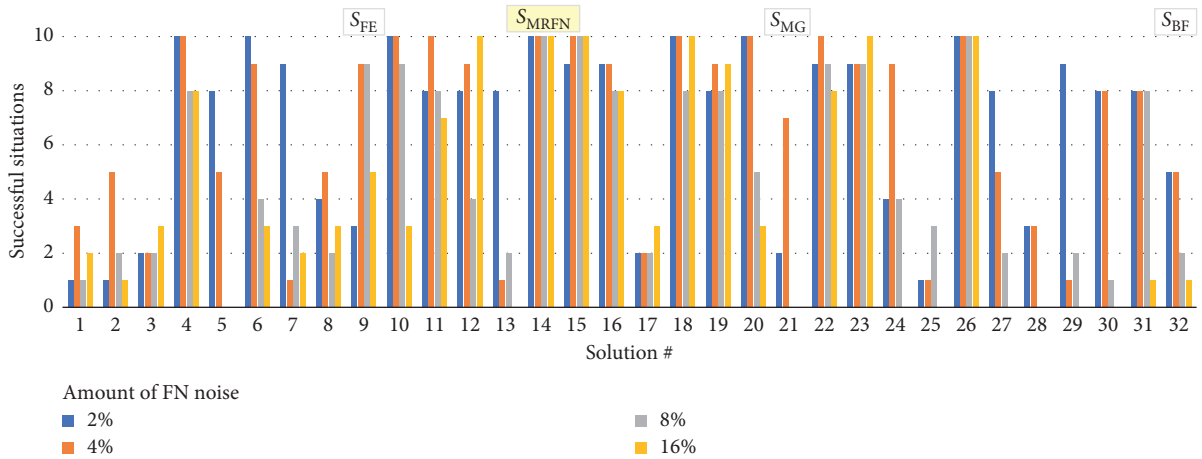


FIGURE 14: Robustness to FN noise of each of the 32 evolved solutions.

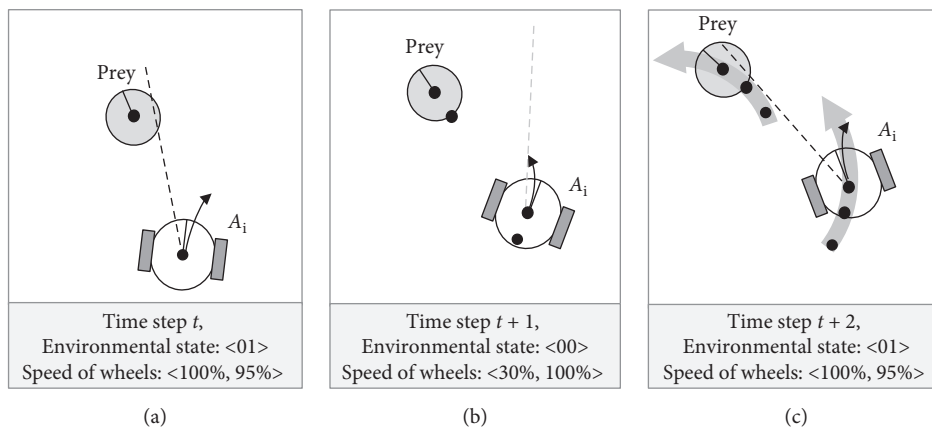


FIGURE 15: Chasing the prey by a sample predator agent  $A_i$ .

video of how the team of predators deals with all 10 situations can be found at <http://isd-si.doshisha.ac.jp/m.georgiev/2018-12-08-SA20deg.mp4>.

As shown in Figure 16(a), in the beginning, all agents have no vision of either the prey or any of the peers. Following the mapping of  $V_{00L} = 30\%$  and  $V_{00R} = 100\%$ , they

start turning around in a circular motion—scanning the environment in an attempt to find another entity. Detecting a peer activates the set of velocities  $V_{10L} = -75\%$  and  $V_{10R} = -70\%$ , which forces the predators to rapidly move away from the perceived agent, which facilitates a better dispersion and a coverage of a wider area. This enhances the

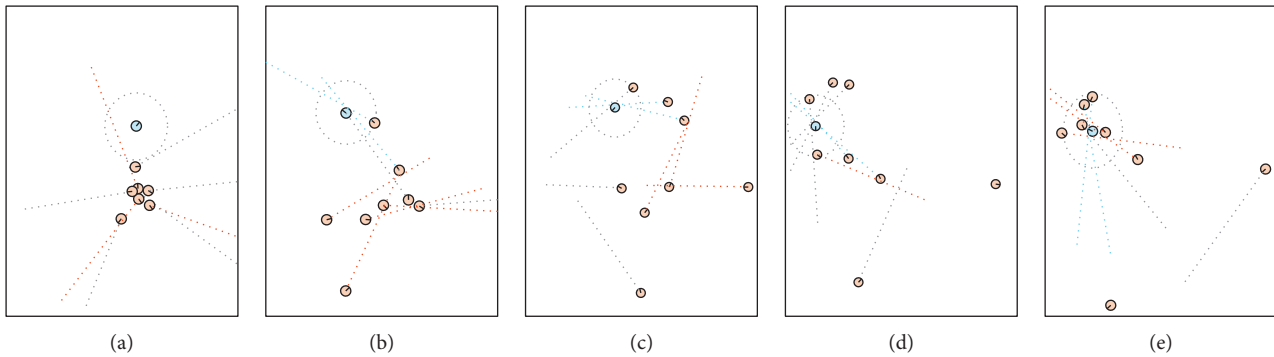


FIGURE 16: Emergent behavioural phases exhibited by the team of predator agents: exploring (a), herding (b–d), and capturing (e).

ability of the predators to *explore* the environment and to discover the prey. The second stage begins when any of the predators discovers the prey. The mapping  $V_{01L} = 100\%$  and  $V_{01R} = 95\%$  results in moving forward at highest speed and slightly turning to the right, which helps keeping the prey always in the same relative position to the agent, to the left side, as shown in Figures 15 and 16(b)–16(d). Once the prey becomes invisible, as shown in Figure 16(b), the predator exhibits an *embodied cognition* that the disappearance is a result, in part, of its own forward motion; therefore, the new location of the prey is, due to the counterclockwise offset of the sensor, most likely on the left of its own orientation. The evolved  $V_{00L} = 30\%$  and  $V_{00R} = 100\%$  are activated (Figure 15(c)) resulting in a circular motion to the left, until the agent rediscovers the disappeared prey. Moreover, as Figures 16(b)–16(d) show, a single predator, due to its sensor offset, *shepherds* (drives) the prey in a circular, counterclockwise trajectory into the (already dispersed) other predators. The final behavioural phase begins with the surrounding of the prey from all sides of the world by both thus far and newly encountered chasing predators, as illustrated in Figure 16(e). When approaching from opposite sides, the predators are able to see both the prey and a peer, which activates the mapping  $V_{11L} = 100\%$  and  $V_{11R} = 100\%$ . Since they have a slight angular offset, it is possible for only two predators to catch the prey, as illustrated in Figure 16(e). One of the predators chases the prey from behind and guides it to its front left side, while the other intercepts it from the exactly opposite direction.

At the same time, we can see in Figures 16(d) and 16(e) that two of the agents keep distancing themselves from the group. The agents seem to exhibit an emergent knowledge [28] that not all eight agents are needed to capture the prey. For the group of agents to be successful, the most important mission is to capture the prey, rather than which particular agent does it. As the performance of the predators is calculated based on the success of the group instead of that of the particular individual agent, such behaviour helps the team (as a whole) by expanding the search field and finding the prey faster, especially when it is further away from the predators. If, instead, the agents were trying to find the prey and capture it by themselves via “greedy chase,” they would inevitably fail because (i) the prey is fast enough to run away from a single predator and (ii) the predators would have

been unable to engage in any organized behaviour that allows surrounding and ultimately, capturing the prey.

The most significant difference between the evolved behaviour of straightforward predator agents and that of the agents with asymmetric morphology is in the second behavioural phase, *shepherding*. This phase could not be observed in the behaviour of the straightforward agents. At the same time, as we elaborated above, it plays an important role in the successful capturing of the prey.

**5.3. Heterogeneous vs. Homogeneous Systems.** During our research, we considered a different configuration for the multiagent system featuring several types of predator agents where each of them has a specific role in capturing the prey. Our work on performance comparison between heterogeneous and homogeneous MAS [29] delves deeper into the problems that heterogeneity brings: our main concern was that the heterogeneous system would suffer from inferior efficiency of evolution due to the inflated search space. Moreover, the robustness of the evolved behaviour of the team of specialized predator agents would be questionable too. The reason for this is that if, for example, the team employs a dedicated “driver” agent, in real-world situations, it could be challenging to make sure that the agents would be deployed in the vicinity of the prey (i.e., a cancer cell) in such a way that the “driver” is in the most favourable position relative to the prey and other predators. Instead, we opted for an implicit behavioural heterogeneity (with genotypic homogeneity)—the agents that are the closest to the prey assume the role of the “driver”, and any of the eight predator agents may turn into this role, if needed. The heterogeneity is implicit because it arises from the interaction between the homogeneous genotype (all agents have identical four pairs of velocities of wheels) and the environment. The dynamically faced environment is what “specialises” the different predator agents in the team.

## 6. Conclusions

Nanorobots are newly emerging technology, made possible by the rapid technological advancements in the last century. Creating synthetic machines on a miniature level, however, shows that there are significant problems to overcome, due

to the differences in physics laws and the limited resources available due to the small size of the robots. Furthermore, as medicine is the most prominent field of use for these new machines, they need to be reliable and precise in their work, which requires making no compromises in the quality of their operation. In attempt to solve these restrictions, we employed a variation of the predator-prey pursuit problem (PPPP), implementing very simple predator agents, equipped with a single line-of-sight sensor, and a simple control of the velocities of their two wheels. The predator agents utilize a direct mapping of the few perceived environmental states into corresponding velocities for their pair of their wheels. We applied genetic algorithms to evolve such a mapping that results in a successful capturing of the prey by the team of predator agents. However, as the preliminary results indicated, the predators featuring a straightforward sensor could not resolve more than just few of the tested initial situations. To improve the generality of the evolved behaviour, we proposed an asymmetric sensory morphology of predators, an angular offset to the sensor relative to their longitudinal axis, and coevolved both (i) the amount of this offset and (ii) the behaviour of predators. According to the experimental results, the behaviour coevolved with a sensor offset between  $12^\circ$  and  $38^\circ$  resulted in both an efficient and consistent capture of the prey in all tested initial situations. Moreover, few of the evolved behaviours for a sensor offset in the range  $18^\circ$ – $24^\circ$  demonstrated a good generality to the variations in the speed of the prey and a good robustness to perception noise.

We believe that the obtained results could be viewed as a step towards the engineering of nanorobots with asymmetric morphology for various medical applications including pinpoint delivery of medicine, locating and destroying cancer cells, microscopic imaging, etc. In our future work, we are planning to develop a three dimensional model which will resemble a more realistic environment such as the human body.

## Data Availability

The data used to support the findings of this study are included within the article.

## Conflicts of Interest

The authors declare that there are no conflicts of interest regarding the publication of this paper.

## Acknowledgments

This research extends the previous work on “Coevolving Behaviour and Morphology of Simple Agents that Model Small-scale Robots” [27]. The authors have included more detailed discussion and evidence, about the benefits of asymmetric morphology in simple multiagent systems and the improvements it brings to generality, robustness and evolved behaviour. This work was assisted by Doshisha University, which provided the facilities and equipment needed for testing and analyses. The corresponding author

Milen Georgiev was partly supported by the Japanese Ministry of Education, Culture, Sports, Science and Technology (MEXT).

## References

- [1] S. M. Martel, P. G. Madden, L. Sosnowski, I. W. Hunter, and S. Lafontaine, “Nanowalker: a fully autonomous highly integrated miniature robot for nanoscale measurements,” *Microsystems Metrology and Inspection*, vol. 3825, no. 1, pp. 111–122, 1999.
- [2] L. Mertz, “Tiny conveyance: micro-and nanorobots prepare to advance medicine,” *IEEE Pulse*, vol. 9, no. 1, pp. 19–23, 2018.
- [3] A. S. Bhat, “Nanobots: the future of medicine,” *International Journal of Management and Engineering Sciences*, vol. 5, no. 1, pp. 44–49, 2014.
- [4] D. H. Kim, U. K. Cheang, L. Kóhidai, D. Byun, and M. J. Kim, “Artificial magnetotactic motion control of tetrahymena pyriformis using ferromagnetic nanoparticles—a tool to fabricate new class of microbiorobots,” *IEEE Applied Physics Letters*, vol. 97, no. 17, pp. 173–702, 2010.
- [5] P. S. S. Kim, A. Becker, Y. Ou, A. A. Julius, and M. J. Kim, “Imparting magnetic dipole heterogeneity to internalized iron oxide nanoparticles for microorganism swarm control,” *Journal of Nanoparticle Research*, vol. 17, no. 3, p. 144, 2015.
- [6] M. Gauci, J. Chen, W. Li, T. J. Dodd, and R. Groß, “Self-organized aggregation without computation,” *International Journal of Robotics Research*, vol. 33, no. 8, pp. 1145–1161, 2014.
- [7] M. Gauci, J. Chen, W. Li, T. J. Dodd, and R. Groß, “Clustering objects with robots that do not compute,” in *Proceedings of the International Conference on Autonomous Agents and Multi-agent Systems*, pp. 421–428, Paris, France, May 2014.
- [8] A. Ozdemir, M. Gauci, and R. Groß, “Shepherding with robots that do not compute,” in *Proceedings of 14th European Conference on Artificial Life*, pp. 332–339, Lyon, France, September 2017.
- [9] D. S. Brown, R. Turner, O. Hennigh, and S. Loscalzo, “Discovery and exploration of novel swarm behaviors given limited robot capabilities,” in *Proceedings of 13th International Symposium on Distributed Autonomous Robotic Systems*, pp. 447–460, London, UK, January 2016.
- [10] M. Gauci, *Swarm robotic systems with minimal information processing*, Ph.D. thesis, University of Sheffield, Sheffield, UK, 2014.
- [11] A. A. G. Requicha, “Nanorobots, NEMS, and Nanoassembly,” *Proceedings of the IEEE*, vol. 9, no. 11, pp. 1922–1933, 2003.
- [12] E. M. Purcell, “Life at low reynolds number,” *American Journal of Physics*, vol. 45, no. 1, pp. 3–11, 1977.
- [13] M. Benda, V. Jagannathan, and R. Dodhiawalla, “On optimal cooperation of knowledge sources,” Technical Report BCS-G2010-28, Boeing AI Center, Boeing Computer Services, Bellevue, WA, USA, 1986.
- [14] T. Haynes and S. Sen, “Evolving behavioral strategies in predators and prey,” in *Adaption and Learning in Multi-Agent Systems. IJCAI 1995*, G. Weiß and S. Sen, Eds., vol. 1042 of Lecture Notes in Computer Science (Lecture Notes in Artificial Intelligence), pp. 113–126, Springer, Berlin, Heidelberg, Germany, 1995.
- [15] T. Haynes, R. Wainwright, S. Sen, I. Sen, and D. Schoenefeld, “Strongly typed genetic programming in evolving cooperation strategies,” in *Proceedings of Sixth International Conference on Genetic Algorithms*, pp. 271–278, San Francisco, CA, USA, January 1995, <https://dl.acm.org/citation.cfm?id=657915>.

- [16] S. Luke and L. Spector, "Evolving teamwork and coordination with genetic programming," in *Proceedings of the First Annual Conference on Genetic Programming*, pp. 150–156, Stanford, CA, USA, 1996.
- [17] I. Tanev, M. Brzozowski, and K. Shimohara, "Evolution, generality and robustness of emerged surrounding behavior in continuous predators-prey pursuit problem," *Genetic Programming and Evolvable Machines*, vol. 6, no. 3, pp. 301–318, 2005.
- [18] R. Niu, D. Botin, J. Weber, A. Reinmüller, and T. Palberg, "Assembly and speed in ion-exchange-based modular photoretic microswimmers," *Langmuir*, vol. 33, no. 14, pp. 3450–3457, 2017.
- [19] M. Ibele, T. E. Mallouk, and A. Sen, "Schooling behavior of light-powered autonomous micromotors in water," *Angewandte Chemie International Edition*, vol. 48, no. 18, pp. 3308–3312, 2009.
- [20] F. Martinez-Pedrero, H. Massana-Cid, and P. Tierno, "Assembly and transport of microscopic cargos via reconfigurable photoactivated magnetic microdockers," *Small*, vol. 13, no. 18, article 1603449, 2017.
- [21] I. Tanev, M. Georgiev, K. Shimohara, and T. Ray, *Evolving a Team of Asymmetric Predator Agents That Do Not Compute in Predator-Prey Pursuit Problem*, AIMS, 2018.
- [22] J. Holland, *Adaptation in Natural and Artificial Systems*, The University of Michigan, Ann Arbor, MI, USA, 1975.
- [23] E. Goldberg, *Genetic Algorithms in Search, Optimization and Machine Learning*, Addison-Wesley, Boston, MA, USA, 1989.
- [24] M. Mitchell, *An Introduction to Genetic Algorithms*, MIT Press, Cambridge, MA, USA, 1998.
- [25] S. Nolfi and D. Floreano, *Evolutionary Robotics: The Biology, Intelligence, and Technology of Self-Organizing Machines*, MIT press, Cambridge, MA, USA, 2000.
- [26] M. Georgiev, I. Tanev, K. Shimohara, and T. Ray, "Evolution, robustness and generality of a team of simple agents with asymmetric morphology in predator-prey pursuit problem," *Information*, vol. 10, no. 2, p. 72, 2019.
- [27] M. Georgiev, I. Tanev, and K. Shimohara, "Coevolving behavior and morphology of simple agents that model small-scale robots," in *Proceedings of the Genetic and Evolutionary Computation Conference Companion (GECCO)*, pp. 1576–1583, Kyoto Japan, July 2018.
- [28] M. Georgiev, I. Tanev, and K. Shimohara, "Exploration of the effect of uncertainty in homogeneous and heterogeneous multi-agent societies with regard to their average characteristics," in *Proceedings of the Genetic and Evolutionary Computation Conference Companion (GECCO)*, pp. 1797–1804, Kyoto Japan, July 2018.
- [29] P. J. Angeline and K. E. Kinnear Jr., "Genetic programming and emergent intelligence," in *Advances in Genetic Programming*, pp. 75–98, MIT Press, Cambridge, MA, USA, 1994.

## Research Article

# Discrimination of Motion Direction in a Robot Using a Phenomenological Model of Synaptic Plasticity

Nareg Berberian , Matt Ross, and Sylvain Chartier

Laboratory for Computational Neurodynamics and Cognition, School of Psychology, University of Ottawa, Ottawa, ON, Canada K1N 6N5

Correspondence should be addressed to Nareg Berberian; [nberb062@uottawa.ca](mailto:nberb062@uottawa.ca)

Received 12 October 2018; Revised 14 February 2019; Accepted 19 March 2019; Published 2 May 2019

Guest Editor: Uma Seeboonruang

Copyright © 2019 Nareg Berberian et al. This is an open access article distributed under the Creative Commons Attribution License, which permits unrestricted use, distribution, and reproduction in any medium, provided the original work is properly cited.

Recognizing and tracking the direction of moving stimuli is crucial to the control of much animal behaviour. In this study, we examine whether a bio-inspired model of synaptic plasticity implemented in a robotic agent may allow the discrimination of motion direction of real-world stimuli. Starting with a well-established model of short-term synaptic plasticity (STP), we develop a microcircuit motif of spiking neurons capable of exhibiting preferential and nonpreferential responses to changes in the direction of an orientation stimulus in motion. While the robotic agent processes sensory inputs, the STP mechanism introduces direction-dependent changes in the synaptic connections of the microcircuit, resulting in a population of units that exhibit a typical cortical response property observed in primary visual cortex (V1), namely, direction selectivity. Visually evoked responses from the model are then compared to those observed in multielectrode recordings from V1 in anesthetized macaque monkeys, while sinusoidal gratings are displayed on a screen. Overall, the model highlights the role of STP as a complementary mechanism in explaining the direction selectivity and applies these insights in a physical robot as a method for validating important response characteristics observed in experimental data from V1, namely, direction selectivity.

## 1. Introduction

Although a seemingly effortless task for humans, recognizing and tracking the direction of visual objects is based on an incredible complexity of brain areas involved in visual processing and attention, as well as learning and memory. In recent years, the advent of artificial neural networks (ANNs) has allowed the combination and isolation of the interactions of important biophysical mechanisms in order to shed light on the nature of biological phenomena. Through a symbiotic collaboration between neuroscience and artificial intelligence, the application of ANNs is in part to unify our understanding of the underlying mechanisms contributing to sensory experience. The development of these brain-inspired computational systems have shown their usefulness in revealing novel mechanisms of neuronal circuitry and in proposing experimental predictions that can be directly tested in experimental settings. In order to elucidate

the circuit mechanisms underlying visual perception, mathematical models have been formulated with strong support from electrophysiological data [1]. Due to their usefulness and their predictive ability in driving new neuroscientific discoveries, brain-inspired ANNs also have the potential to be implemented in robotic agents in order to further assess their ecological validity [2]. Given that mechanistic models cannot yet capture the full complexity of the nature of perceptual phenomena, the implementation of well-established models from neuroscience into the domain of artificial intelligence opens new avenues for understanding biological networks exposed to real-world stimuli [3]. Previous approaches in modelling the perceptual phenomena of motion have shown successful attempts in incorporating natural visual inputs in networks of spiking neurons [4–6].

In this study, we propose a model of motion discrimination using a ubiquitous mechanism in neuronal circuits,



namely, short-term plasticity (STP), whereby the strength of synaptic connections varies from milliseconds to seconds as a result of recent activity [7, 8]. These rapid changes in synaptic strength vary overtime from one spike to the next due to short-term facilitation (STF) and short-term depression (STD) [9]. Short-term synaptic plasticity serves diverse functions in bio-inspired networks. For example, STP can process temporal patterns [10], modify a neuron’s sensitivity to the temporal coherence of inputs [11, 12], participate in gain control [12], reduce redundancy [13], act as an adaptive filter [14], and improve discriminability [15] among others [16]. Despite the beneficial effects of STP on cortical computation [7, 8, 10, 16–18], it remains unclear whether STP contributes independently of sensory experience or whether it provides a causal contribution to experience-dependent plasticity. A study in-line with the former found that alteration in STP has been observed in cultural neurons, suggesting that endogenous neuronal activity (i.e., independent of sensory experience) is sufficient to drive changes in STP [19]. In contrast, there is evidence to suggest that STP is a consequence of experience-dependent plasticity in local neuronal circuits and therefore causally linked to visually driven inputs [20–25]. For example, sensory deprivation can alter STP, but in most cases, the dynamics of synaptic transmission are often inconsistent in these experiments, as even at the same synapse type, some promote facilitation while others will exhibit depression. Nonetheless, evoked and spontaneous vesicle release is likely to be controlled by two independent and nonoverlapping mechanisms [26]. Sensory experience can therefore modify the dynamics of STP, thus pointing towards a causal contribution of STP to experience-dependent plasticity. Indeed, an important determinant of development and sensory-driven alteration in STP is the expression of presynaptic NMDA receptors (preNMDARs) [27, 28]. These are ligand-gated ionotropic glutamate receptors that serve diverse functions ranging from the coincidence detection in Hebbian learning to excitatory neurotransmission critical for information processing in the mammalian central nervous system [29].

In layers 2/3 (L2/3) of the primary visual cortex (V1), individual neurons respond more strongly to an object (i.e., orientation grating) moving in a particular direction (“preferred”) than the same object moving in the opposite direction (“null”); a visual response property termed direction selectivity. There is surmounting experimental and theoretical evidence that STP contributes to the enhancement of motion discrimination [30–33]. In-line with previous studies, we recently found that rapid changes in synaptic strength via STP may provide an essential contribution for accurate motion discrimination [34]. Starting with the well-established Tsodyks–Markram model [1], we implement STP in the synaptic connections of a microcircuit motif. We then examine neuronal responses to changes in the direction of real-world vertical orientation stimuli moving in bidirectional motion along a single axis of motion. Furthermore, we compare neuronal responses in real-time from a robotic implementation to those of a simulated version of the model whereby units are instead exposed to a

hypothetical version of real-world stimuli in motion. Finally, we analyse neuronal responses in V1 to drifting sinusoidal gratings and compare cortical responses to those observed in the robotic implementation. The remainder of the paper is divided as follows: Section 2 describes the architecture of the microcircuit motif, the setup of the robotic implementation, and the phenomenological model of STP and summarizes the experimental data analysis approach. Section 3 illustrates all findings. In Sections 4 and 5, we summarize the overall insights of our work, propose future avenues, and highlight the contribution of our work to neurorobotics research.

## 2. Materials and Methods

**2.1. Architecture.** Here, we propose a microcircuit motif of six units in total, comprised of two subpopulations connected via synapses that exhibit STF (Figure 1). This novel framework differs from our previously proposed architecture of two units mediated by STD- and STF-dominated synaptic connections [34]. In our current study, we aim to provide a more parsimonious approach in highlighting the contribution of STP by using a single STP mechanism rather than two distinct STP mechanisms for showing successful motion discrimination. In addition, we highlight the structural advantages of the expanded network over the two-unit microcircuit. Finally, we display the functional advantages resulting from the topological structure of the expanded network, which happen to be absent in a two-unit microcircuit.

In order to assess whether the embodied robot is capable of displaying response characteristics similar to those observed in local microcircuits in V1, the architecture is expanded by following a constrained network topology inspired from specific features observed in local cortical microcircuits. For example, bidirectional connectivity in V1 is a by-product of neighbouring neurons sharing similar visual responses [35]. In addition, bidirectional connectivity has been suggested to evolve according to synaptic connections mediated by STF [36]. Furthermore, neurons in V1 that share similar visual features (e.g., similar direction preference) are more highly connected and less connected to neurons showing a reduced preference for those similar visual features [35]. Similarly, in our expanded microcircuit, there are a greater number of connections amongst units exhibiting the same direction preference and less connections between units coding for an opposing direction of motion (Figure 1) [37]. More specifically, units 1, 2, and 3 within subpopulation 1 are more highly connected amongst each other and less connected to units 4, 5, and 6 within subpopulation 2. These topological features of the expanded network would be absent in a two-unit microcircuit with bidirectional connections because both units would exhibit the same number of outgoing and incoming connections, acting as a single isolated subpopulation. Consequently, we hypothesized that, in the expanded architecture, units within subpopulation 1 and subpopulation 2 would exhibit preferential responses to opposing directions of motion. In contrast, we expected that a microcircuit of two units with bidirectional connections would have a limited functional

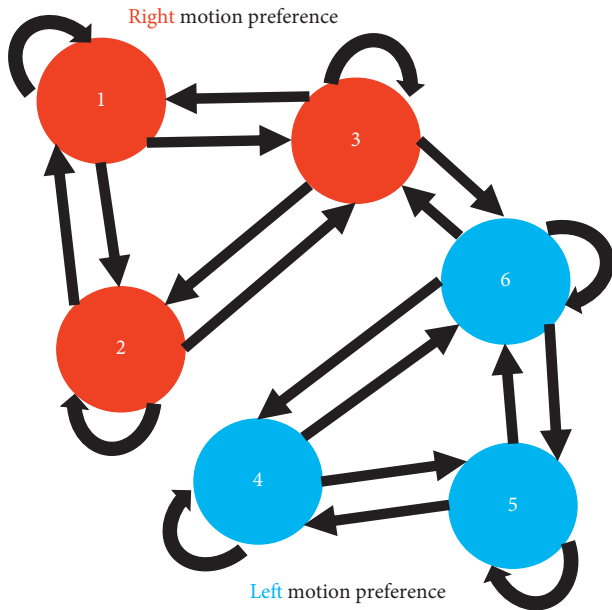


FIGURE 1: Architecture of the microcircuit. There are 6 units in total. Subpopulation 1 (red) forms a cluster of 3 units, each of which exhibits a preference for stimuli moving towards the right. The remaining units in subpopulation 2 (blue) display higher responses for stimuli moving towards the left. Connections are bidirectional, with self-connections allowed. Outgoing connections from units within both subpopulations exhibit STF.

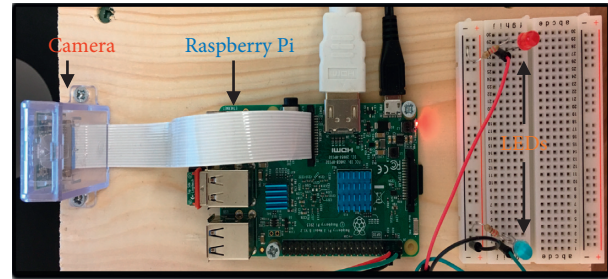
contribution by displaying preference only for a single direction of motion. Finally, it is noteworthy to mention that the study proposed here has extended the architecture to six units, as network size from this point forward would not change the desired behaviour of individual units in the model but simply increase simulation time.

**2.2. Setup.** For the robotic implementation, we have employed the Raspberry Pi 3 Model B-V1.2 microcontroller (Figure 2(a)). To capture the image of the stimulus in motion, a Raspberry Pi camera (V2.1) is used and attached to the device via a ribbon cable. In addition, two simple circuits are created on a breadboard responsible for lighting up coloured LEDs (red and blue) and attached to the Raspberry Pi's GPIO (general purpose input/output) pins. The robotic setup is mounted onto a wooden box, and the camera is placed 12 centimeters away from the front of a computer monitor whereby real-world stimuli are displayed (Figure 2(b)).

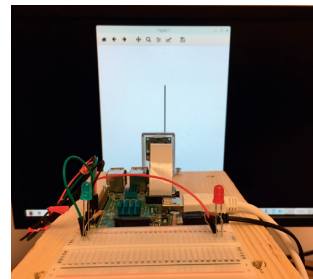
**2.3. Model.** Using the robotic implementation, we incorporate the mechanism of STP within the microcircuit, whereby the neurotransmitter release probability in the synaptic connections evolves according to

$$\frac{du_j}{dt} = \frac{U - u_j(t)}{\tau_f} + U(1 - u_j(t)) \sum_{k=0}^{\infty} \delta(t - t_k^{(j)}), \quad (1)$$

where  $\delta(t)$  is the Dirac delta function. The sum on  $k$  spikes is over all spike times  $t_k^{(j)}$  of presynaptic neuron  $j$ , and  $u_j(t)$



(a)



(b)

FIGURE 2: Robotic setup. (a) Setup of the camera, Raspberry Pi, and the LEDs. (b) Overview of the robotic setup in front of a computer monitor displaying an orientation stimulus from the real-world.

reflects presynaptic residual calcium levels. In the absence of incoming action potentials, the synapse is at a resting state with residual calcium levels  $u_j(t_0) = U$ . The amount of residual calcium instantaneously increases immediately after the first action potential within a spike train, and  $u_j(t_1) = 1 - u_j(t_0)$  is the fraction that remains available immediately after this first event. Hence, the running variable of  $U$  refers to  $u_j(t)$ , and  $U$  remains a parameter that applies to the first action potential in the spike train, after which  $u_j(t)$  (the running variable of  $U$ ) decays exponentially to its resting value  $U$  with a time constant  $\tau_f$ . As a result, each time an action potential is generated, presynaptic residual calcium instantaneously rises and then recovers with a time constant  $\tau_f$  between subsequent spikes. As residual calcium levels increase, a release-ready vesicle along the active zone of the presynaptic membrane terminal releases neurotransmitters onto the postsynaptic side of the synapse. During this process of exocytosis, the neurotransmitter availability within the presynaptic terminal is described according to

$$\frac{dx_j}{dt} = \frac{1 - x_j(t)}{\tau_d} - u_j(t)x_j(t) \sum_{k=0}^{\infty} \delta(t - t_k^{(j)}), \quad (2)$$

where  $x_j(t)$  denotes the fraction of resources that remain available following vesicle release. Between subsequent spikes,  $x_j(t)$  recovers back to baseline to its resting value of 1 with a time constant  $\tau_d$ , restoring the amount of synaptic resources available within the presynaptic terminal. The STP model allows the examination of synaptic behaviour under a relatively short timescale. Hence, here we are interested in the properties and mechanisms of plasticity over the course of milliseconds to seconds [7]. Depending on the initial setup of kinetic parameters  $\tau_f$ ,  $\tau_d$ , and  $U$ , the STP model can

mimic the effect of a depressing or a facilitating synapse (Table 1) [1]. Therefore, the mechanism of STD and STF can be distinguished using a different parameter setup in the same governing Equations (1) and (2).

In this study, images that the camera captures from the sensory environment are used as direct input into the microcircuit motif. In other words, external inputs directly generate incoming presynaptic spikes in the STP model. In order to receive synaptic inputs, the stationary camera is used to process changes in the visual image captured from the sensory environment. The generated image is displayed on a computer monitor and is characterized by a 24 bit colour scheme. This setup provides the advantage in presenting moving stimuli that follow a spatiotemporal pattern. Furthermore, we decided to mimic a similar stationary screen fixation setup used in experimental neuroscience [38–40], where an anesthetized, paralyzed animal exhibits minimal eye movements to moving stimuli displayed on the screen. As for the nature of the stimulus presented, we are interested in black and white images. Hence, an average of the three 8 bit RGB planes is taken, and the resulting plane is then converted such that every pixel inside the plane is coded by 1 (black pixel) or 0 (white pixel), instead of traditional values ranging from 0 to 255 (where 255 is the maximal intensity that could be displayed). The conversion of the image to a binary scheme allows us to directly feed the microcircuit with trains of incoming “all-or-none” action potentials as the camera processes visual images, similar to previous methods [6]. The Raspberry Pi camera has a native resolution of  $3280 \times 2464$  (Figure 3). Two steps were applied to down sample the stimulus image and thus simplify input to the network. Firstly, the camera resolution was lowered to  $100 \times 1000$ , in order to allow a visible preview of the image processed by the camera. When the stimulus is displayed on the computer monitor, the vertical line extends across the entire first dimension and therefore activates all units in the network (Figure 3). Here, the first dimension of 100 is meant to represent the number of units to receive the input. Given that the network is comprised of six units, there are 94 remaining units along the first dimension (i.e., rows) serving as redundant information to the network. Hence, to remove redundant information presented to the network, the dimensionality was further reduced to  $6 \times 1000$ , where each row serves as input to a single unit in the network and each column describes the amount of time needed to evaluate the activity of each unit during visual information processing.

In this way, the camera captures an image of 6000 pixels which is then directly introduced as input to the spiking network. It is noteworthy to mention that the number of presynaptic spikes that each unit receives is equal to the number of 1s encoded in the pixelated image processed from the camera. In other words, the greater the width of the orientation bar, the greater the number of pixels coded with 1s and, therefore, the higher the frequency of the presynaptic inputs. In addition, individual shifts in the orientation stimulus in motion will also shift the timing of presynaptic spikes. Finally, given the nature of the real-world stimulus, images were inherently noisy, meaning some units received a few more input spikes than others. This inherent feature

TABLE 1: Short-term synaptic plasticity parameters.

Parameters	Values STF
Facilitation recovery ( $\tau_f$ )	750 ms
Depression recovery ( $\tau_d$ )	50 ms
Initial neurotransmitter availability ( $x$ )	1
Multiplicative factor ( $A$ )	0.039

potentially originated from fluctuations in luminance and/or the angle of the monitor relative to the lens of the camera.

In the model, there are a total of 200 direction steps, where each direction step represents a shift in the orientation stimulus, which is captured by using the camera. Therefore, the camera captures 200 images, 100 of which are comprised of orientation stimuli moving towards the right and the remaining 100 images are comprised of orientation stimuli moving towards the left. For individual shifts in the image, the network receives a new train of incoming presynaptic inputs for a total of 1000 ms (Table 2). When dealing with temporal coding tasks, it is necessary to manipulate the initial vesicle release probability  $U$  (Equation 1) [10]. Here, changes in direction steps introduce changes in the initial release probability of STF-mediated units in the microcircuit motif [34]. The range of values used to modulate the initial vesicle release probability is presented in Figure 4(a). For every direction step of the stimulus in motion, we recruited a pair of initial vesicle release probabilities, one of which was recruited by units within subpopulation 1, and the remaining one was recruited by units within subpopulation 2. Hence, a single change in the direction step introduced a new pair of initial release probabilities, which in turn mediated neuronal responses across time. Based on the temporal dynamics of synaptic transmission, units would in turn display preferential and nonpreferential responses to orientation stimuli in motion. The average initial release probability for left and right motions from each respective subpopulation shows that units within subpopulation 1 exhibit a higher initial release probability for right motion, whereas units within subpopulation 2 exhibit a higher initial release probability for left motion (Figure 4(b)).

As units receive visual input, the kinetic parameters modulate the interplay between the dynamics of  $u_j(t)$  and  $x_j(t)$ . In turn, the joint effect of  $u_j(t)x_j(t)$  characterizes the short-term strength of the synaptic inputs at a given time step, thus generating an instantaneous current characterized by

$$I_i^{\text{stf}}(t) = A \sum_{j=1}^N w_{ij} u_j(t) x_j(t), \quad (3)$$

where the summation is taken over all presynaptic inputs. Here,  $w_{ij}$  is the absolute synaptic efficacy from presynaptic unit  $j$  to postsynaptic unit  $i$  mediated by the temporal dynamics  $u_j(t)x_j(t)$  of STP [41]. For each direction step,  $w_{ij}$  is kept constant and set to 1 if unit  $j$  is connected to the unit  $i$ , otherwise it is set to 0, denoting the absence of a connection. In this way, the temporal dynamics of the instantaneous current  $I_i^{\text{stf}}(t)$  is mostly mediated by STP.  $A$  is a constant

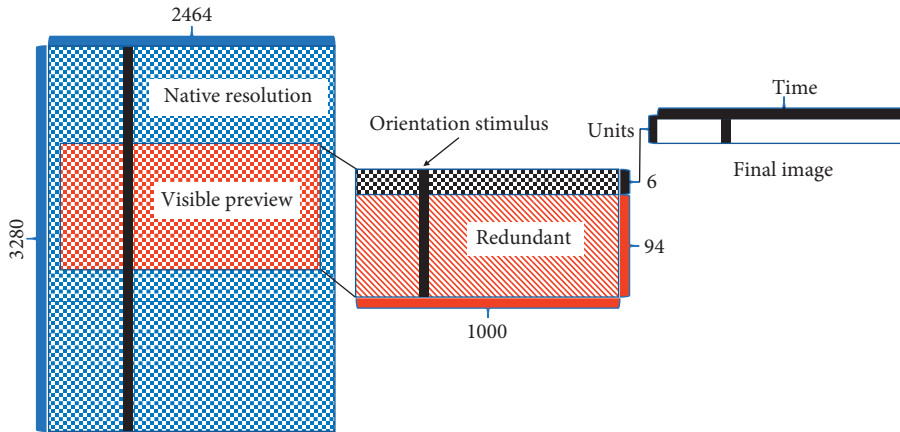


FIGURE 3: Schematic representation displaying the transformation starting from the native resolution of the Raspberry Pi camera up to the final image displayed to the robot.

TABLE 2: Leaky integrate-and-fire parameters.

Parameters	Values
Spike emission threshold ( $\theta$ )	-55 mV
Resting membrane potential ( $V_{rest}$ )	-70 mV
Membrane resistance ( $R_m$ )	200 m $\Omega$
Membrane time constant ( $\tau_m$ )	30 ms
Absolute refractory period ( $\tau_{arp}$ )	2 ms
Integration time step ( $dt$ )	1 ms
Stimulus duration ( $T$ )	1000 ms

multiplicative factor, modulating the overall gain of the generated current. The current mediated by STP drives subthreshold membrane potential depolarization dynamics of leaky integrate-and-fire (LIF) units according to

$$\tau_m \frac{dV_i}{dt} = -V_i(t) + V_{rest} R_m I_i^{stp}(t), \quad (4)$$

where  $\tau_m$  is the membrane time constant,  $I_i^{stp}(t)$  is the current mediated by the short-term synaptic strength, and  $R_m$  is the membrane resistance. Whenever a depolarization hits a fixed threshold ( $V_i(t) \geq \theta$ ), the unit emits a spike and becomes refractory for a period  $\tau_{arp}$ , after which Equation 4 resumes from a subthreshold reset potential  $V_{rest}$  (Table 2).

**2.4. Experimental Data.** To draw a parallel between the responses of spiking units observed in the real-time robotic implementation versus those observed in an experimental setting, we analysed data from V1 of visually evoked activity in anesthetized macaque (*Macaca fascicularis*) monkeys. Resulting recordings were mostly confined to layers 2/3, an area where orientation and direction selectivity are cortical response properties prominently observed. The data were collected in the Laboratory of Adam Kohn at the Albert Einstein College of Medicine and downloaded from the CRCNS website [42]. Hence, the dataset is taken from previous work where the experimental procedures are described in detail [38–40]. Briefly, extracellular recordings were performed using Utah microelectrode arrays inserted 0.6 mm into cortex. Animals were paralyzed to minimize eye

movements. All experimental procedures complied with guidelines approved by the Albert Einstein College of Medicine of Yeshiva University and New York University Animal Welfare Committees.

The spiking activity of neurons was recorded while presenting full-contrast drifting sinusoidal gratings presented at 12 orientations spaced equally (30°). Drifting gratings were presented binocularly for 1.28 seconds and separated by 1.5 seconds intervals during which a gray screen was presented. Stimulus orientation was randomized, and each stimulus was presented 200 times (i.e., trials). The evoked dataset consisted of spiking activity from 59 to 105 neurons from 3 monkeys (dataset 1, 2, and 3, respectively). To characterize neuronal responses, we chose dataset 3, which included the most amount of neurons (105) out of all 3 datasets. For each orientation of the stimulus moving in the bidirectional motion, the trial-averaged firing rate of individual neurons was computed.

In V1, and other areas of the brain, neurons exhibit high trial-by-trial fluctuations in firing rate [43]. Regardless of the nature of the stimulus and the behavioural state of the animal, a widespread feature of cortical responses is the reduction in trial-by-trial variability around 100 ms following the onset of the stimulus [44]. Given that stimulus onset quenches neuronal variability, estimated neuronal responses following a certain delay would in turn provide a more accurate response representation of visual information. Hence, we computed the firing rate of individual cells during the remaining 1 second of the recordings, rather than the entire 1.28 seconds to ensure a decline in neuronal response variability. Furthermore, to remain consistent with the paradigm of the real-time robotic implementation, we analysed the spiking activity of 6 neurons in the dataset. While neuronal responses for all orientation gratings were analysed, we focused on finding neurons exhibiting higher responses exclusively for the vertical orientation gratings; the same orientation was processed by using the camera of the robot. Consequently, we chose 3 neurons (30, 63, and 103) from the dataset exhibiting preferential responses for vertical sinusoidal gratings moving towards the right and nonpreferential responses in the opposite null direction.

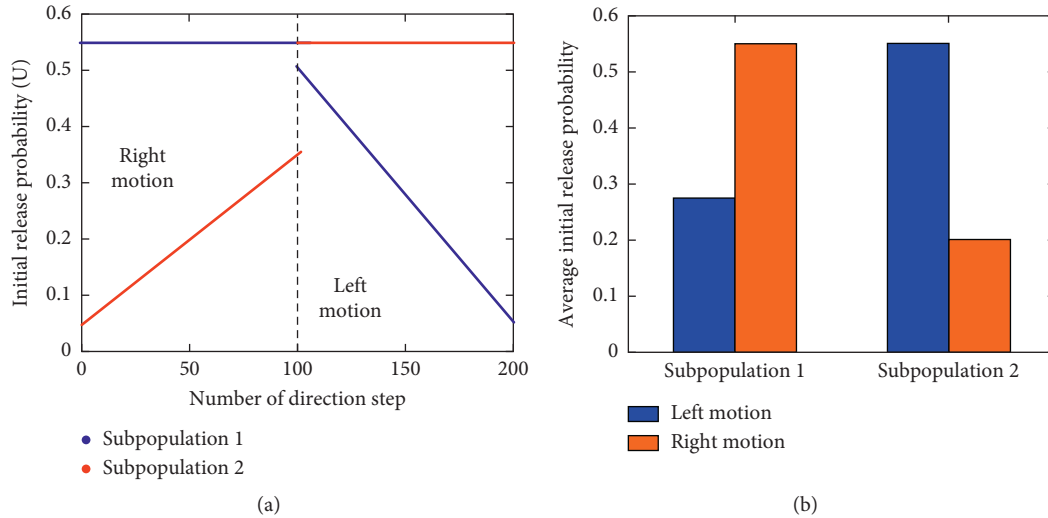


FIGURE 4: Initial release probability in the synaptic connections as a function of the direction step number. (a) Pair of initial release probabilities recruited during left and right motion discrimination. (b) Average initial release probability for left and right motion in the STF-mediated synaptic connections of subpopulation 1 and subpopulation 2.

Conversely, we chose 3 other neurons (5, 42, and 98) from the same dataset exhibiting preferential responses to stimuli moving left and nonpreferential responses in the opposite null direction.

### 3. Results

Figure 5 illustrates the visually evoked activity of individual units, where an orientation stimulus exhibits a rightward motion along a single axis. In this scenario, the activity of the microcircuit is dominated by the response of units within subpopulation 1, where units within this subpopulation exhibit a preferential response for stimuli moving towards the right. Higher responses for right motion discrimination are indicated by the activation of the red LED (Figure 5(a)). Figure 5(b) illustrates a snapshot of the image captured by the camera during the time at which the stimulus is moving towards the right. Figure 5(c) displays the presynaptic input to each unit within the microcircuit, whereas Figure 5(d) illustrates the visually evoked activity of individual units within the microcircuit during right motion discrimination.

Figure 6 illustrates the activity of individual units to a stimulus moving towards the left. Here, the activity of the microcircuit is dominated by the response of units within subpopulation 2. Higher responses from subpopulation 2 are in turn represented by the activation of the blue LED (Figure 6(a)). An image of the vertical orientation stimulus is displayed in Figure 6(b), resulting in direct incoming action potentials in the microcircuit illustrated in Figure 6(c). Figure 6(d) illustrates the visually evoked activity of individual units within the microcircuit during left motion discrimination. A video illustration of the real-time robotic implementation and the corresponding spatiotemporal patterns of activity of all six units can be found in Supplementary Material (see S1 for video illustration).

Figure 7 displays the average firing rate of units within subpopulations 1 and 2 exposed to stimuli moving in

bidirectional motion. The visually evoked response of both subpopulations is shown when the model is exposed to hypothetical stimuli (Figure 7(a)) and real-world stimuli (Figure 7(b)). Units within subpopulation 1 exhibit a preferential response to orientation stimuli moving towards the right. Conversely, units within subpopulation 2 show a higher response to stimuli moving towards the left. Under both scenarios, the average firing rate of units in the preferred and nonpreferred direction is highly close to that observed amongst direction-selective neurons in V1 responding to drifting sinusoidal gratings (Figure 7(c)). Figure 7(d) displays the average response of the direction-selective cells of interest across all orientations and directions. Among these responses, those resulting from vertical gratings are displayed in Figure 7(c). In subpopulation 1, the trial-averaged response of 3 cells shows preferential responses for right motion. In subpopulation 2, the trial-averaged response of 3 cells displays preference for left motion.

Figure 8 illustrates the temporal dynamics of the synaptic variables  $x_j(t)$  and  $u_j(t)$  as the microcircuit process visual information. During motion discrimination, units within both subpopulations display synaptic connections that require similar amounts of synaptic resources available in order to properly mediate the response of both subpopulations. Furthermore, the average amount of neurotransmitters available is kept within a high range across the entire temporal domain (Figure 8(a)). This suggests that units within the microcircuit are minimizing use-dependent alterations of synaptic transmission during bidirectional motion discrimination, a scenario that is particularly advantageous when future task demands are required for the robot to perform. Finally, the examination of the release probability in the synaptic connections suggests that units within subpopulation 1 exhibit a higher neurotransmitter release probability for stimuli moving towards the right. On the contrary, synaptic connections within subpopulation 2

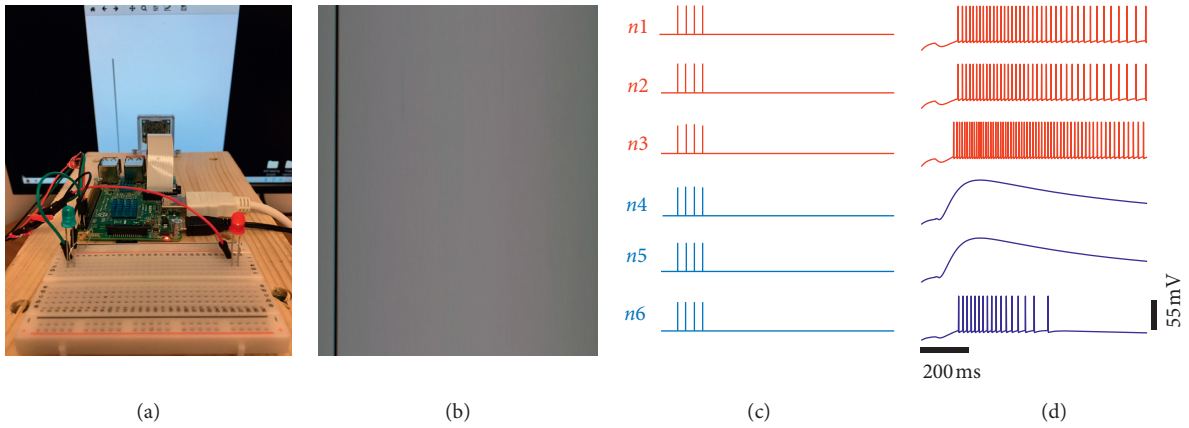


FIGURE 5: Right motion discrimination. (a) Activation of the red LED in response to a stimulus moving towards the right. (b) Real-world stimulus processed by using the Raspberry Pi camera. (c) Trains of presynaptic spikes fed to each unit in the microcircuit. (d) Postsynaptic response of individual units.

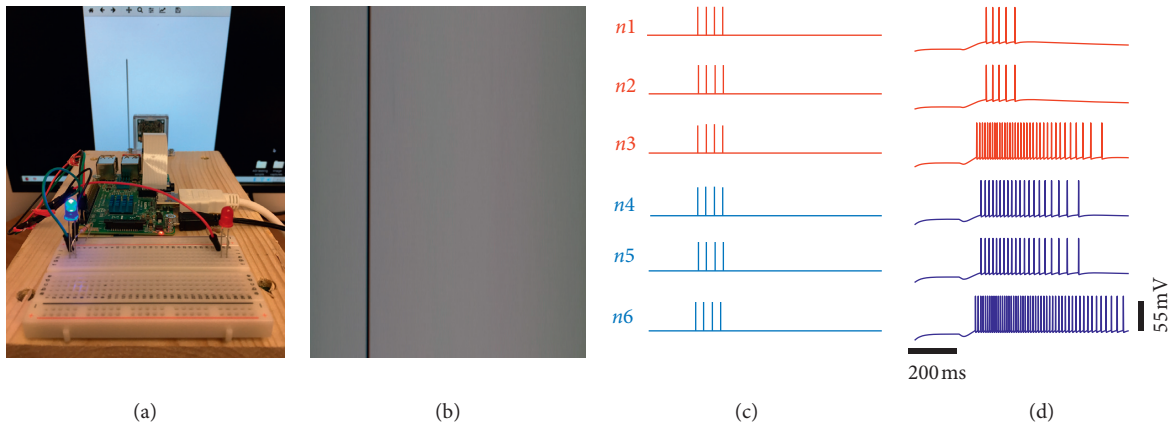


FIGURE 6: Left motion discrimination. (a) Activation of the blue LED in response to a stimulus moving towards the left. (b) Real-world stimulus processed by using the Raspberry Pi camera. (c) Trains of presynaptic spikes fed to each unit in the microcircuit. (d) Postsynaptic response of individual units.

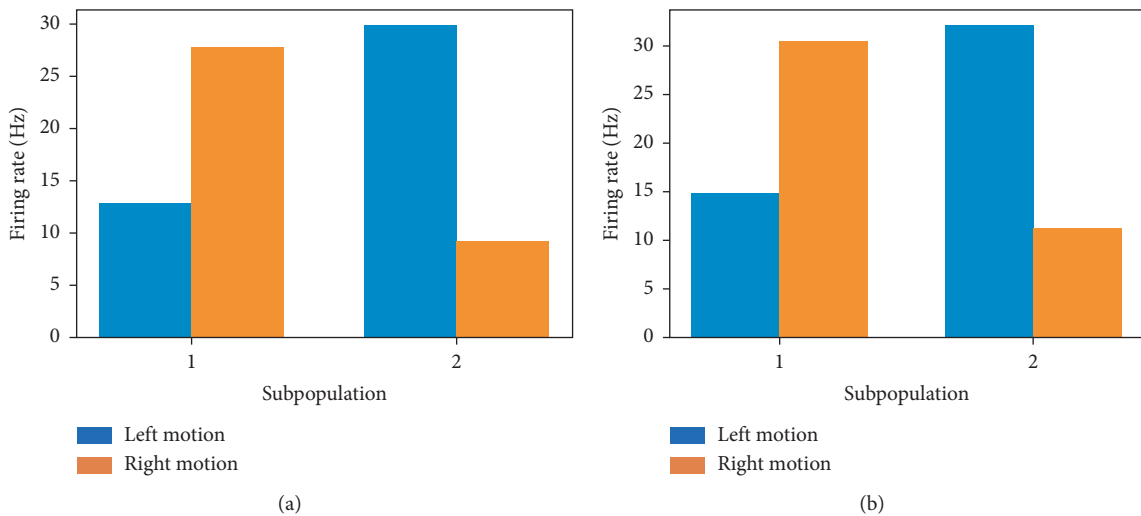


FIGURE 7: Continued.

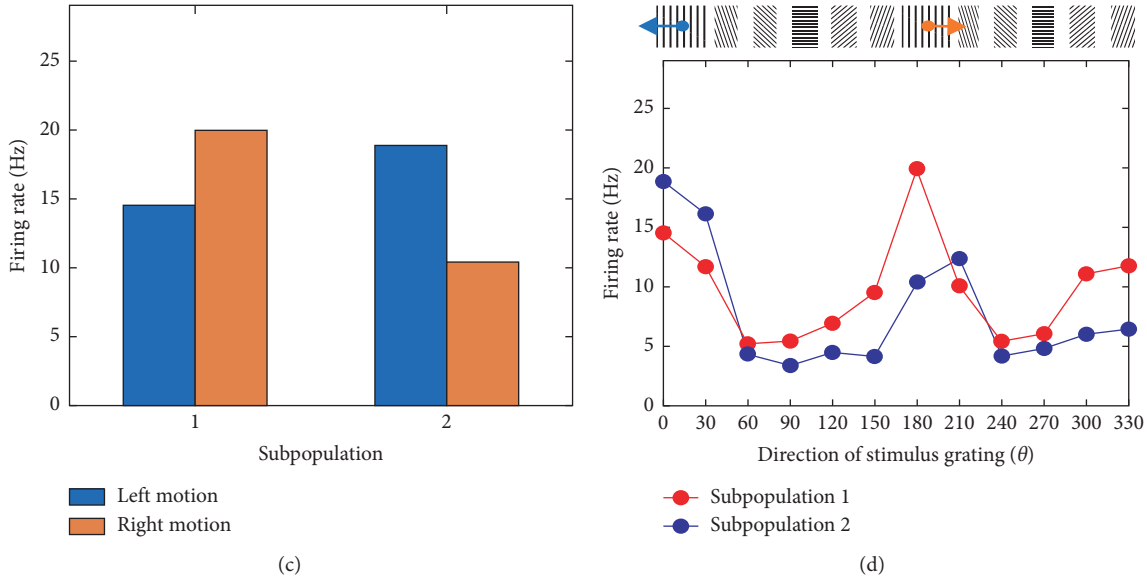


FIGURE 7: Response of 2 subpopulations during the simulation, real-time robotic implementation, and microelectrode recordings of V1. (a) Responses to hypothetical stimuli tested in the model. (b) Responses to real-world stimuli tested in the robot. (c) Responses to vertical sinusoidal gratings tested on a macaque monkey. (d) Responses to sinusoidal gratings presented at 12 orientations tested on a macaque monkey.

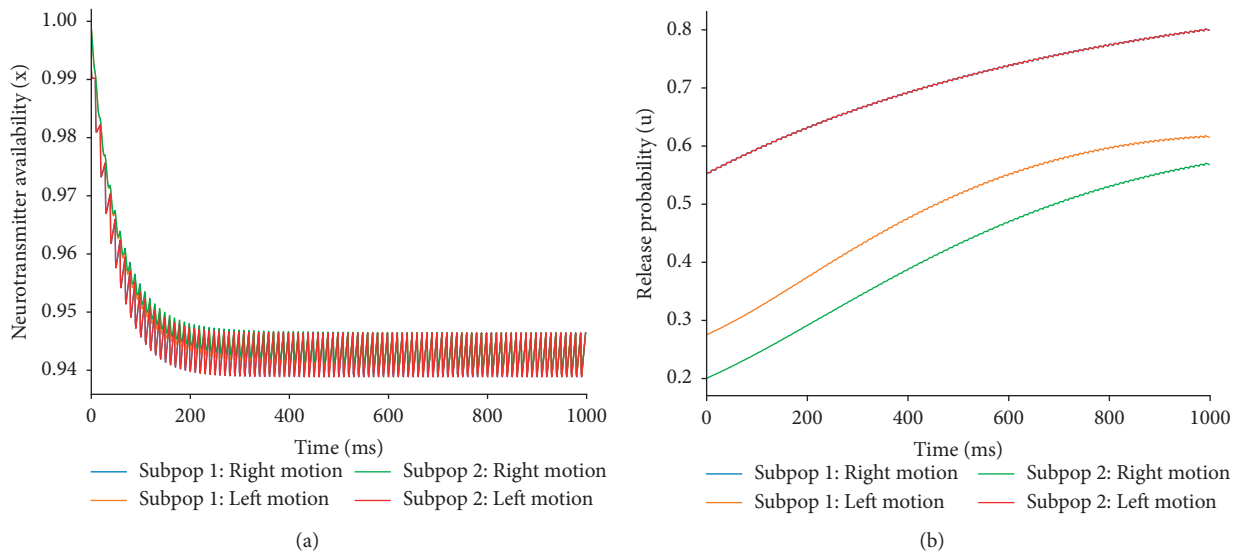


FIGURE 8: Parameters related to the efficacy of synaptic transmission during left and right motion discrimination. (a) Average synaptic resources available within each subpopulation. (b) Average neurotransmitter release probability in the synaptic connections within each subpopulation. Notice that the temporal evolution of the release probability is the same for subpop 1-right motion and subpop 2-left motion because their average initial release probability recruited for left and right motion is the same (Figure 4(b)).

display a higher neurotransmitter release probability for stimuli moving towards the left (Figure 8(b)). This suggests that when the microcircuit is exposed to stimuli moving in a specific direction, units that exhibit preferential responses to stimuli moving in the specified direction are most likely to be mediated by synaptic connections that exhibit a high release probability [45].

Next, we examined whether the topological structure of our expanded network adds functionality that would otherwise be absent in a two-unit microcircuit. In order to

maintain a consistent comparison between the expanded network and the two-unit microcircuit, all of the synaptic connections were mediated by STF (Figure 9(a)). In addition, we examined the activity of each unit using the same kinetic parameters  $\tau_f$  and  $\tau_d$  (Table 1). Furthermore, we presented the same hypothetical stimulus in motion and recruited the same pairs of initial release probabilities  $U$  (Figure 4(a)). Under this framework, both units display highly synchronized spatiotemporal patterns of activity to stimuli moving in bidirectional motion (see S2 in

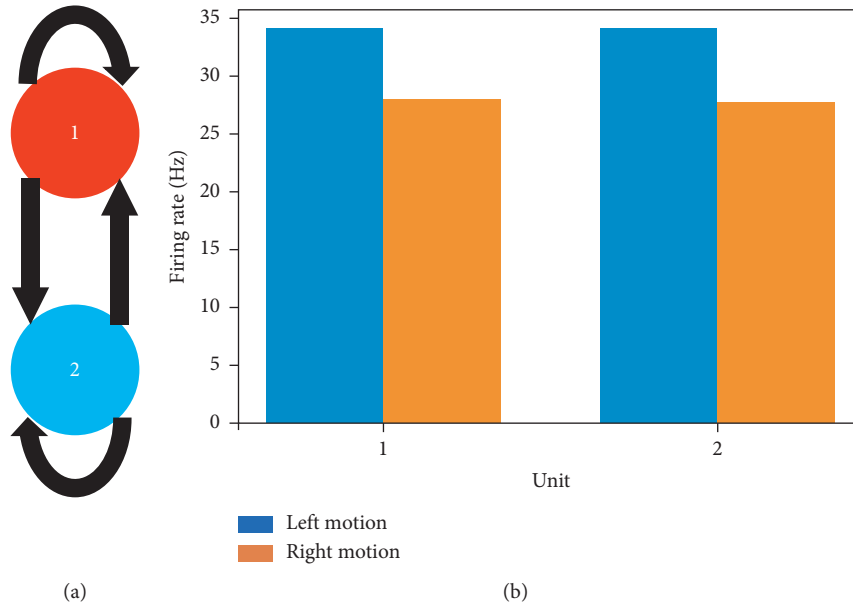


FIGURE 9: Direction selectivity in the two-unit model. (a) Architecture of the microcircuit. There are 2 units in total. (a) Outgoing connections from unit 1 and unit 2 exhibit STF. Connections are bidirectional, with self-connections allowed. (b) Average response of two units to a hypothetical stimulus moving in bidirectional motion. Unit 1 and unit 2 exhibit the same preference in response to opposite directions of motion. Besides keeping all other parameters the same, the default multiplicative factor  $A$  (Table 1) was multiplied by 2, in order to ensure that the mean activity of units falls within a similar range as that of the six-unit microcircuit (Figures 7(a) and 7(b)).

Supplementary Material for video illustration). In addition, the two-unit microcircuit behaves as a single subpopulation, displaying preference only for a single direction of motion (Figure 9(b)). In contrast, the topological structure of the expanded network divides units into two distinct subpopulations, each of which displays preference for a direction opposite to that of its neighbouring subpopulation (Figure 7(a)). Taken together, the two-unit model limits the functional contribution of the microcircuit by displaying preference only for a single direction of motion, whereas the expanded architecture embodies a topological structure that lays the foundation for displaying preferential responses to both directions of motion.

In cortical microcircuits including V1, neurons exhibit shared fluctuations in population activity overtime [46]. In general, these shared fluctuations are measured between pairs of neurons over multiple presentations of an identical stimulus. To examine these coordinated fluctuations in spiking activity, we used a measure of spike count correlation (SCC) between pairs of neurons in V1 during motion discrimination [47]. In doing so, we used a nonoverlapping time window of 1 millisecond to compute the total number of spikes emitted from each neuron at a given time step. In this way, we obtained the total spike count of individual neurons across time over multiple presentations of the same stimulus in motion. We then computed the pairwise correlation coefficient matrix between 6 neurons, representing the SCC between all pairs of neurons. Finally, we computed the mean SCC observed between pairs of neurons within and between subpopulations. In doing so, we find a positive SCC within subpopulations, and a negative SCC between subpopulations (Figure 10(a)). Interestingly,

a positive “within” SCC predicts that fluctuations in the activity of neurons within subpopulations are accurate predictors of a shared preference for a particular direction of motion (Figure 10(b)). Conversely, a negative “between” SCC predicts the presence of an unshared motion direction preference between units belonging to distinct subpopulations (Figure 10(b)). These results were qualitatively captured by our expanded microcircuit of six units (Figures 10(c) and 10(d)). In contrast, the microcircuit of two units displays preference only for a single direction (Figure 9(b)) and therefore fails to predict the presence of an unshared motion direction preference (Figure 10(e)). Taken together, the expanded architecture has a greater predictive power over the two-unit microcircuit, by exhibiting fluctuations in population activity that marks the presence of both shared and unshared motion direction preferences.

#### 4. Discussion

Our simple and reproducible robotic implementation highlights the relation between short-term dynamics of synaptic transmission and motion discrimination. In our work, real-world stimuli are used and directly incorporated in a microcircuit dominated by a ubiquitous plasticity rule inspired from biological networks. As the microcircuit receives inputs, spiking units exhibit both preferential and nonpreferential responses to stimuli moving bidirectionally along a single axis of motion. Results from the simulation and the robotic implementation are in close agreement to analyses of visually evoked activity in V1, whereby cortical neurons exhibit



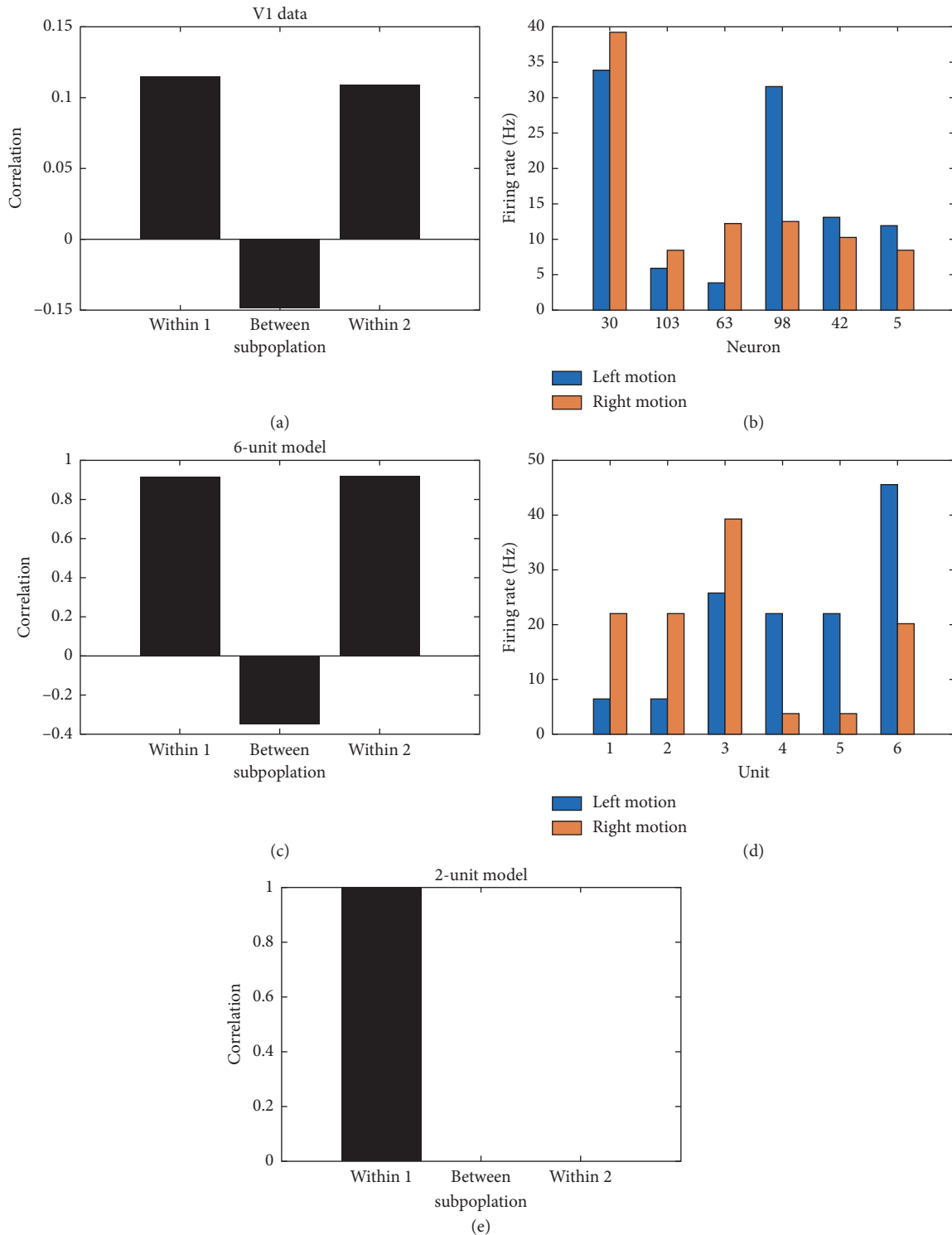


FIGURE 10: Spike count correlations predict shared and unshared motion direction preferences. (a) Mean SCC between pairs of V1 cells within and between subpopulations. (b) Average firing rate of six neurons in V1 responding to drifting vertical sinusoidal gratings. Neurons 30, 103, and 63 exhibit a preferential response for stimuli moving towards the right, whereas neurons 98, 42, and 5 exhibit a preference for stimuli moving towards the left. (c) Mean SCC between pairs of units within and between subpopulations in the six-unit microcircuit. (d) Average firing rate of six units responding to a vertical orientation stimulus in motion. Units 1, 2, and 3 exhibit a preferential response for stimuli moving towards the right, whereas units 4, 5, and 6 exhibit a preference for stimuli moving towards the left. (e) Mean SCC between the pair of units within the two-unit microcircuit. Given that both units display fully synchronized spatiotemporal patterns of activity for left and right motion discrimination (see S2 in Supplementary Material for video illustration), their mean SCC is 1. Notice that the two-unit model behaves as a single subpopulation; therefore, mean SCC for “Between” and “Within 2” cannot be computed.

higher responses for stimuli moving in the preferred direction of motion and lower responses for stimuli moving in the opposite null direction. In addition to accurate motion discrimination, the firing rate of motion-selective units in the STP model is close to the firing rate of direction-selective neurons in V1. As a result, the robotic implementation and the simulated version of the model capture both qualitative and quantitative depictions of typical neuronal responses observed in V1. In addition, units that exhibited preferential responses to stimuli moving in the specified direction were more likely to be mediated by synaptic connections exhibiting a high release probability. Furthermore, the contribution of STP as a complementary mechanism for direction selectivity is validated by the robotic implementation in real-time, showing successful motion discrimination at the behavioural level. By comparing neuronal responses from the robotic implementation to those of a simulated version of the model, accurate motion discrimination is observed despite the inherent noise of real-world stimuli present in the real-time robotic implementation. In addition, motion discrimination is conserved despite hardware constraints introducing differences in the timescale required to process stimuli in real-time (1398 seconds), versus the time required to run the computer simulation using hypothetical inputs (217 seconds). Here, processing time was measured using the execution time module named “*timeit*” in the *Python* programming language. In addition, the term “real-time” in our study referred to the amount of time it took for the Raspberry Pi microprocessor to run the STP model during which the camera processed 200 snapshots of the stimulus moving in bidirectional motion on the computer monitor. Hence, the term “real-time” was used in order to create a distinction between the robotic implementation and the simulated version of the STP model in a laptop computer.

Although visual experience exerts an influence over the direction preference that neurons acquire, the initial topological structure is an essential determinant of direction selectivity [48, 49]. In this work, the topological structure of the six-unit microcircuit expanded the repertoire of direction preferences over the two-unit microcircuit, allowing two subpopulations of units to exhibit preferential responses to opposing directions of motion. In contrast, this functional contribution happened to be absent in both the current and previously proposed [34] architecture of two units. In addition, although units in the two-unit microcircuit exhibited motion-induced progressive changes in their spatiotemporal patterns of activity, those spatiotemporal patterns were synchronized across both units during opposite directions of motion [34]. This functional property is in stark contrast to cortical networks, where asynchronous activity is more commonly observed across cells [50]. With the addition of more units, our larger network embodied a topological structure which inevitably added asynchronous spatiotemporal patterns of neural activity during motion discrimination. Finally, within the context of a larger network size, we show that global fluctuations in population activity can provide an accurate

prediction of shared versus unshared motion direction preferences. More specifically, units within subpopulations displayed a positive SCC and were therefore more likely to exhibit fluctuations in subpopulation activity that were accurate predictors of a shared motion direction preference. In contrast, units between subpopulations shared a negative SCC, suggesting that units between subpopulations were likely to display preference for opposing directions of motion. This later prediction was absent in the two-unit microcircuit because the architecture behaved as a single microcircuit thus preventing neurons from displaying the presence of an unshared motion direction preference.

A predominant view from recent computational work suggests that direction biases present at eye opening may arise purely from “innate” network connectivity [6]. The onset of this architecture is suggested to be present in the absence of any explicit coding for direction selectivity and prior to any self-organizing process facilitated by spontaneous activity or motion-induced training [6]. Similarly, the topological structure of our expanded network was constructed in the absence of any explicit coding for direction selectivity. Hence, our work is in-line with recent experimental and computational studies suggesting that visual experience may serve a *permissive* role to complement structural processes that are fully characterized at the onset of visual experience [6, 48, 51, 52]. Hence, the organization of the initial architecture may lay the foundation for the map of direction preference, as observed in the visual cortex [49].

Visually evoked activity is likely to be mediated by a variety of mechanisms operating at different timescales and at distinct developmental stages [53]. Therefore, given the wide range of plasticity rules [54], it is likely to expect other candidate mechanisms that are complementary to short-term changes in synaptic strength. Indeed, there is experimental evidence within the literature largely supporting the interaction between STP and long-term synaptic plasticity [55–59]. Amongst long-term changes in synaptic strength, spike timing-dependent plasticity (STDP) has been proposed as a ubiquitous mechanism that strengthens or weakens synapses based on the relative timing of action potentials. Despite operating at different timescales, multiple experimental studies have shown that STP and STDP interact [11, 59–64]. As a potential application of real-time learning of visually evoked activity, a future extension of our work aims to combine STP with STDP. An examination of the synergistic interaction between STP and STDP would allow us to highlight the functional role of this interaction during visual information processing. This issue is of particular importance because it remains an open question as to how short-term changes in synaptic plasticity work their way in reorganizing a local neuronal circuit with STDP [54]. Given the importance of applying real-time learning in robotic systems, we intend to implement the extended model in a physical robot as a method for validating the functional role of the interaction between STP and STDP. This approach will allow us to examine the synergy between these two ubiquitous mechanisms, as learning unfolds in the

developing circuit designed to perform motion discrimination of real-world stimuli from the sensory environment.

## 5. Conclusion

It is important to note that the work presented here does not provide a complete biophysical interpretation of the underlying neural computations observed in the brain. There are a variety of computational models in the literature that reside at different levels of description, with various levels of biological detail. Amongst these models, there are trade-offs of cognitive fidelity against biological fidelity [65]. The model proposed here presents itself as a model that exhibits motion discrimination, with a complementary mechanism that captures neuronal components designed in aiding the description of neuronal dynamics that transfer at the behavioural level. Hence, the phenomenological model is not designed to capture only cognitive function, nor is it designed to capture only neuronal components and dynamics. For example, synaptic transmission is a stochastic process whereby neurotransmitter release is unreliable. Hence, from a biophysical standpoint, an incoming action potential does not guarantee the triggering of neurotransmitter release. In contrast, the STP model proposed here captures the phenomenology of vesicular release. In doing so, the model assumes that the stochastic recovery of the vesicle is eliminated by either pooling the response from many independent synaptic connections or by taking a trial-averaged response of the stochastic recovery of the vesicle from a single synaptic connection. Hence, the model does not catch the full complexity of the nature of synaptic release. Despite the assumption of a deterministic model over a stochastic one, the phenomenological model has been formulated with strong support from electrophysiological data, capturing response traces accurately fitted by the *averaged* model [1]. Consequently, the phenomenological model of STP is detailed enough to support analyses of experimental data and general enough to transfer its applicability in a neurobotic domain; capturing some aspects of cognition at the behavioural level, while staying grounded to fundamental biological processes. The proposed model therefore resides at a level of description that falls between the two ends of the spectrum, with a characterization of information processing that is useful when describing the performance of some task with some level of phenomenological abstraction. Consequently, the model proposed here turns the trade-off between full complexity and full cognitive function into a synergy between the two ends of the spectrum. At the theoretical level, the current approach in modelling neurobiological components intends to study neuronal dynamics and their contribution to cognition and behaviour. Hence, the phenomenological model is designed to be interpreted in the context of the cognitive functions it supports. Currently, cognitive models steer away from neurobiological fidelity, yet successfully implement task-performing cognitive models of the brain. These models take sensory inputs and exhibit motor outputs that perform experimental tasks that are well in-line with human-level performance. Conversely, biophysical models capture

biologically plausible dynamical components of the brain with a high degree of fidelity but fail to exhibit cognitive task performance [65]. Hence, the neurobiological basis of the work presented here is intended to tie computational neuroscience to tasks of cognitive science, while being mindful of the compromise between biological plausibility and computational feasibility. As behaviour is deeply coupled not only in the underlying neuronal dynamics, but also by the anatomical constraints of the physical body it controls, the overall aim of this study was to provide a step forward in applying well-established models from neuroscience into the domain of neurorobotics. In doing so, it highlights the contribution of STP predominantly in the context of a motion discrimination task applied in a neurobotic domain and uses an embodied robot as a method for qualitatively and quantitatively capturing the response characteristics of direction-selective cells in V1.

## Data Availability

The experimental data used to support the findings of this study were supplied by Adam Kohn under license and so cannot be made freely available. Requests for access to these data should be made to Jeff Teeters, [jteeters@berkeley.edu](mailto:jteeters@berkeley.edu).

## Conflicts of Interest

The authors declare that there are no conflicts of interest regarding the publication of this paper.

## Acknowledgments

We are thankful to André Cyr and Matias Calderini for useful comments and Adam Kohn for allowing access to the experimental dataset. This research was supported by the Natural Sciences and Engineering Research Council of Canada (NSERC) (210663) and the Ontario Graduate Scholarship (OGS) award program.

## Supplementary Materials

S1. A video clip of the real-time robotic simulation setup and the corresponding spatiotemporal patterns of activity of all six units. S2. A video clip of the spatiotemporal patterns of activity of the two-unit model. (*Supplementary Materials*)

## References

- [1] M. V. Tsodyks and H. Markram, "The neural code between neocortical pyramidal neurons depends on neurotransmitter release probability," *Proceedings of the National Academy of Sciences*, vol. 94, no. 2, pp. 719–723, 1997.
- [2] J. L. Krichmar, J. Conradt, and M. Asada, "Neurobiologically inspired robotics: enhanced autonomy through neuro-morphic cognition," *Neural Networks*, vol. 72, pp. 1–2, 2015.
- [3] D. Hassabis, D. Kumaran, C. Summerfield, and M. Botvinick, "Neuroscience-inspired artificial intelligence," *Neuron*, vol. 95, no. 2, pp. 245–258, 2017.
- [4] M.-J. Escobar, G. S. Masson, T. Vieville, and P. Kornprobst, "Action recognition using a bio-inspired feedforward spiking

- network,” *International Journal of Computer Vision*, vol. 82, no. 3, pp. 284–301, 2009.
- [5] Q. Wu, T. M. Mcginnity, L. Maguire, and J. Cai, “Motion detection using spiking neural network model,” in *Proceedings of the International Conference on Intelligent Computing*, pp. 76–83, Shanghai, China, September 2008.
- [6] S. V. Adams and C. M. Harris, “A computational model of innate directional selectivity refined by visual experience,” *Scientific Reports*, vol. 5, no. 1, article 12553, 2015.
- [7] R. S. Zucker and W. G. Regehr, “Short-term synaptic plasticity,” *Annual Review of Physiology*, vol. 64, no. 1, pp. 355–405, 2002.
- [8] L. F. Abbott and W. G. Regehr, “Synaptic computation,” *Nature*, vol. 431, no. 7010, pp. 796–803, 2004.
- [9] J. S. Dittman, A. C. Kreitzer, and W. G. Regehr, “Interplay between facilitation, depression, and residual calcium at three presynaptic terminals,” *Journal of Neuroscience*, vol. 20, no. 4, pp. 1374–1385, 2000.
- [10] T. P. Carvalho, “A novel learning rule for long-term plasticity of short-term synaptic plasticity enhances temporal processing,” *Frontiers in Integrative Neuroscience*, vol. 5, pp. 1–11, 2011.
- [11] H. Markram and M. Tsodyks, “Redistribution of synaptic efficacy between neocortical pyramidal neurons,” *Nature*, vol. 382, no. 6594, pp. 807–810, 1996.
- [12] L. F. Abbott, J. A. Varela, K. Sen, and S. B. Nelson, “Synaptic depression and cortical gain control,” *Science*, vol. 275, no. 5297, pp. 220–224, 1997.
- [13] M. S. Goldman, P. Maldonado, and L. F. Abbott, “Redundancy reduction and sustained firing with stochastic depressing synapses,” *Journal of Neuroscience*, vol. 22, no. 2, pp. 584–591, 2002.
- [14] M. C. W. Van Rossum, M. A. A. Van Der Meer, D. Xiao, and M. W. Oram, “Adaptive integration in the visual cortex by depressing recurrent cortical circuits,” *Neural Computation*, vol. 20, no. 7, pp. 1847–1872, 2008.
- [15] R. P. Costa, R. C. Froemke, P. J. Sjöström, and M. C. W. van Rossum, “Unified pre- and postsynaptic long-term plasticity enables reliable and flexible learning,” *Elife*, vol. 4, pp. 1–16, 2015.
- [16] P.-Y. Deng and V. A. Klyachko, “The diverse functions of short-term plasticity components in synaptic computations,” *Communicative & Integrative Biology*, vol. 4, no. 5, pp. 543–548, 2011.
- [17] Z. Rotman, P.-Y. Deng, and V. A. Klyachko, “Short-term plasticity optimizes synaptic information transmission,” *Journal of Neuroscience*, vol. 31, no. 41, pp. 14800–14809, 2011.
- [18] A. Klug, J. G. G. Borst, B. A. Carlson, C. Kopp-Scheinflug, V. A. Klyachko, and M. A. Xu-Friedman, “How do short-term changes at synapses fine-tune information processing?,” *Journal of Neuroscience*, vol. 32, no. 41, pp. 14058–14063, 2012.
- [19] W. X. Chen and D. V. Buonomano, “Developmental shift of short-term synaptic plasticity in cortical organotypic slices,” *Neuroscience*, vol. 213, pp. 38–46, 2012.
- [20] R. S. Larsen, I. T. Smith, J. Miriyala et al., “Synapse-specific control of experience-dependent plasticity by presynaptic NMDA receptors,” *Neuron*, vol. 83, no. 4, pp. 879–893, 2014.
- [21] J. Urban-Ciecko, J. A. Wen, P. K. Parekh, and A. L. Barth, “Experience-dependent regulation of presynaptic NMDARs enhances neurotransmitter release at neocortical synapses,” *Learning & Memory*, vol. 22, no. 1, pp. 47–55, 2015.
- [22] K. J. Bender, “Synaptic basis for whisker deprivation-induced synaptic depression in rat somatosensory cortex,” *Journal of Neuroscience*, vol. 26, no. 16, pp. 4155–4165, 2006.
- [23] C. E. J. Cheetham and K. Fox, “The role of sensory experience in presynaptic development is cortical area specific,” *Journal of Physiology*, vol. 589, no. 23, pp. 5691–5699, 2011.
- [24] G. T. Finnerty, L. S. E. Roberts, and B. W. Connors, “Sensory experience modifies the short-term dynamics of neocortical synapses,” *Nature*, vol. 400, no. 6742, pp. 367–371, 1999.
- [25] A. E. Takesian, V. C. Kotak, and D. H. Sanes, “Presynaptic GABAB receptors regulate experience-dependent development of inhibitory short-term plasticity,” *Journal of Neuroscience*, vol. 30, no. 7, pp. 2716–2727, 2010.
- [26] T. Abrahamsson, C. Y. C. Chou, S. Y. Li et al., “Differential regulation of evoked and spontaneous release by presynaptic NMDA receptors,” *Neuron*, vol. 96, no. 4, pp. 839.e5–855.e5, 2017.
- [27] R. S. Larsen and P. J. Sjöström, “Synapse-type-specific plasticity in local circuits,” *Current Opinion in Neurobiology*, vol. 35, pp. 127–135, 2015.
- [28] A. Banerjee, R. S. Larsen, B. D. Philpot, and O. Paulsen, “Roles of presynaptic NMDA receptors in neurotransmission and plasticity,” *Trends in Neurosciences*, vol. 39, no. 1, pp. 26–39, 2016.
- [29] P. Paoletti, C. Bellone, and Q. Zhou, “NMDA receptor subunit diversity: impact on receptor properties, synaptic plasticity and disease,” *Nature Reviews Neuroscience*, vol. 14, no. 6, pp. 383–400, 2013.
- [30] S. Carver, E. Roth, N. J. Cowan, and E. S. Fortune, “Synaptic plasticity can produce and enhance direction selectivity,” *PLoS Computational Biology*, vol. 4, no. 2, article e32, 2008.
- [31] F. S. Chance, S. B. Nelson, and L. F. Abbott, “Synaptic depression and the temporal response characteristics of V1 cells,” *Journal of Neuroscience*, vol. 18, no. 12, pp. 4785–4799, 1998.
- [32] D. Hansel and G. Mato, “Short-term plasticity explains irregular persistent activity in working memory tasks,” *Journal of Neuroscience*, vol. 33, no. 1, pp. 133–149, 2013.
- [33] N. J. Buchs and W. Senn, “Spike-based synaptic plasticity and the emergence of direction selective simple cells: simulation results,” *Journal of Computational Neuroscience*, vol. 13, no. 3, pp. 167–186, 2002.
- [34] N. Berberian, M. Ross, S. Chartier, and J.-P. Thivierge, “Synergy between short-term and long-term plasticity explains direction-selectivity in visual cortex,” in *Proceedings of the IEEE Symposium Series on Computational Intelligence*, pp. 1–8, Honolulu, HI, USA, November–December 2017.
- [35] H. Ko, L. Cossell, C. Baragli et al., “The emergence of functional microcircuits in visual cortex,” *Nature*, vol. 496, no. 7443, pp. 96–100, 2013.
- [36] E. Vasilaki and M. Giugliano, “Emergence of connectivity motifs in networks of model neurons with short- and long-term plastic synapses,” *PLoS One*, vol. 9, no. 1, Article ID e84626, 2014.
- [37] L. Cossell, M. F. Iacaruso, D. R. Muir et al., “Functional organization of excitatory synaptic strength in primary visual cortex,” *Nature*, vol. 518, no. 7539, pp. 399–403, 2015.
- [38] M. A. Smith and A. Kohn, “Spatial and temporal scales of neuronal correlation in primary visual cortex,” *Journal of Neuroscience*, vol. 28, no. 48, pp. 12591–12603, 2008.
- [39] R. C. Kelly, M. A. Smith, R. E. Kass, and T. S. Lee, “Local field potentials indicate network state and account for neuronal response variability,” *Journal of Computational Neuroscience*, vol. 29, no. 3, pp. 567–579, 2010.
- [40] J. R. Cavanaugh, “Nature and interaction of signals from the receptive field center and surround in macaque V1 neurons,” *Journal of Neurophysiology*, vol. 88, no. 5, pp. 2530–2546, 2002.

- [41] G. Mongillo, O. Barak, and M. Tsodyks, "Synaptic theory of working memory," *Science*, vol. 319, no. 5869, pp. 1543–1546, 2008.
- [42] A. Kohn and M. A. Smith, "Utah array extracellular recordings of spontaneous and visually evoked activity from anesthetized Macaque primary visual cortex (V1)," in *Proceedings of the Collaborative Research in Computational Neuroscience (CRCNS 2016)*, Albert Einstein College of Medicine, New York, NY, USA, 2016.
- [43] A. A. Faisal, L. P. J. Selen, and D. M. Wolpert, "Noise in the nervous system," *Nature Reviews Neuroscience*, vol. 9, no. 4, pp. 292–303, 2008.
- [44] M. M. Churchland, B. M. Yu, J. P. Cunningham et al., "Stimulus onset quenches neural variability: a widespread cortical phenomenon," *Nature Neuroscience*, vol. 13, pp. 369–378, 2010.
- [45] J. A. Varela, K. Sen, J. Gibson, J. Fost, L. F. Abbott, and S. B. Nelson, "A quantitative description of short-term plasticity at excitatory synapses in layer 2/3 of rat primary visual cortex," *Journal of Neuroscience*, vol. 17, no. 20, pp. 7926–7940, 1997.
- [46] T. A. Engel, N. A. Steinmetz, M. A. Gieselmann, A. Thiele, T. Moore, and K. Boahen, "Selective modulation of cortical state during spatial attention," *Science*, vol. 352, no. 6316, pp. 1140–1144, 2016.
- [47] G. Vinci, V. Ventura, M. A. Smith, and R. E. Kass, "Separating spike count correlation from firing rate correlation," *Neural Computation*, vol. 28, no. 5, pp. 849–881, 2016.
- [48] A. Roy, I. K. Christie, G. M. Escobar et al., "Does experience provide a permissive or instructive influence on the development of direction selectivity in visual cortex?," *Neural Development*, vol. 13, no. 1, pp. 1–11, 2018.
- [49] S. D. Van Hooser, Y. Li, M. Christensson, G. B. Smith, L. E. White, and D. Fitzpatrick, "Initial neighborhood biases and the quality of motion stimulation jointly influence the rapid emergence of direction preference in visual cortex," *Journal of Neuroscience*, vol. 32, no. 21, pp. 7258–7266, 2012.
- [50] A. S. Ecker, P. Berens, A. S. Tolias, and M. Bethge, "The effect of noise correlations in populations of diversely tuned neurons," *Journal of Neuroscience*, vol. 31, no. 40, pp. 14272–14283, 2011.
- [51] Y. Li, S. D. Van Hooser, M. Mazurek, L. E. White, and D. Fitzpatrick, "Experience with moving visual stimuli drives the early development of cortical direction selectivity," *Nature*, vol. 456, no. 7224, pp. 952–956, 2008.
- [52] A. Cyr, F. Thériault, M. Ross, N. Berberian, and S. Chartier, "Spiking neurons integrating visual stimuli orientation and direction selectivity in a robotic context," *Frontiers in Neurobotics*, vol. 12, pp. 1–10, 2018.
- [53] J. M. Clemens, N. J. Ritter, A. Roy, J. M. Miller, and S. D. Van Hooser, "The laminar development of direction selectivity in ferret visual cortex," *Journal of Neuroscience*, vol. 32, no. 50, pp. 18177–18185, 2012.
- [54] H. Markram, W. Gerstner, and P. J. Sjöström, "A history of spike-timing-dependent plasticity," *Frontiers in Synaptic Neuroscience*, vol. 3, pp. 1–24, 2011.
- [55] H. Markram, J. Lübke, M. Frotscher, and B. Sakmann, "Regulation of synaptic efficacy by coincidence of postsynaptic APs and EPSPs," *Science*, vol. 275, no. 5297, pp. 213–215, 1997.
- [56] H. R. Monday and P. E. Castillo, "Closing the gap: long-term presynaptic plasticity in brain function and disease," *Current Opinion in Neurobiology*, vol. 45, pp. 106–112, 2017.
- [57] A. Loebel, J.-V. Le Be, M. J. E. Richardson, H. Markram, and A. V. M. Herz, "Matched pre- and post-synaptic changes underlie synaptic plasticity over long time scales," *Journal of Neuroscience*, vol. 33, no. 15, pp. 6257–6266, 2013.
- [58] H. R. Monday, T. J. Younts, and P. E. Castillo, "Long-term plasticity of neurotransmitter release: emerging mechanisms and contributions to brain function and disease," *Annual Review of Neuroscience*, vol. 41, no. 1, pp. 299–322, 2018.
- [59] P. J. Sjöström, G. G. Turrigiano, and S. B. Nelson, "Multiple forms of long-term plasticity at unitary neocortical layer 5 synapses," *Neuropharmacology*, vol. 52, no. 1, pp. 176–184, 2007.
- [60] V. Bolshakov and S. Siegelbaum, "Regulation of hippocampal transmitter release during development and long-term potentiation," *Science*, vol. 269, no. 5231, pp. 1730–1734, 1995.
- [61] P. J. Sjöström, G. G. Turrigiano, and S. B. Nelson, "Neocortical LTD via coincident activation of presynaptic NMDA and cannabinoid receptors," *Neuron*, vol. 39, no. 4, pp. 641–654, 2003.
- [62] H. Tokuoka and Y. Goda, "Activity-dependent coordination of presynaptic release probability and postsynaptic GluR2 abundance at single synapses," *Proceedings of the National Academy of Sciences of the United States of America*, vol. 105, no. 38, pp. 14656–14661, 2008.
- [63] I. Jin, S. Puthanveetil, H. Udo, K. Karl, E. R. Kandel, and R. D. Hawkins, "Spontaneous transmitter release is critical for the induction of long-term and intermediate-term facilitation in Aplysia," *Proceedings of the National Academy of Sciences*, vol. 109, no. 23, pp. 9131–9136, 2012.
- [64] M. Kintscher, C. Wozny, F. W. Jenkinson, D. Schmitz, and J. Breustedt, "Role of RIM1a in short- and long-term synaptic plasticity at cerebellar parallel fibres," *Nature Communications*, vol. 4, no. 1, article 2392, 2013.
- [65] N. Kriegeskorte and P. K. Douglas, "Cognitive computational neuroscience," *Nature Neuroscience*, vol. 21, pp. 1148–1160, 2018.

## Research Article

# Spatial Concept Learning: A Spiking Neural Network Implementation in Virtual and Physical Robots

André Cyr <sup>1</sup> and Frédéric Thériault <sup>2</sup>

<sup>1</sup>*School of Psychology, University of Ottawa, Ottawa, Ontario, Canada*

<sup>2</sup>*Department of Computer Science, Cégep du Vieux Montréal, Montréal, Quebec, Canada*

Correspondence should be addressed to André Cyr; [andre.cyr1@videotron.ca](mailto:andre.cyr1@videotron.ca)

Received 21 September 2018; Accepted 11 March 2019; Published 1 April 2019

Academic Editor: Reinoud Maex

Copyright © 2019 André Cyr and Frédéric Thériault. This is an open access article distributed under the Creative Commons Attribution License, which permits unrestricted use, distribution, and reproduction in any medium, provided the original work is properly cited.

This paper proposes an artificial spiking neural network (SNN) sustaining the cognitive abstract process of spatial concept learning, embedded in virtual and real robots. Based on an operant conditioning procedure, the robots learn the relationship of horizontal/vertical and left/right visual stimuli, regardless of their specific pattern composition or their location on the images. Tests with novel patterns and locations were successfully completed after the acquisition learning phase. Results show that the SNN can adapt its behavior in real time when the rewarding rule changes.

## 1. Introduction

Mastering abstract concepts seems like a key to reach a higher level of cognition, allowing animals to gather more complex knowledge [1]. Concepts save time by avoiding learning every stimuli, regrouping them in general categories to deal with new situations. According to Zentall et al. [2], three main hierarchical types of abstract concepts are defined. Perceptual or natural abstract concepts consist in finding physical similarities between different objects or stimuli and are a first type of categorization. A second type, relational concepts, concerns the general rule or abstract relationship between stimuli that is not directly related to their specific physical attributes. In that sense, it is a second-order process [3, 4]. For example, sizes (such as small and large) are abstract categories that are determined by comparing the sizes of the presented objects. Thus, the dimensional relationship is not tied to the exact physical size of the objects but compared and developed from experience. Finally, associative or functional concepts imply that one stimulus or characteristic is interchangeable with another one (i.e., Dogs-Barking). This paper focuses on spatial abstract concepts as a prior step toward achieving a relational above/below neural circuit.

There is an abundant collection of empirical data on relational concepts, as well as in the literature. Animal models and methodologies are also numerous with many levels of comparison [5–9]. Recently, this higher cognitive process was explored with invertebrates. Astonishingly, it was shown that bees could learn several different types of relational concepts, despite having a small brain that consists of less than one million neurons [10–15]. Even if some progress is made to relate the learning process and the neural substrates [16], no precise neural circuit is currently known to explain concept learning from a complete sensory to motor architecture, be it natural or artificial. Also, the relationship between perceptual and relational concept levels remains mostly unexplored from a computational neuro-robotic perspective.

Neural modeling is one computational tool that that maybe helpful for approaching this problem, more precisely by elaborating a precise artificial neural circuit that correlates the behavioral observations. Few articles have explored the abstract concept learning process phenomenon from this angle. Therefore, this article seeks to further study the topic under a spiking neural network (SNN) paradigm. Moreover, this research also goes a step beyond an SNN by implementing the whole cognitive process in a

complete virtual and physical neurobotic model [17]. This allows validation of the proposed computational model in a brain-body-environment or embodied cognitive context [18].

SNNs are bioinspired neural models that have emphasis on single spike events and their temporal-coincidental relations [19, 20]. Generally, the learning rule used from these neural models is based on synaptic changes from a spike-timing dependent plasticity (STDP) process [21–23]. As such, this paper uses a specific SNN model to sustain the representation of a spatial concept learning process.

In this study, a spatial visual task with different images composed of horizontal/vertical and left/right patterns are shown in front of a static robot. From an operant conditioning procedure, the robot has to decide which side to choose (left or right). Hence, from reinforcements, it learns to associate different spatial relations, independently of specific stimulus patterns shown and their locations. This visual learning scenario is partially inspired from the one made with bees [11, 24], which fully succeeded in learning two relational abstract concepts (above/below, left/right, and same/different) with generalization transfer tests. This paper is in the continuity of our previous work, which was to build an SNN that sustains the identity concept learning process in the neurobotic domain [25].

The next section describes the methodology and the details on the learning protocol. It is followed by results, highlighting the spatial concept learning process from the synaptic to the behavioral changes. The last section contains a discussion on the current model’s limitations and the future perspectives of this learning model.

## 2. Methodology

*2.1. Protocol.* The visual task consists in learning horizontal/vertical and left/right spatial concepts. Images are projected in front of a robot. Each of them has two sides (left and right): one side contains two black/white motifs aligned vertically and the other side contains two motifs aligned horizontally (Figure 1). The first experiment consists of grouping patterns (horizontal or vertical), which are permuted on three possible positions on each side. Thus, all images are first randomized for the side of the horizontal and vertical patterns, second for the position, and third for the individual stimulus patterns composing them (Figure 2). Images cover the whole field of view of the robot’s camera. The second experiment tests stimuli on novel locations, once the learning phase is completed. Finally, a third experiment allows to validate the SNN under less precise conditions, by using a real robot.

Following an image capture, the robot takes a dichotomous left or right decision according to a chosen stimulus, randomly selected prior to learning. This action is manifested by directly rotating its motor towards it. From a conditioning procedure, a reward is consistently applied on the vertical or the horizontal motif, depending on the desired learning rule. Along with the task and with few positive reinforcers, the robot learns the horizontal/vertical

or left/right relation, ignoring the exact individual pattern features as well as its location on its side. To validate the robustness of the SNN, the experiment ends with the presentation of novel patterns at new locations.

*2.2. Architecture.* The neural circuit is organized into four basic layers: a sensory input layer, an integrative layer, a decision layer, and a motor output layer (Figure 3). The sensory visual neurons are linked to a camera that captures images of 4:3 ratio. These neurons are arranged in a  $3 \times 15$  array, with each of them overlapping a different spatial section, hence completely covering the visual field. In this experiment, sensory neurons only integrate black intensity with numerical values. These are averaged and normalized in a percentage scale. Therefore, the spiking activities of sensory visual neurons reflect the stimulus patterns shown in front of the robot. Once an image of the robot’s view is captured, a cooldown prevents the camera from triggering before an action is made. Otherwise, constant stimulus inputs from this layer would prevent the SNN from integrating and acting on a single image.

The sensory input layer forwards signals to integrative neurons. These are topographically organized in a neighborhood configuration, separated in left/right and upper/mid/lower logical sections. In the current model, the first level of integration is composed of 12 neurons (six for vertical and six for horizontal detection). This allows the SNN to react to local stimuli. More precisely, each integrative element can respond to any vertical or horizontally displayed black stimulus. A second integrative level regroups all horizontal and vertical neurons for each side (ViewVerticalLeft, ViewVerticalRight, ViewHorizontalLeft, and ViewHorizontalRight).

From the integrative neurons, signals are propagated to the decision layer, more precisely to the Predictor neurons. Those Predictor neurons are linked to their associated Choose neuron (ChooseLeft, ChooseRight, ChooseVert, and ChooseHor) with a weak excitatory synapse and a synaptic learning rule (STDP) and are also connected to the action layer. Prior to learning, Predictor neurons cannot trigger Choose neurons alone. As rewards are given, the STDP rule strengthens those specific synapses. This eventually allows the correct Predictor to trigger its associated Choose neuron. Rewards are simulated by moving a block in front of an infrared sensor located at the back of the robot. In this study, the learning rule from STDP needs a third factor (the reward) to be activated [26, 27]. When no reward is given, it implies that the robot took a wrong decision and the synapse strongly weakens.

The decision layer also contains Go neurons (GoVertLeft, GoVertRight, GoHorLeft, GoHorRight). For example, when the horizontal Choose neuron spikes, the Go horizontal neuron allows the proper action (turn left/right) to be done, depending on where the horizontal stimulus is located.

The action layer consists of two motor neurons (ActionTurnLeft, ActionTurnRight), orienting the robot towards the chosen side. Prior to learning, when a pattern is detected

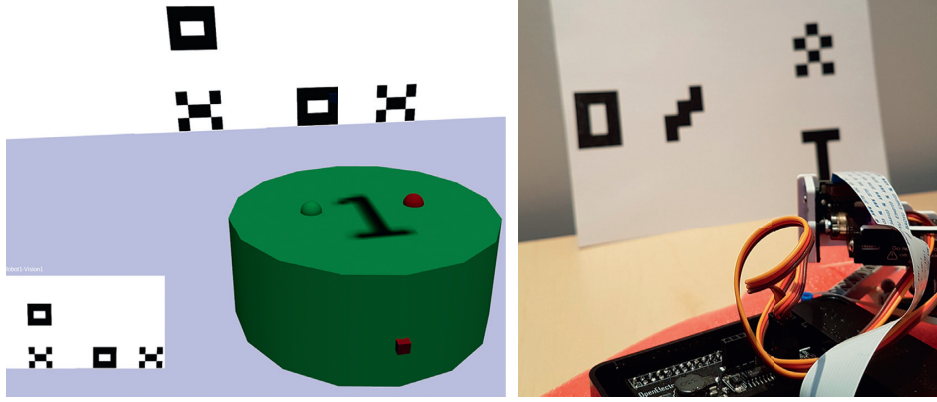


FIGURE 1: Similar virtual and physical environments, showing the robots and their view. On the left side, the virtual environment displays the robot's view on the bottom left part. In this case, it consists of a left vertical and a right horizontal image, composed of two different patterns (O and X).

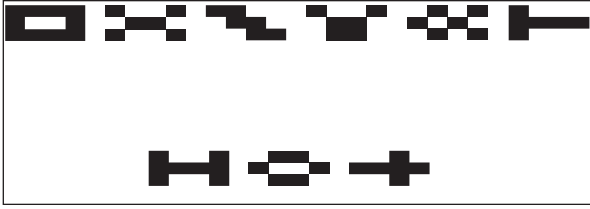


FIGURE 2: All patterns used in this study. The top six patterns are shown in the first part of the experiment. The three lower patterns represent the novel patterns used at the end of the simulation.

in the sensory visual layer, a randomized action is triggered by sending a delayed signal to motor neurons. This action could eventually be bypassed from the Predictor neurons in the decision neural, after learning.

**2.3. Neural Dynamic.** The spiking neural model used in this paper and the neural architecture were achieved with the SIMCOG software [28]. The neural dynamic is based on standard properties, which are membrane potential variation (equations (1), (3), and (4)), nonlinear integration of excitatory/inhibitory inputs (equation (2)), threshold for spike events, absolute refractory period, and an after spike hyperpolarization state. Since the neural circuit is well defined, the tuning of the starting synaptic weights was manually adjusted prior to launching the final experiment (supplementary materials for starting synaptic weight values at <http://aifuture.com/res/2018-spatial>). The learning rule used in the proposed model integrates a STDP function (equation (5)) only available for synapses in the decision layer.

Leaky integrator neural dynamic:

$$v_m(k) = f(v_m(k-1) + \sum v_i), \quad (1)$$

where  $v_m(k)$  = membrane potential at cycle  $k$ ,  $v_i$  = synaptic input as calculated in equation (2), and  $f$  = membrane potential curve as calculated in equation (3).

General function describing the postsynaptic potential curve:

$$v_i(t) = \begin{cases} ae^{-t/\tau}, & \text{if } t \leq t \text{ Max}, \\ 0, & \text{if } t > t \text{ Max}, \end{cases} \quad (2)$$

where  $a$  = maximum amplitude (set from 2 to 20),  $\tau$  = tau (set to 7),  $t$  = time since spike (cycle), and  $t \text{ Max}$  = maximum duration of a PSP (set from 1 to 10 cycles).

Membrane potential function:

$$f(v_m) = \begin{cases} g(v_m, 0), & \text{if } v_m < v_m \text{ Rest}, \\ v_m \text{ Rest}, & \text{else if } v_m = v_m \text{ Rest}, \\ g(v_m, 1), & \text{else if } v_m < v_m \text{ Threshold}, \\ 100, & \text{else,} \end{cases} \quad (3)$$

where  $v_m \text{ Rest}$  = membrane potential rest value (set as 43) and  $v_m \text{ Threshold}$  = threshold value (set as 65).

Membrane potential output:

$$g(v_m, d) = \begin{cases} \min(\text{each } v \text{ in vec where } v > v_m), & \text{if } d = 0, \\ \max(\text{each } v \text{ in vec where } v < v_m), & \text{if } d = 1, \end{cases} \quad (4)$$

where  $\text{vec} = [4, 11, 18, 23, 28, 32, 36, 42, 43, 44, 45, 47, 50, 53, 58, 65, 100]$ , ascending phase to reach threshold =  $\exp(0.8 + 0.3 * t) + 40$  for each  $t$  from 0 to 8, ascending phase from post action potential to rest =  $\log_{10}(0.9 + 0.2 * t) * 100$  for each  $t$  from 1 to 7, and action potential = 100.

General STDP function.

$$\Delta w = a * b * e^{-abs(t_{\text{post}} - t_{\text{pre}})/c}, \quad (5)$$

where  $\Delta w$  = synaptic weight change,  $a$  = multiplier factor (set to 1.0),  $b = 1$  when  $t_{\text{post}} > t_{\text{pre}}$ ,  $-1$  when  $t_{\text{post}} < t_{\text{pre}}$ ,  $c$  = time-constant (set to 100/3), STDP coefficients for  $\Delta w$ : duration of the synaptic change = 1000 cycles, max. synaptic change in one paired spike = 25%, and max. global synaptic change = 100%.



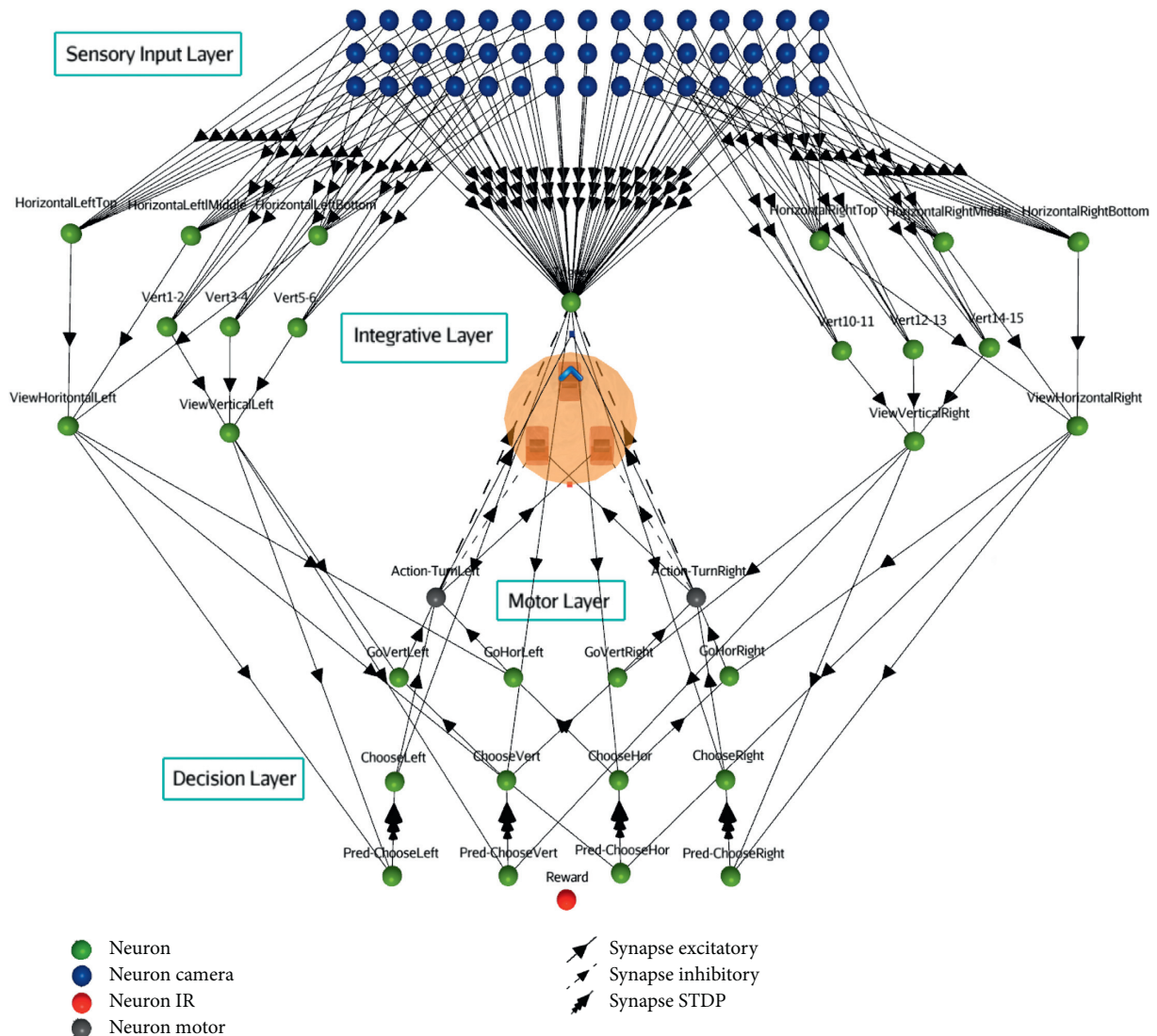


FIGURE 3: Full view of the SNN architecture, composed of the robot and four different functional neural layers.

**2.4. Physical Environment.** After tuning the SNN parameters and evaluating them in a virtual world, it was embedded in a physical environment using a Raspberry Pi 3 mounted with a  $160 \times 120$  resolution camera and two servomotors (for pan/tilt camera rotation). The objective of this simulation was to verify the SNN's capability to learn with less precise variables (i.e., timing of events, camera detection, etc.). To embed the SNN in the Raspberry Pi robot, it only required a single modification. Since the robot does not contain infrared sensors, the reward was instead given by displaying a red sheet of paper in front of it. Hence, an additional reward visual neuron was linked to the camera, in order to perceive the red color.

### 3. Results

Figure 4 represents the neural behavior dynamic of the main elements achieving the spatial concept learning task. For each trial, the sensory neural layer ( $3 \times 15$  array of neurons) captures the image with one horizontal pattern on one side

and one vertical pattern on the other side. These are composed of two different black and white motifs ( $3 \times 4$  pixels). Three examples of the robot's view are shown at the top of the figure. The sensory layer forwards the signal to the integrative layer resulting in associated spike events of the four main neurons (graphics A to D). From these, a single Choose neuron from the decision neural layer (graphics E to H) emits an action potential.

In the first experiment, the desired output was set on the vertical stimulus. Then the rewarding rule was modified, as of cycle 2000, to give a reward when choosing the horizontal pattern. One can see that the SNN fully adapted its behavior even when changing the rewarding rules online. The reverse situation (learning horizontal stimulus before the vertical one) was also tested with no effect on the learning procedure (not shown). Since the image sequence is randomized, including both the patterns and the horizontal or vertical sides, several trials were done. In all cases, the SNN succeeded in learning, adapting its behavior according to the desired output.

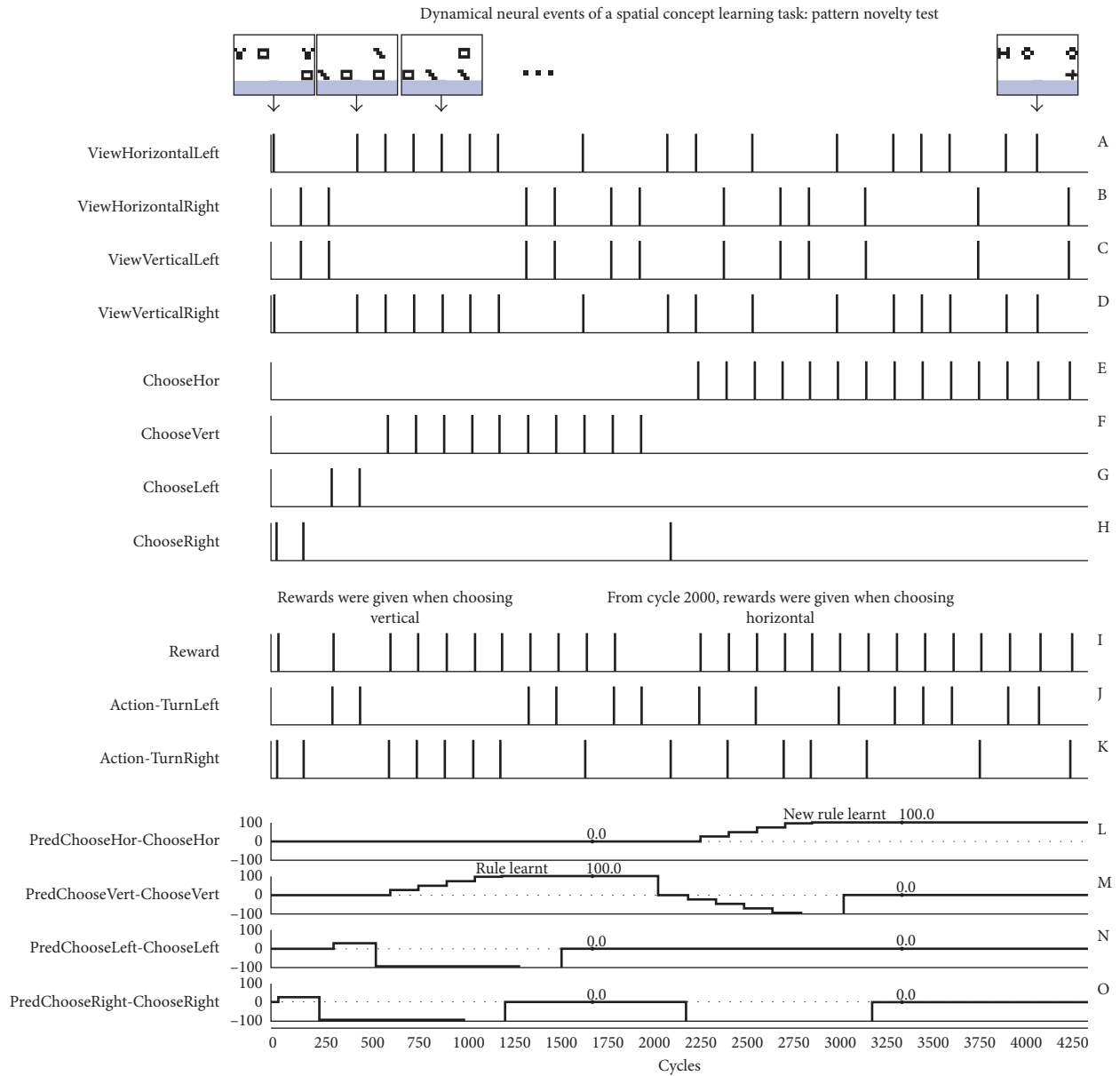


FIGURE 4: Dynamical neural representations of the virtual simulation, showing the SNN’s behavioral adaptation according to given rewards. Graphics A–K represent neural spike events and L–O consist of synaptic STDP coefficients. The final test includes novel patterns composing the stimulus. In the top row of the figure, only few images from the whole set are shown for clarity, the arrow indicating the perceived stimulus.

At the beginning of the simulation, the synaptic links between the Predictor neurons and the Choose neurons are weak. Thus, the choice of action is random. During the experiment, a positive reinforcement (Graphic I) is applied when the SNN succeeds in choosing the correct action (Graphics J and K). This learning process is shown in graphics L to O with an increase in the synaptic weights from several rewards. The learning step factor was designed to reach the threshold point after three correct associations, but it could have been done differently for smooth learning or even to trigger a learnt response after a single correct trial. When the SNN constantly predicted the correct action, a last test was done with novel patterns (see example at cycle 4100).

In the second experiment, most images were displaying verticals on the left side, up until cycle 2200 (Figure 5). This

allowed the SNN to learn between two choices: left and vertical. To prevent the robot from only learning the left side rule (from the ChooseLeft neuron), few horizontal-left/horizontal-right images were shown (for example, see at cycle 250). After cycle 2200, vertical patterns were shown on the right, verifying that the SNN could still use the learnt vertical rule even though it was on a novel location.

The real experimentation, using the Raspberry Pi, gave similar results, though it was necessary to run the experiment a few times before succeeding. The main difficulty here was with respect to the timing and manual image adjustments in front of the camera; otherwise, it was not capturing images correctly in the sensory input layer. Also, since no infrared sensors were available on the real robot, the

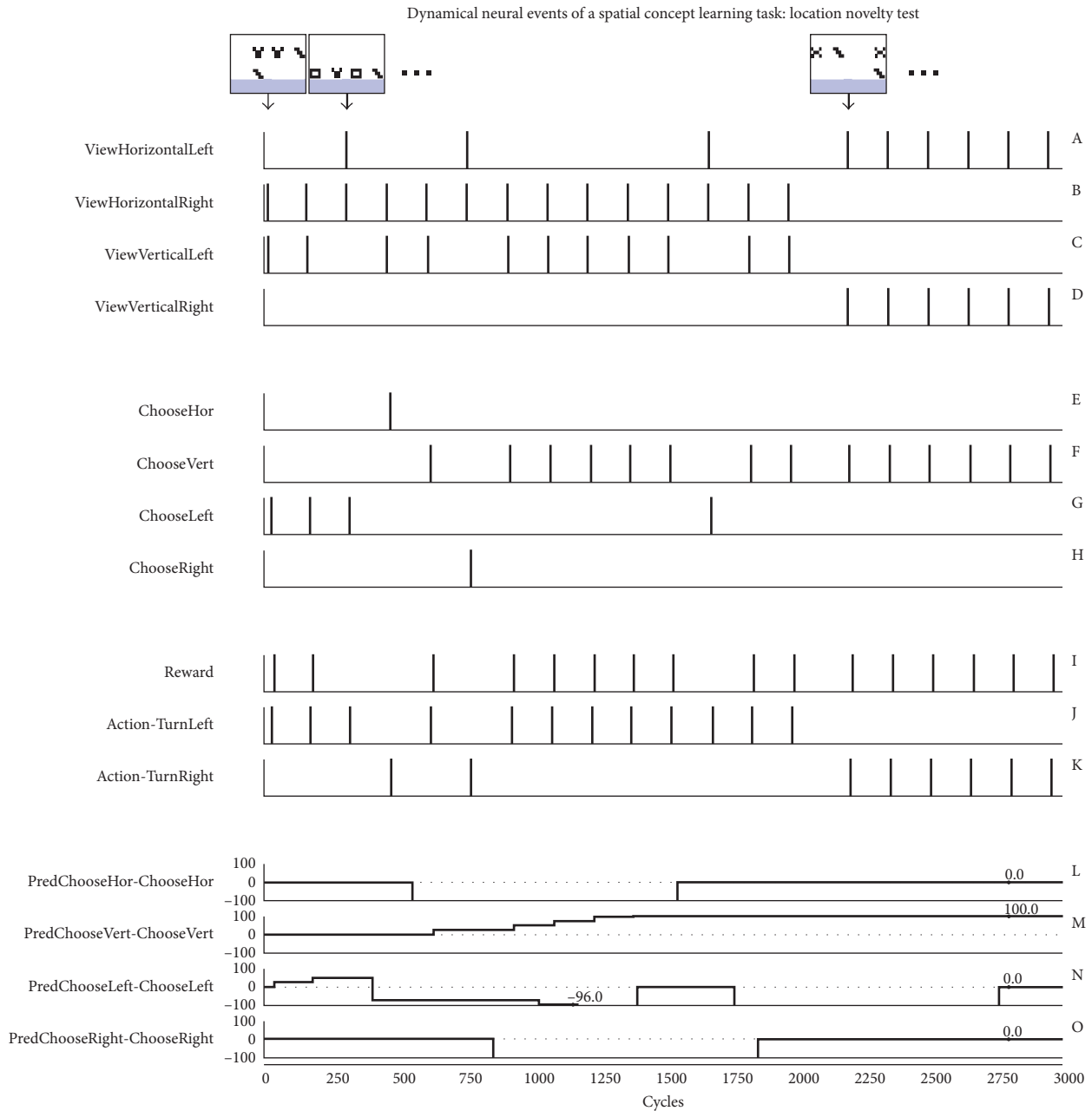


FIGURE 5: Dynamical neural representations of the virtual simulation, showing the ability of the SNN to adapt its behavior according to given rewards. Graphics A–K represent neural spike events and L–O consist of synaptic STDP coefficients. The final test includes a novel location of the stimulus. In the top row of the figure, only few images from the whole set are shown for clarity, the arrow indicating the perceived stimulus.

rewards were instead given by showing red colored papers in front of it, which were perceived by its camera. This added some artifacts during the simulation. Video and simulation results are available as supplementary materials: <http://aifuture.com/res/2018-spatial>.

#### 4. Discussion

Abstract concept learning is thought to be a higher cognitive process and a key feature of intelligent natural species. The recent literature in neuroscience suggests that that even invertebrates with small brains could reach this level of

complexity. This attractive fact stimulates the emulation of the cognitive phenomenon with a bioinspired artificial spiking neurons approach embedded in a neurobotic model. One working hypothesis of this paradigm relies on a level of computational general intelligence level, based on functional cognitive processes that are related for specific physical body structures and environments. However, the simulation of a cognitive process from a precise artificial neural circuit and a given robot implementation does not intend to reflect a natural one, but only reproduce the function and the behavior with artificial substrates, grounded in a real-world context.

This project intends to be a prior step to reach the relational concept level, from designing a specific SNN associated to the spatial abstract concepts of horizontal/vertical and left/right. Beyond the main objective of simulating this learning process through a neurobotic model, the present experimentation also serves as a prototype model to further study the development of a general neural design, which could sustain the three different types of concept learning, as well as several forms of concept inside each category.

In its current form, the SNN model is limited by its small visual scale (retina) and a single color perception (black). The SNN design is also restricted to detect perfect horizontal or vertical stimuli. Hence, it would be unable to perform when seeing an angled stimulus in front of it, which is another possible test for the generalization property. In the same perspective, scaling up or down stimuli was not possible in this experiment, again from the limitative capability of the retina. However, these issues could be corrected in future works. Furthermore, a higher discrimination would be a desirable feature to include in the present SNN model, since it is needed in the above/below and same/different relational concepts, as well as its full validation from transfer tests. However, we believe that the core neural layers of this architecture would remain and could be used in more related complex studies.

Does the relational concept learning process emerge from experiences and synaptic modifications of an existing neural circuit, or does it need the addition of new neurons as in the developmental neural phases? Is the relational concept structured in a bottom-up neural hierarchy? Does the first-order perceptual level of categorization sustain the second-order relational abstract concept? As a start toward answering those questions from a neurobotic model perspective, the proposed SNN allows learning two spatial concepts from a specific set of neurons and synapses. At first, the learning rule was unknown for the robot, but as rewards were given, the SNN adapted its behavior from supervised reinforcements in an operant conditioning procedure. Also, the SNN exhibited a behavioral plasticity when changing the rewarding rule online.

In the present experiments, it is not necessary to discriminate stimulus patterns, for example, to differentiate the black square stimulus and the X shape stimulus. This lower level of perception was not required to achieve the spatial learning task for left/right and horizontal/vertical patterns. However, it certainly represents a critical step to reach the relational abstract learning level. For example, in the above/below scenario, determining the constant visual spatial referent while the location of the other visual pattern varies requires a perceptual discrimination and a functional action of comparison. This is a future work for our team to integrate the present model and build an SNN that links this spatial concept level to a second-order relational concept.

Another objective of this paper is to provide comparative experimental data between different computational robotic models, as well as developing benchmarks for testing incremental complexity scenarios in the field of abstract concept learning.

## 5. Conclusion

This paper shows that the proposed SNN, controlling virtual and physical robots, succeeded to learn the spatial concept of horizontal/vertical and left/right visual patterns from a conditioning procedure and synaptic modifications. This experiment intends to be a first step study to reach the second-order relational concepts as in the above/below case. We believe that this bioinspired approach may open new perspectives to reach higher artificial cognition in the neurobotic domain.

## Data Availability

The complete access to all parameters and result data used to support this study, as well as the SIMCOG software, is available from the corresponding author upon request.

## Conflicts of Interest

The authors declare that they have no conflicts of interest.

## References

- [1] T. R. Zentall, E. A. Wasserman, O. F. Lazareva, R. K. Thompson, and M. J. Rattermann, "Concept learning in animals," *Comparative Cognition & Behavior Reviews*, vol. 3, pp. 13–45, 2008.
- [2] T. R. Zentall, E. A. Wasserman, and P. J. Urquioli, "Associative concept learning in animals," *Journal of the Experimental Analysis of Behavior*, vol. 101, no. 1, pp. 130–151, 2014.
- [3] J. S. Katz, A. A. Wright, and K. D. Bodily, "Issues in the comparative cognition of abstract-concept learning," *Comparative Cognition and Behavior Reviews*, vol. 2, pp. 79–92, 2007.
- [4] A. A. Wright and J. S. Katz, "Generalization hypothesis of abstract-concept learning: learning strategies and related issues in macaca mulatta, cebus apella, and columba livia," *Journal of Comparative Psychology*, vol. 121, no. 4, pp. 387–397, 2007.
- [5] L. Chittka and K. Jensen, "Animal cognition: concepts from apes to bees," *Current Biology*, vol. 21, no. 3, pp. R116–R119, 2011.
- [6] J. S. Katz and A. A. Wright, "Same/different abstract-concept learning by pigeons," *Journal of Experimental Psychology: Animal Behavior Processes*, vol. 32, no. 1, pp. 80–86, 2006.
- [7] J. S. Katz, A. A. Wright, and J. Bachevalier, "Mechanisms of same-different abstract-concept learning by rhesus monkeys (*Macaca mulatta*)," *Journal of Experimental Psychology: Animal Behavior Processes*, vol. 28, no. 4, pp. 358–368, 2002.
- [8] G. L. Murphy, *The Big Book of Concepts*, MIT Press, Cambridge, MA, USA, 2004.
- [9] A. A. Wright, "Concept learning and learning strategies," *Psychological Science*, vol. 8, no. 2, pp. 119–123, 1997.
- [10] A. Avarguès-Weber, D. d'Amaro, M. Metzler, and A. G. Dyer, "Conceptualization of relative size by honeybees," *Frontiers in Behavioral Neuroscience*, vol. 8, p. 80, 2014.
- [11] A. Avarguès-Weber, A. G. Dyer, M. Combe, and M. Giurfa, "Simultaneous mastering of two abstract concepts by the miniature brain of bees," *Proceedings of the National Academy of Sciences*, vol. 109, no. 19, pp. 7481–7486, 2012.
- [12] A. Avarguès-Weber and M. Giurfa, "Conceptual learning by miniature brains," *Proceedings of the Royal Society of London*

- B: Biological Sciences*, vol. 280, no. 1772, article 20131907, 2013.
- [13] M. Giurfa, "Cognition with few neurons: higher-order learning in insects," *Trends in Neurosciences*, vol. 36, no. 5, pp. 285–294, 2013.
  - [14] M. Giurfa, S. Zhang, A. Jenett, R. Menzel, and M. V. Srinivasan, "The concepts of "sameness" and "difference" in an insect," *Nature*, vol. 410, no. 6831, pp. 930–933, 2001.
  - [15] R. Menzel, "The honeybee as a model for understanding the basis of cognition," *Nature Reviews Neuroscience*, vol. 13, no. 11, pp. 758–768, 2012.
  - [16] C. J. Perry, A. B. Barron, and K. Cheng, "Invertebrate learning and cognition: relating phenomena to neural substrate," *Wiley Interdisciplinary Reviews: Cognitive Science*, vol. 4, no. 5, pp. 561–582, 2013.
  - [17] J. L. Krichmar, "Neurorobotics—a thriving community and a promising pathway toward intelligent cognitive robots," *Frontiers in Neurobotics*, vol. 12, 2018.
  - [18] A. Cangelosi and F. Stramandinoli, "A review of abstract concept learning in embodied agents and robots," *Philosophical Transactions of the Royal Society B: Biological Sciences*, vol. 373, no. 1752, article 20170131, 2018.
  - [19] W. Gerstner and W. Kistler, *Spiking Neuron Models: Single Neurons, Populations, Plasticity*, Cambridge University Press, Cambridge, UK, 2002.
  - [20] W. Maass, "Networks of spiking neurons: the third generation of neural network models," *Neural Networks*, vol. 10, no. 9, pp. 1659–1671, 1997.
  - [21] G. Q. Bi and M. M. Poo, "Synaptic modifications in cultured hippocampal neurons: dependence on spike timing, synaptic strength, and postsynaptic cell type," *Journal of Neuroscience*, vol. 18, no. 24, pp. 10464–10472, 1998.
  - [22] N. Caporale and Y. Dan, "Spike timing-dependent plasticity: a hebbian learning rule," *Annual Review of Neuroscience*, vol. 31, no. 1, pp. 25–46, 2008.
  - [23] H. Markram, J. Lubke, M. Frotscher, and B. Sakmann, "Regulation of synaptic efficacy by coincidence of postsynaptic APs and EPSPs," *Science*, vol. 275, no. 5297, pp. 213–215, 1997.
  - [24] A. Avarguès-Weber, A. G. Dyer, and M. Giurfa, "Conceptualization of above and below relationships by an insect," *Proceedings of the Royal Society B: Biological Sciences*, vol. 278, no. 1707, pp. 898–905, 2011.
  - [25] A. Cyr, A. Avarguès-Weber, and F. Thériault, "Sameness/difference spiking neural circuit as a relational concept precursor model: a bio-inspired robotic implementation," *Biologically Inspired Cognitive Architectures*, vol. 21, pp. 59–66, 2017.
  - [26] N. Fremaux, H. Sprekeler, and W. Gerstner, "Functional requirements for reward-modulated spike-timing-dependent plasticity," *Journal of Neuroscience*, vol. 30, no. 40, pp. 13326–13337, 2010.
  - [27] Ł. Kuśmierz, T. Isomura, and T. Toyozumi, "Learning with three factors: modulating hebbian plasticity with errors," *Current Opinion in Neurobiology*, vol. 46, pp. 170–177, 2017.
  - [28] A. Cyr, M. Boukadoum, and P. Poirier, "AI-SIMCOG: a simulator for spiking neurons and multiple animats' behaviours," *Neural Computing and Applications*, vol. 18, no. 5, pp. 431–446, 2009.

## Research Article

# Control of a Humanoid NAO Robot by an Adaptive Bioinspired Cerebellar Module in 3D Motion Tasks

Alberto Antonietti <sup>1</sup>, Dario Martina <sup>1</sup>, Claudia Casellato <sup>2</sup>, Egidio D'Angelo <sup>2</sup>,  
and Alessandra Pedrocchi <sup>1</sup>

<sup>1</sup>Department of Electronics, Information and Bioengineering, Politecnico di Milano, Milano, Italy

<sup>2</sup>Department of Brain and Behavioral Sciences, University of Pavia,

Brain Connectivity Center Istituto Neurologico IRCCS Fondazione C. Mondino, Pavia, Italy

Correspondence should be addressed to Alberto Antonietti; [alberto.antonietti@polimi.it](mailto:alberto.antonietti@polimi.it)

Received 12 October 2018; Accepted 27 December 2018; Published 27 January 2019

Guest Editor: Somyot Kiatwanidvilai

Copyright © 2019 Alberto Antonietti et al. This is an open access article distributed under the Creative Commons Attribution License, which permits unrestricted use, distribution, and reproduction in any medium, provided the original work is properly cited.

A bioinspired adaptive model, developed by means of a spiking neural network made of thousands of artificial neurons, has been leveraged to control a humanoid NAO robot in real time. The learning properties of the system have been challenged in a classic cerebellum-driven paradigm, a perturbed upper limb reaching protocol. The neurophysiological principles used to develop the model succeeded in driving an adaptive motor control protocol with baseline, acquisition, and extinction phases. The spiking neural network model showed learning behaviours similar to the ones experimentally measured with human subjects in the same task in the acquisition phase, while resorted to other strategies in the extinction phase. The model processed in real-time external inputs, encoded as spikes, and the generated spiking activity of its output neurons was decoded, in order to provide the proper correction on the motor actuators. Three bidirectional long-term plasticity rules have been embedded for different connections and with different time scales. The plasticities shaped the firing activity of the output layer neurons of the network. In the perturbed upper limb reaching protocol, the neurorobot successfully learned how to compensate for the external perturbation generating an appropriate correction. Therefore, the spiking cerebellar model was able to reproduce in the robotic platform how biological systems deal with external sources of error, in both ideal and real (noisy) environments.

## 1. Introduction

This work belongs to neurorobotics, a discipline that has the objective to replicate typical animal behaviours in robotic platforms. Its aim is to develop systems that, through specific algorithms and computational models inspired by biology and physiology, are capable of mimicking the sensory and motor control mechanisms of animals and humans. This ambitious objective is pursued in order to develop a better understanding of the biological mechanisms that rule our behaviours. The obtained technology and systems will also provide valuable feed-back and feed-forward control functions that could introduce sensory-motor coordination in robots. In this work, we focused on a bioinspired cerebellar simulator integrated into the controller of a humanoid

robot. We tested its learning properties in the typical sensorimotor task of perturbed upper limb reaching [1].

Motor control is one of the main tasks of the central nervous system (CNS), and many hypotheses on its operating principles and mechanisms have been proposed. Considering the intimate relation between the motor control system and the sensory system in the motor execution, it is possible to refer to their combined behaviour as a sensorimotor loop. This loop combines both feed-forward and feed-back strategies where the sensory and cognitive processes are the inputs that generate the next motor output. Computationally, the CNS is represented by the system that processes the inputs and generates the outputs. The inputs consist of all the sensory information from external and proprioceptive receptors as well as the cognitive internal

signals. The output is the motor command directed to the muscles which will produce an effect on the environment. The sensorimotor loop comprehends many different substructures and, among the others, the cerebellum. It has a major role in the fine motor control and in the learning of motor tasks and association patterns. The cerebellum processes the data from many sensory channels (i.e., vestibular and proprioceptive) and combines them with the previous motor commands to produce the updated motor commands for the next execution. The cerebellum is also supposed to be involved in a large amount of cognitive learning processes [2]. The paradigms assessed in literature, stressing the cerebellar role, are the eye blinking classical conditioning for the associative tasks [3], the vestibule-ocular reflex (VOR) [4], and the perturbed upper limb reaching for the motor control [5].

More than half of all the brain neurons are located in the cerebellum, which accounts for just the 10% of the brain mass. The cerebellar cells are thus densely packed in the grey matter of the highly convoluted cerebellar cortex and in the four deep cerebellar nuclei, on both brain hemispheres. The cerebellar cortex is composed of three layers, which include at least five types of cells. The cerebellar structure and its functional behaviours have been deeply analysed. During this extensive study, many cerebellar computational models have been proposed and developed [6–9]. Among these, the phenomenological models obtained from computational motor control studies are the best candidates to solve the sensorimotor integration issue, since they use an abstract function-based approach. This kind of models is capable to deal with motor planning, internal models, state estimation, motor learning, and modularity [10]. A realistic approach based on neurobiology requires the use of interconnected adaptive spiking neural networks (SNN). These networks have the potential to reproduce good adaptive control systems for robots, considering how biological organisms perform excellent control using ensembles of interconnected neurons [11].

In previous works, we have tested a range of simplified, but realistic, cerebellar models into sensorimotor tasks [12–14]. The objective of this work was to implement a computational model in a robotic platform in order to validate its functionality and behaviour in real-time control problems. In particular, a robot controller has been integrated with the cerebellar-inspired network, which provides the system with the capability of motor learning. The component of the motor control system can be represented by their phenomenological models, such as the feed-back and feed-forward mechanisms of the internal models. The first is based on the ongoing error coming from the sensor updates, while the latter is based on the direct motor commands. To allow such integration between the robotic platform controller and the bioinspired spiking network, we needed to introduce the right interfaces within the modules. Three interfaces have been introduced; two that encode the desired inputs trajectories and the errors obtained into a spiking activity, and the other one that decodes the frequency of the output neurons into an angular value that can be then applied by the robot controller. The spiking neural

network has been simulated by the EDLUT platform, a SNN simulator which allows a real-time execution. By means of look-up tables, EDLUT bypasses the need to solve the differential equations governing the state of every network unit, thus reducing the computational load.

## 2. Materials and Methods

First, we defined a suitable version of the perturbed upper limb reaching protocol. This paradigm is used to enhance the cerebellar effect in the sensorimotor loop. The objective is to have the subject, the robot in this case, to follow a particular trajectory. At a certain point, an unexpected external force is applied which will then produce a perturbation in the performed trajectory. The same perturbation is then applied in a sequence of trials, so that the subject learns to predict the perturbation and thus to limit the error (acquisition phase). After that, the perturbation is suddenly removed, the subject generates an error in the opposite direction, which is canceled out in the following trials (extinction phase).

The network was tuned using a robot simulator to perform a physiological behaviour; therefore, we set the starting weight values between the different kinds of cells to provide activity frequencies matching the ones present in the literature. Then, we performed a brute force exploration to find the best combination of the model plasticity parameters.

Once the network was optimized, we proceeded to test its capability of generalization with other trajectories, different than the one used to train the network. To further investigate the network behaviour, we evaluated its performances with the real robot using the parameters derived from the tuning with the simulator. We evaluated how the different plasticities and the gain tuning affected the performances on a noisy environment and also how the network in the real robot can deal with the different perturbations (i.e., different trajectories).

A final test was performed using a network ten times larger, with the same trajectory and parameters, to verify how a more detailed SNN could alter the performances for the proposed motor task.

Summarizing, we have focused this work on three main objectives: (i) the optimization of the upper limb reaching protocol, adapting it to the NAO robot to simultaneously control 3 degrees of freedom (DoFs); (ii) the parameter tuning of the SNN, to replicate the physiological behaviour of its constituent neurons and of the resulting robot behaviour; and (iii) the exploitation of the optimized network on different trajectories (transfer learning).

*2.1. Simulated and Real Robots.* NAO is an integrated, programmable, medium-sized humanoid robot developed by Aldebaran Robotics. NAO (version V3.3) is a 58 cm, 5 kg robot, communicating with remote computers via an IEEE 802.11 g wireless or a wired Ethernet link. The NAO has 21 DoFs and features a variety of sensors. Since we were interested in arm movements, we controlled three joints of the robot left shoulder and elbow (Figure 1(c)): shoulder pitch (Joint 1), elbow yaw (Joint 2), and elbow roll (Joint 3).

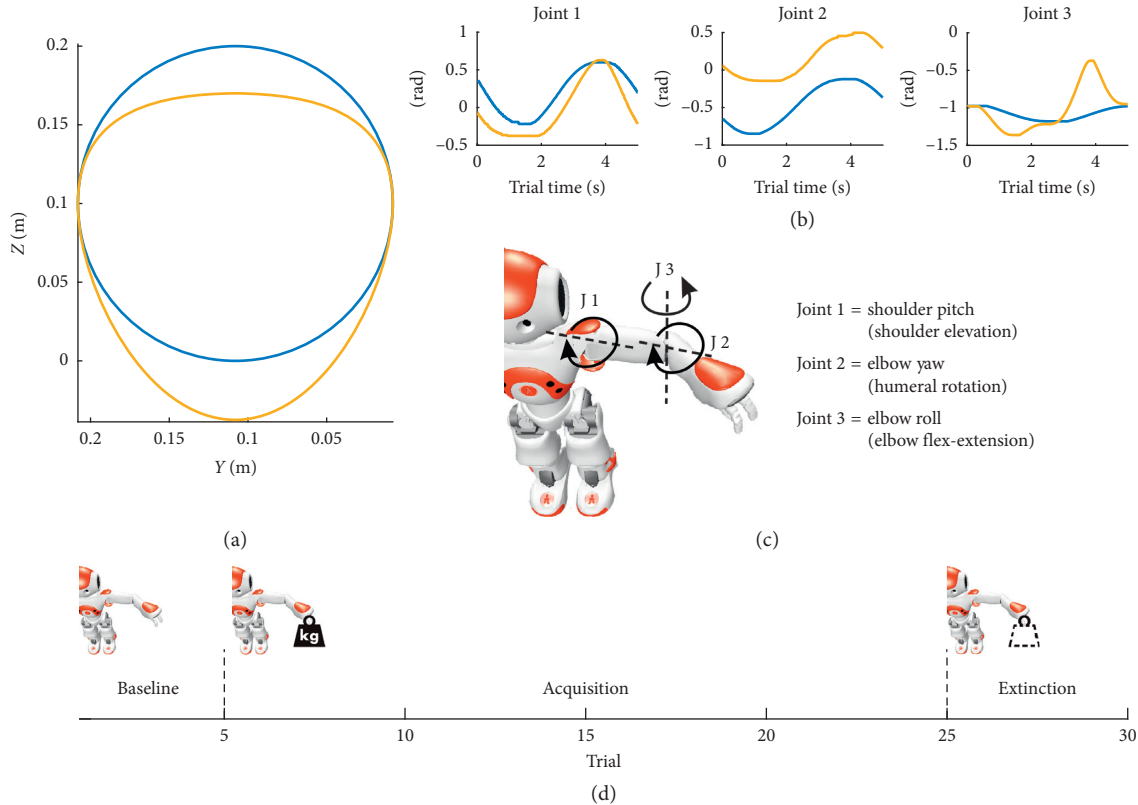


FIGURE 1: Trajectories and experimental protocol. (a) Planar representation ( $Y$ - $Z$  axis, in the robot reference frame) of the ideal (blue) and perturbed (yellow) Cartesian trajectories. The corresponding trajectories in the joint space are depicted in panel (b). (c) The controlled joints of the robot correspond to three rotations: shoulder elevation (Joint 1), humeral rotation (Joint 2), and elbow flex extension (Joint 3). (d) The experimental protocol consists of 5 baseline trials, 20 trials of acquisition, where a load is applied to the robot arm, and 5 trials of extinction, where the additional load is removed.

To interface the robot with the neural network, able to run in real time with a frequency of 1 kHz, a stable frequency update was a strict requirement. For this reason, the robot was commanded by means of the device communication manager (DCM). The DCM is the software module that is in charge of the communication with all electronic devices in the robot (boards, sensors, actuators, etc.). It is the link between high-level functions and low-level controllers. The DCM has a separate real-time thread that runs every 10 ms, thus guaranteeing a stable refresh rate of 100 Hz.

NAO robot cannot be controlled directly in torque/current to the motors, but only in position. This forbids to physically perturb the arm reaching motion task with an external force. In case of a lower force, the robot arm would just reach the desired angle, while in case of a higher force the motor would stall without moving at all. For this reason, two different trajectories were used: one ideal trajectory used as the desired path and another *perturbed* trajectory, to be corrected by the network using the angular errors of the joints as learning signals.

Since the network optimization process will need hundreds of tests, we used a robot simulator called Webots. This simulator allows launching a simulated NAO moving in a virtual world, offering a safe place to test behaviours before deploying them on a real robot. Considering the level of

control offered by the DCM and the unpredictable behaviour of the SNN, especially in tuning phase, a simulator was ideal to test how the motor commands would be affected and to prevent dangerous commands to be sent to the real robot. While being a very accurate simulator for the NAO, as with any other simulator, some nonidealities are not considered (e.g., nonlinear friction, sensor errors, and motor overheating).

**2.2. Cerebellar Model.** In this work, a cerebellar-inspired SNN, based on previous versions presented and tested in [12, 13], was used to prove its adaptation capabilities in a complex motor task. The cerebellar neural network used has the following architecture (Figure 2(a)), built taking inspiration from physiological studies of the cerebellum, in a tight collaboration with neuroscientists. The SNN was composed of 6480 Leaky Integrate and Fire neurons replicating the cerebellar microcircuit: 300 mossy fibers (MFs), the first input of the cerebellar network, organized in 6 groups of 50 cells each: 3 groups, one for each controlled joints, encoding information on the desired positions and 3 groups encoding information on the desired velocities; 6000 granular cells (GrCs), generating a sparse representation of the state input; 72 inferior olive neurons (IOs), the second



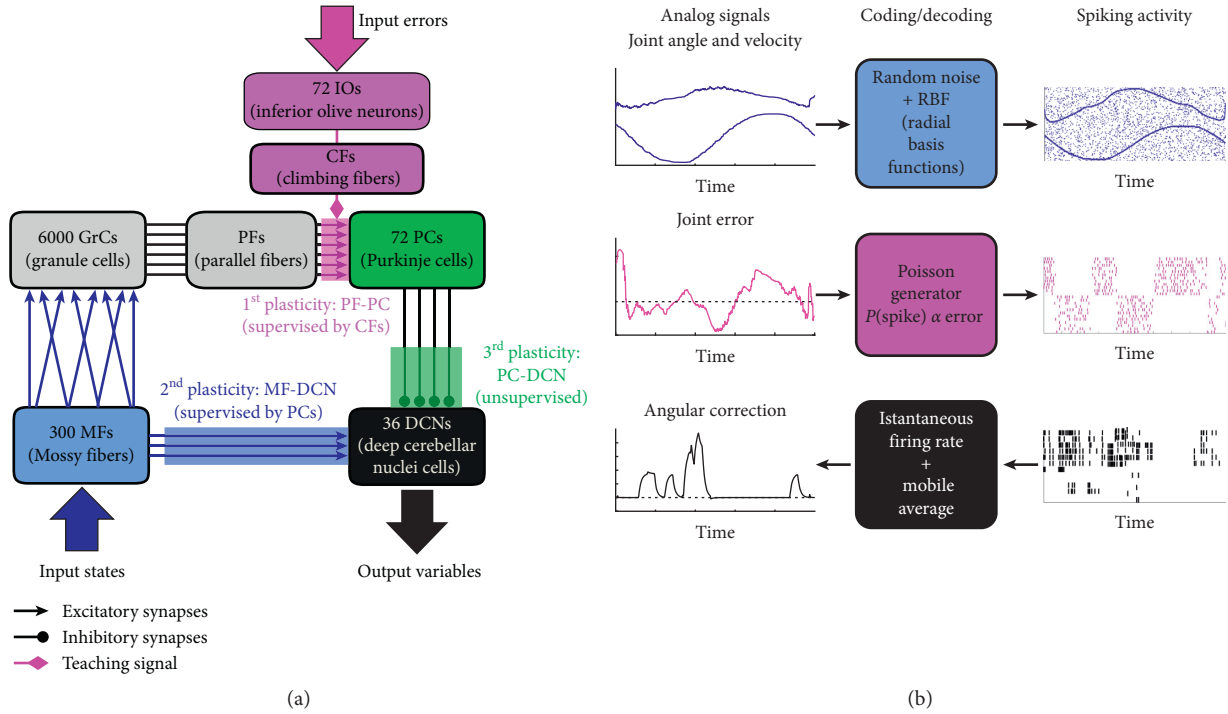


FIGURE 2: Cerebellar SNN and coding/decoding strategies. (a) The computational model applied for creating the cerebellar SNN embedded into the controller of NAO robot. Each block represents a neural population, with the relative inputs and outputs. The excitatory, inhibitory, and teaching connections are depicted. The shaded areas represent the three plasticity sites: magenta the PF-PC synapses, blue the MF-DCN synapses, and green the PC-DCN synapses, adapted from [15]. (b) Coding (for MFs and IOs) and decoding (for DCNs) strategies implemented to integrate the analog robotic world with the spiking activity of the SNN. The 3 joint angles and angular velocities are fed as input to the MFs by means of an RBF approach, overlapped to a random activity. Each joint error is transformed into IO spikes by means of Poisson generators, which produce spikes with a probability that is proportional to the error magnitude. Each IO generates a spike pattern that is therefore independent of their history and of the other IOs. The DCN spikes are transformed into an angular correction sent to the robot joints by means of an instantaneous firing rate computation, subsequently averaged with a mobile-window filter.

cerebellar input, with their respective climbing fibers (CFs); IOs are divided into 6 groups of 12 cells each, 3 groups, one for each joint, encoding the positive errors and other 3 groups encoding the negative ones; 72 Purkinje cells (PCs), the integrators of the sparse state-information coming from the GrCs through the parallel fibers (PFs) with the error-information coming from the IOs through the CFs; 36 deep cerebellar nuclei neurons (DCNs), which are the only output of the cerebellar microcomplex, thus producing the cerebellar output variable, divided in 6 groups, two for each joint, where one group controls the compensation of positive errors (i.e., agonist muscles) and the other compensates for negative errors (i.e., antagonist muscles).

Three interfaces (Figure 2(b)) were implemented to transform analog signals into spiking activity to be fed to the network (input) and vice versa (output).

The first interface computes the input current for MFs with a radial basis function (RBF) method. This current  $I(t)$  is used to increment the membrane potential  $V_m(t)$  of the MF. RBF centers are distributed equally along the sensory dimensions, with their widths tuned to ensure a small overlap in the response of consecutive MF. One-dimensional values are converted into multidimensional current vectors, one for each RBF. Every MF has its own receptive field to

encode the analog information, normalized between  $-1$  (minimum value) and  $1$  (maximum value).

The second interface converts joint errors into IO spikes. These neurons have a low firing rate (less than 10 Hz) that could prevent the representation of high-frequency error signal related to the task being learned. This issue can be fixed exploiting the irregular firing of the IO by statistically sampling the entire error signal over multiple trials. It has been observed that the temporal distribution of the spikes of IOs shares similar characteristics as the Poisson model. IOs fire randomly in behaving animals at rest and during the ocular following response and arm-motion tasks in monkeys. This stochastic characteristic firing enhanced the input-output mutual information despite the ultralow firing rates of CFs [16]. The firing rate is reproduced with a Poisson model of spike generation and, at every time step, IO spikes are randomly generated with a probability that is proportional to the error magnitude. This approach has been employed to generate independent spike patterns on multiple IO neurons. For each IO, the firing probability is therefore independent of the previous spiking activity and from the activity of the other IOs [17, 18]. Substantial evidence supports a role for CFs in error signalling and

motor learning, and the proportionality between the error signal and the spiking activity of CFs has been verified [19, 20].

The third interface decodes DCN spike patterns into analog angular values. First, the instantaneous firing rate of every DCN is calculated, and then positive and negative DCN firing rates are averaged with a mobile time window of 200 samples (i.e., 200 ms). The cerebellar output is obtained by calculating the net difference between the two averaged mean DCN firing rates (positive and negative) [12].

Thanks to these interfaces, the SNN could be integrated into the robotic platform controller, with the function of a feed-forward predictive controller.

The SNN neurons are connected in three possible ways:

- (i) Excitatory connections: synapses in which an action potential in a presynaptic neuron increases the probability of an action potential occurring in a postsynaptic cell. There are excitatory connections between MFs and GrCs, between MFs and DCNs, and between GrCs and PCs.
- (ii) Inhibitory connections: synapses in which the impulse in a presynaptic cell results in a reduced likelihood for a postsynaptic cell to produce an action potential. There are inhibitory connections between PCs and DCNs.
- (iii) Teaching connections: connections that encode teaching spike trains (related to the error) for the supervised learning in plasticity sites of the cerebellum.

According to neurobiological studies, three plasticity sites have been identified in the human cerebellum: at the level of PF-PC excitatory connections; at the level of MF-DCN excitatory connections; and at the level of PC-DCN inhibitory connections [21–24].

The SNN model was equipped with three plasticity sites, at cortical (PF-PC) and nuclear (MF-DCN and PC-DCN) levels. The synaptic connections in each site followed three different learning rules, which strengthen or weaken these connections by long-term modifications: long-term potentiation (LTP) and long-term depression (LTD). LTP and LTD mechanisms were modeled as modifications on the synaptic conductances as described in detail in [13, 15]. In general, the three mechanisms were based on different kinds of Spike-Timing-Dependent Plasticity (STDP), but each one was tailored to the specific experimentally measured mechanism. The first plasticity (PF-PC) modulates the activity of PCs, increasing or decreasing the synaptic strength of the connections under the supervision of the IO activity. The second plasticity (MF-DCN) is also a supervised learning rule; in this case, the PC activity is the modulator signal that influences the synaptic weights. The third plasticity (PC-DCN) is an unsupervised standard STDP, where the weight modifications are driven uniquely by the timing of the presynaptic (PC) and postsynaptic (DCN) neurons.

For the initialization of the network synaptic weights, we referred to physiology values. MF activity has been set to a frequency comprised around 50 Hz, by adjusting the

background random activity and the overlap and bell width of the RBFs. MF-GrC weights have been set to achieve a GrC frequency of 3–6 Hz and the GrC-PC weights to produce a PC frequency around 40–60 Hz. MF-DCN weights were set in order to have a DCN frequency around 25 Hz in absence of PC inhibition (PC-DCN weight = 0). The last step consisted in adjusting PC-DCN weights, nullifying the DCN activity in presence of a stable PC activity around 45 Hz.

To perform the simulations in real time, we leveraged the EDLUT simulator [25], an open source simulator of SNN that provided a reduction of the computational loads, speeding up the network simulation by means of look-up tables. In fact, with a standard simulator (e.g., NEURON [26], NEST [27, 28], or Brian [29]), the program has to solve one or more differential equations for each neuron and cannot guarantee the real-time performances that are required in interfacing a real robotic platform.

*2.3. Experimental Protocol.* We challenged the SNN in a 3D motion adaptation protocol, similar to adaptation protocols based on force-fields performed on human subjects [30–32]. The ideal trajectory that the robot wants to perform is a planar circle of 0.1 m radius, executed in the Y-Z plane and with center  $Y = 0.1$  m and  $Z = 0.1$  m (Figure 1(a), blue line). When an unexpected load is virtually added to the robot hand, the trajectory deviates from the desired one, being deformed toward the ground (Figure 1(a), yellow line). As a result, the three controlled joint angles deviated from the ideal paths (Figure 1(b)), thus generating positive and negative errors for each DoF.

The experimental protocol consisted in 30 trials divided into three phases (Figure 1(d)): the first one was the baseline phase, in which the command for the robot was the ideal trajectory and lasted for 5 trials. The second phase was the acquisition phase that lasted for 20 trials and in which the input for the robot was the perturbed trajectory. The last one was an extinction phase of 5 trials, in which the input was again the ideal trajectory. In order to mimic the adaptation capabilities of the cerebellum, the goal of the SNN was to minimize the joint errors, thus reducing the subsequent Cartesian errors in the 3D space.

*2.4. Parameter Tuning.* As mentioned above, there are three different plasticity sites that can modify the behaviour of the SNN, each one is characterized by two learning parameters: LTP and LTD. In order to assess the best values for these six parameters, a brute force exploration has been performed. The first plasticity (cortical plasticity, PF-PC) is the main cause of the learning effect, as it regulates the activity of the PC which depresses the DCN output. The other two plasticities (nuclear plasticities, MF-DCN, and PC-DCN) have a secondary effect, affecting the error reduction performance on a longer time scale and with a lower magnitude. The parameter tuning tests have been performed with Webot simulator, to prevent damages and avoid unpredictable movements of the robot arm due to unexpected behaviour of the network.

To evaluate the network performance, we calculated a global cost function, which we wanted to minimize. The cost function is the sum of two quality metrics. Both metrics take into account the root mean square error (RMSE) of all the three joints. For each trial, RMSE for every joint was computed over the 5000 ms of trial time, and then the three RMSEs were averaged. The average RMSE for the  $i^{\text{th}}$  trial is computed as

$$\text{RMSE}_{\text{Avg}}(i) = \frac{\text{RMSE}_{\text{Joint1}}(i) + \text{RMSE}_{\text{Joint2}}(i) + \text{RMSE}_{\text{Joint3}}(i)}{3} \quad (1)$$

The first quality metric computed a weighted average of  $\text{RMSE}_{\text{Avg}}$  in the acquisition and extinction phases. While it is normal to have higher errors in the first acquisition trials, a good cerebellar controller should gradually correct the ongoing joint errors. This metric rewards SNN showing a good correction in the late stages of the acquisition and also low extinction errors:

$$\text{RMSE}_{\text{Weighted}} = \frac{\sum_{i=6}^{30} \text{RMSE}_{\text{Avg}}(i) \cdot \text{weight}(i)}{25} \quad (2)$$

where

$$\text{weight}(i) = \begin{cases} \frac{i-4}{3}, & \text{if } 6 \leq i \leq 25 \text{ (acquisition phase),} \\ 4, & \text{if } i > 25 \text{ (extinction phase).} \end{cases} \quad (3)$$

The second quality metric measures the stability of the correction, computing the standard deviation (SD) of the trials 21–25 (i.e., the last 5 trials of acquisition). High values of LTP and LTD parameters could lead to fast changes in the RMSE in the acquisition phase, but also to its instability. This leads to a high standard deviation of the RMSE, especially in the last five trials, where the minimum error should have been reached already:

$$\text{STD} = \frac{\sqrt{\sum_{i=21}^{25} (\text{RMSE}_{\text{Avg}}(i) - \overline{\text{RMSE}_{\text{Avg}}})^2}}{5} \quad (4)$$

Finally, a global cost function, whose minimum should identify the most performing model in the explored area, is calculated normalizing  $\text{RMSE}_{\text{Weighted}}$  and STD over their maximum and minimum values, thus obtaining values between [0-1], and then summing them to obtain a global cost value in the range [0-2].

For the first plasticity, we evaluated an  $11 \times 11$  matrix, with LTP1 values ranging from 0 to 0.01 with steps of 0.001 and LTD1 values ranging from 0 to 0.05 with steps of 0.005. The exploration was performed iteratively, choosing an LTP value and pairing it with all the LTD values and then repeating the process for all the other LTP values. For each LTP and LTD combination, a complete simulation of the protocol was performed, and the final global cost value was computed. After the first exploration, a second one has been performed in the area of the global minimum of the cost function, with finer steps, testing other  $10 \times 10$  values. The

best LTP-LTD configuration has then been chosen for the tuning of the other nuclear plasticities.

For the nuclear plasticities, the LTP1 and LTD1 resulting from the previous exploration have been kept fixed, and the exploration has been performed on LTP and LTD parameters (i.e., LTP2, LTD2, LTP3, and LTD3). The evaluation was similar to the first plasticity, with the exception of the parameter ranges. LTP and LTD ranged from  $10^{-10}$  to  $10^{-1}$  with a  $\times 10$  steps. As before, a second exploration in the best area identified was performed. The second search covered a  $10 \times 10$  parameter area centered on the best parameter identified in the first exploration, testing half of the below and above values (i.e.,  $[0.5 \ 0.6 \ 0.7 \ 0.8 \ 0.9 \ 1 \ 2 \ 3 \ 4 \ 5] \times 10^j$ , where  $j$  is the best generation exponential).

Once the plasticities values have been set, another parameter to consider is the gain needed to convert the analog output of the network in an angular value (in radians). Since each joint has different ranges and different errors amplitude, a proper gain for each joint has to be used. To find the optimal gain values, a brute force exploration has been performed with a gross exploration (i.e., testing gain values ranging from 0.005 to 0.05 with steps of 0.005) and a subsequent finer exploration (i.e., testing 10 gain values centered on the best result of the gross exploration, with steps of 0.001). The gain factor is particularly relevant due to the normalization of the angular values and the error that is given as input to the network. As the network manages values comprised between 0 and 1 for all joints, its output does not consider the differences in the actual angular errors. Therefore, a joint with small angular error will require a lower gain, while more perturbed joints will require a greater gain.

*2.5. Transfer Learning.* Having identified the set of the network parameters (i.e., LTP1–3, LTD1–3, and gain 1–3) which produced the best performances, we have verified if (i) the SNN was able to compensate for an external perturbation a 3D movement performed by a physical NAO robot and if (ii) the SNN was able to compensate different perturbations on both simulated and physical robotic platform.

Therefore, we executed 10 tests with both Webot simulator and NAO robot, in order to verify the robustness of our controller in a noisy system performing the same protocol used for the SNN optimization.

To verify the transfer learning capabilities of the cerebellar model, we have executed 10 tests with both Webot simulator and NAO robot in variations of the protocol, with 3 other couples of ideal and perturbed trajectories: two deformations of the ideal circle trajectory (an oval and a squared deformation) and with ideal and deformed  $\infty$ -shaped trajectories.

*2.6. Network Enhancement.* One of the limits of the network used is the low number of output cells which limits the resolution of the correction, leading to jerky angular trajectories. Therefore, we tested an expanded version of the SNN, to observe how the network size can change the overall

performances of the cerebellar-inspired controller. Each neural population was increased ten-fold, maintaining the same connectivity rules explained above. All parameters have been kept the same as the ones used with the normalized network, and the gain has been reduced by ten, in order to match the increased number of output cells. A side effect of the increased size of the network is the loss of the real-time property due to a larger number of spikes to be processed. Therefore, the larger network was tested for a single test instead of the usual 10 tests. Also in this case, we tested also the three additional trajectories to verify the generalizability of the learning properties of the SNN.

### 3. Results and Discussion

*3.1. Parameter Tuning.* After every plasticity gross exploration, the parameter space area resulting in the best performance, according to the developed cost function, was further explored. The RMSE over all trials was computed for 10 tests, using the parameters found during the optimization, in order to verify the behaviour of the SNN over the different phases.

In Figure 3(a), it is possible to see the effect of LTP1 and LTD1 on the quality of the correction: there are three main areas that is possible to identify. The first one is the lower-left corner, where LTD is too low and LTP is consistently higher (blue cross). Since the LTD is the major player in the attenuation of PC activity and the consequent increase of DCN activity, the network does not perform well in the acquisition phase (i.e., there is no learning) while it performs well in the extinction phase as there is no overcompensation when the additional load is removed (Figure 3(c), blue line). The second area is the middle right corner, where LTD is higher than LTP (green cross). Here the activity of the DCN reaches high levels, and since the correction is strong, this is the worst area for the extinction phase. Note that also in acquisition, this area is not useful, as a too fast and aggressive correction leads to instability in the final trial of this phase (Figure 3(c), green line). Finally, there is the area around the principal diagonal, where we can find lower values of the cost function. The top central area containing the global minimum (red square) is the area chosen for the finer exploration (Figure 3(b)).

The finer exploration produced more uniform results, but it was still possible to exclude the lower area with too high values of LTD, where the correction was insufficient and unstable. The global minimum of this exploration corresponded to the parameters  $LTP1 = 0.0006$  and  $LTD1 = 0.015$ . As already proved in previous works [21–23, 33], the cortical LTD has greater values with respect to the LTP. This combination of parameters was tested ten times to assess the reproducibility of the results (Figure 3(d)), and it was then used during the tuning of the nuclear plasticities.

The results obtained after the second plasticity (MF-DCN) gross exploration are shown in Figure 4(a)). It is evident that the highest errors are present in the bottom right area, where the high LTP produce an

overcompensation effect. Note that, for this plasticity, LTP2 is the main responsible for the increased activity of the DCN while LTD2 concurs to their attenuation. In the right area, too high LTD2 leads to the absence of DCN activity and therefore of the correction. In the left area, the LTD2 allows an activity from the DCN, and thus the better results. We investigated the top left area, containing the global minimum. The finer exploration (Figure 4(b)) was almost uniform; therefore, we identified the minimum global cost function for the combination of parameters  $LTP2 = 10^{-9}$  and  $LTD2 = 2 \cdot 10^{-10}$ . As in other protocols Medina et al. [34]; Antonietti et al. [13]; Mauk and Ruiz [35]; and Medina and Mauk [36], the MF-DCN plasticity parameters have significantly lower values than the cortical plasticity, thus confirming the hypothesis that the effect of nuclear plasticities becomes meaningful on longer time scales.

The third plasticity (PC-DCN) gross exploration produced almost uniform results, if compared to the other two plasticities (Figure 4(c)). In the right area, the LTD is too high, and therefore, the PCs could not selectively inhibit the corresponding DCN. Even if more combination of LTP3 and LTD3 gave low cost function values, without defining a specific area, the parameter space near the global minimum was explored in the finer search. The finer exploration (Figure 4(c)) revealed homogeneous performances without particular spots of interest. The global minimum of this exploration corresponded to the parameters  $LTP3 = 10^{-2}$  and  $LTD3 = 10^{-7}$ .

*3.2. Simulated and Real Robot Performances.* Having optimized the three learning rules, 10 tests were performed with only the cortical plasticity and with all the plasticities activated (Figure 5(a)). It becomes clear that the performance improvements given by the addition of the nuclear plasticities were negligible. As already mentioned, the main effect of nuclear plasticities could be seen on a longer time scale. It has been demonstrated [13] that the benefits of the nuclear plasticities can be verified in long paradigms, after more than 100 trials, possibly when more repeated sessions of acquisition and extinction are repeated. In addition, the possible improvements provided by the nuclear plasticities could be hidden by the nonnegligible variability between the 10 performed tests.

Once the three plasticities have been optimized, we proceeded with the tuning of the three joint gains. In the previous cases, all the joints used the same gain value of 0.012, theoretically derived from the foreseen maximum joint errors. The first rough exploration confirmed values near the ones already used. The results of the finer exploration identified the optimal gains as follows: Gain 1 = 0.005, Gain 1 = 0.013, and Gain 1 = 0.012. Since we have optimized the network plasticities with a fixed gain of 0.012, it is reasonable that the obtained gains are not very different from the original one.

Testing the SNN with optimized gains (Figure 5(b)), we obtained a generally lower error and a more stable trend in the acquisition phase, where the appropriate gain makes the intervention of the network more adequate in compensating

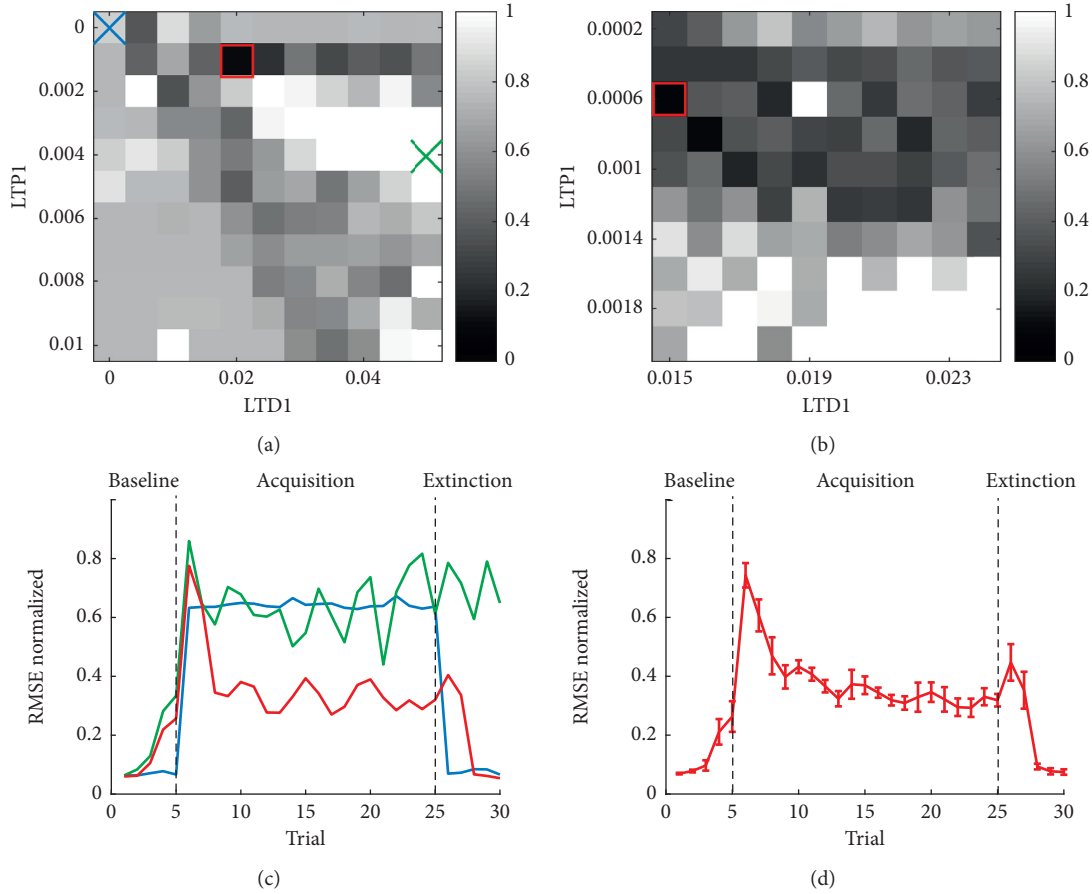


FIGURE 3: Cortical plasticity optimization. (a) Cost function resulting from the gross exploration of LTP1 and LTD1 parameters. Darkest values represent low values of the cost function, therefore the best combinations of the two plasticity parameters. The parameter space further explored in the finer search (b) is identified by the red square. Blue and green crosses identify two examples parameters giving bad performances (c). (b) Cost function resulting from the finer exploration of LTP1 and LTD1 parameters. The red square identifies the global minimum, therefore the chosen combination of LTP1 and LTD1. (c) Three examples of RMSE performance across the 30 trials of the protocol. The red line represents a good performance, with a reduction of the RMSE during the acquisition phase and a good extinction in the last 5 trials. The blue line represents the combination of  $LTP1 = 0.0$  and  $LTD1 = 0.0$ ; therefore, no correction happened in the acquisition phase, leading to a high cost function value. The green line represents a combination of too high LTP1 and LTD1, leading to an unstable and ineffective correction along the trials. (d) Mean and SD of the RMSE in 10 tests performed with the Webot simulator with the best combination of LTP1 and LTD1 identified in the finer exploration.

the error, thus reducing the overcorrection effects leading to instability.

Having assessed the performance of the SNN in an almost ideal environment (the Webot simulator), we proceeded to test the model performance in the real world with NAO robot. The ten tests performed with NAO robot (Figure 5(b)) showed a proper correction in the acquisition phase, the after-effect at the beginning of the extinction phase, and a good extinction in the last trials. As expected, the Webot simulator performed slightly better than NAO robot, with smaller variance. However, the performance obtained with the NAO robot was still similar, with a good error reduction and similar physiological behaviour. Given the higher variability with the NAO robot, it would be even more difficult to notice differences between the performances of a SNN equipped with the cortical plasticity or with multiple plasticities.

**3.3. Transfer Learning Performances.** We wanted to test the transfer learning capabilities of the proposed SNN controller; we thus challenged the optimized SNN with three different ideal and perturbed trajectories (Figures 6(a), 6(d), and 6(g)). For each trajectory, we have adapted the gain values proportionally to the maximum error of every joint. Then, we tested the different shapes in Webot simulator (Figures 6(b), 6(e), and 6(h)) and in the NAO robot (Figures 6(c), 6(f), and 6(i)).

In the Webot simulator tests, comparing the error trends over time with the one obtained using the original trajectory, it is possible to notice a slightly higher variability exhibited by the oval trajectory, while the infinite and square trajectories performances were similar to the one obtained with the original perturbation. However, in all the cases, the overall performances were similar to the one achieved with the training trajectory.

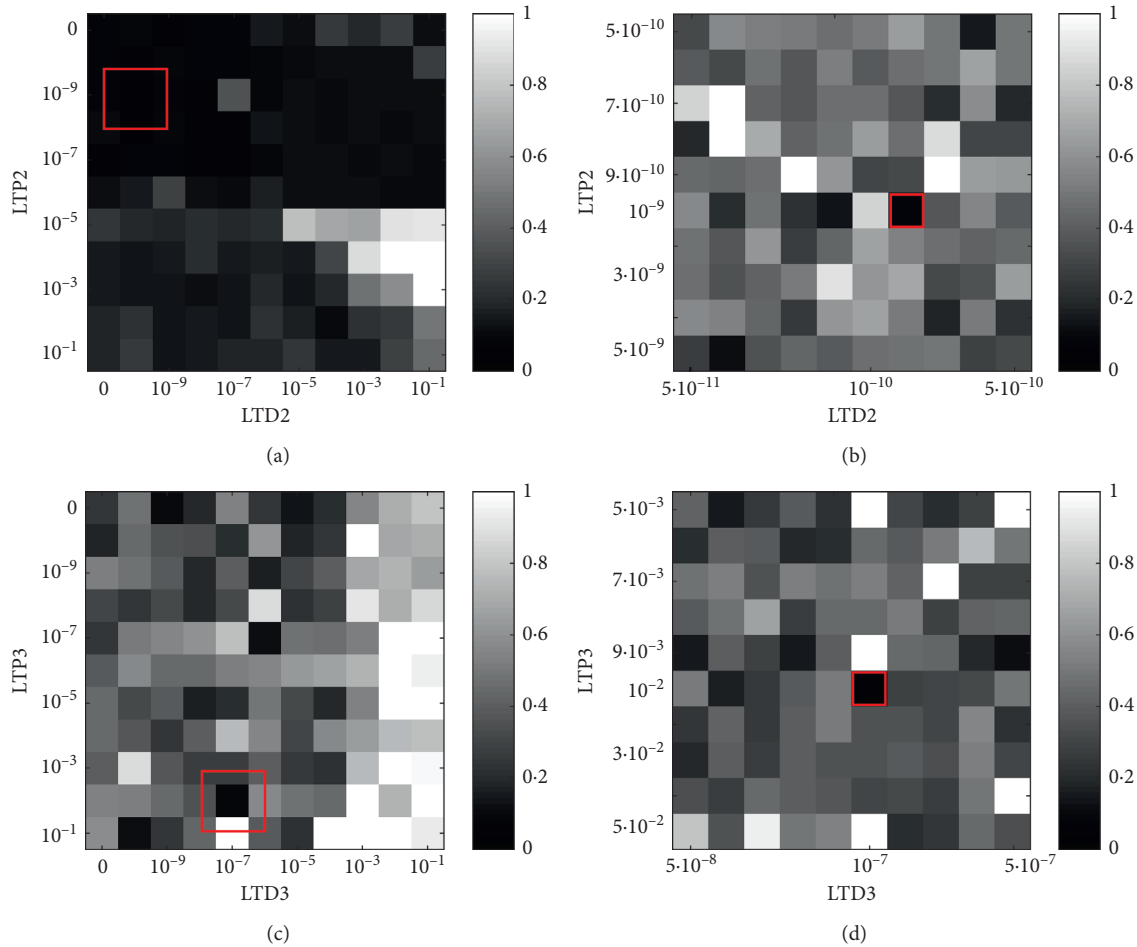


FIGURE 4: Nuclear plasticities optimization. (a, b) Cost functions resulting from the gross and finer explorations of LTP2 and LTD2 parameters. Darkest values represent low values of the cost function, therefore the best combinations of the two plasticity parameters. The parameter space further explored in the finer search (b) is identified by the red square (a). (c, d) As (a, b), but for the gross and finer exploration of LTP3 and LTD3.

In the NAO robot tests, differently from what was obtained with the Webot simulator, the worst performance was obtained with the infinite trajectory. This result is justified being the infinite trajectory, the one with the lower angular errors, with values more affected by the overall noise. Therefore, the SNN was less efficient and could not perform as well as in the other trajectories.

**3.4. Network Enhancement.** One of the limits of the SNN used so far is the low number of output cells (DCN) which limits the resolution of the correction. As a result, the cerebellar correction on the joint angular values was jerky. To compensate for this effect, we tested a larger version (ten times larger) of the same network. All parameters have been kept the same as the ones used with the normal-sized network, and the gain has been reduced by a factor ten to match the increased number of output cells. A side effect of the increased size of the network is the loss of the real-time property, due to a larger number of spikes to be processed. Therefore the larger network was tested with both Webot simulator (Figure 7(a)) and NAO robot (Figure 7(a)) for a

single test, instead of the usual 10 tests. The main improvements with respect to the normal-sized network were the initial error in the baseline phase, which remains around zero, and the lower and more stable RMSE in the acquisition phase. The other difference is in the extinction phase where the higher correction produces a higher overcompensation effect, and it requires more time to return to the initial state with respect to the normal-sized network.

The transfer learning capabilities were maintained in the larger SNN, also in these cases with smoother and more stable corrections of the joint errors in all the three additional trajectories. It is possible to notice that the enhancement of the SNN, augmenting the resolution of the network, made it slower in the adaptation processes. However, the parameter tuning carried out using the original SNN could be reused in the larger SNN, without having to rerun the optimization process (which would be unfeasible, given the extended computational loads of the larger SNN).

**3.5. Neural Behaviour.** We have also evaluated the network activity. The spikes generated by all the cells have been

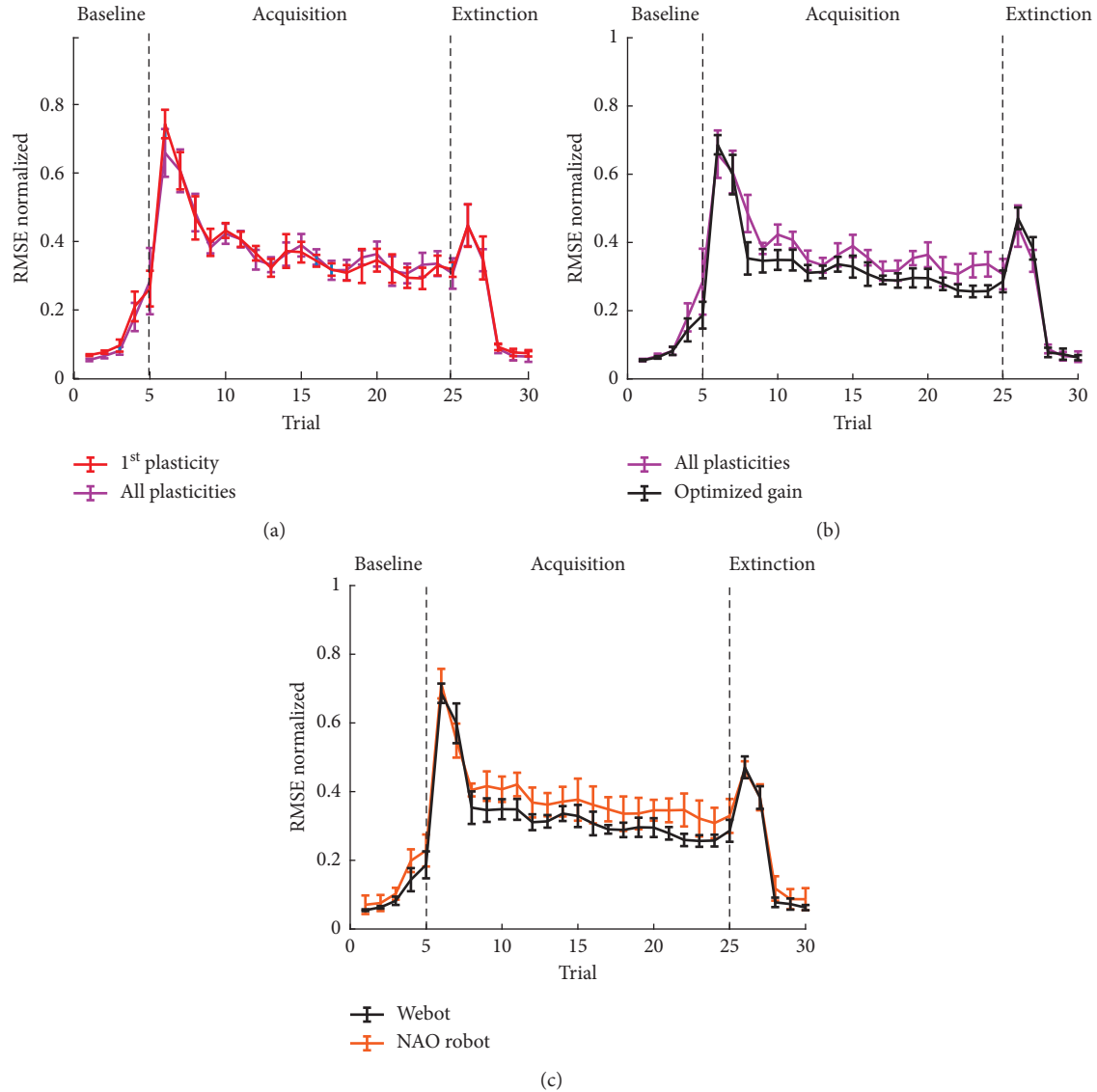


FIGURE 5: RMSE in different testing conditions. (a) Mean and SD of the RMSE computed for 10 tests with only the cortical plasticity optimized (in red) and after the optimization of the cortical and nuclear plasticities (in magenta). (b) Mean and SD of the RMSE computed for 10 tests after the optimization of the cortical and nuclear plasticities (in magenta) and after the optimization of the gain (in black). (c) Mean and SD of the RMSE computed for 10 tests after the optimization of the gain with Webot simulator (in black) and with NAO robot (in orange).

recorded during the testing phases and they could be analysed to verify how the errors affected the activity of the neuronal populations over the trials. The MFs kept an almost constant frequency over all the trials, with values comprised between 44 and 47 Hz. The GrCs were also almost constant with a frequency between 6 and 7 Hz; given the high number of these cells, their monitoring was quite challenging, and therefore their spike data were not collected in all the tests. PCs, IO, and DCN are the cells that explain the behaviour of the network, and from their variation in frequency, we can evaluate the physiological similarity of our system with a real biological one.

For every test, we recorded the ideal and real joint values, together with the actual Cartesian trajectory performed by the robot hand. Here, we report the network activity and the

relative Cartesian and angular trajectories for the circle trajectory perturbed by an additional load application at the robot hand using the NAO robot and the enhanced SNN. Analyzing the salient trials of the protocol (see also the video provided as Supplementary Materials (available here)), it is possible to notice how the network activity shapes the robot behaviour and vice versa.

In the first trial of the baseline phase (Figure 8(a)), the robot is performing a correct trajectory, therefore IO activity is low, and the PCs are firing without restrictions. As a result, the output from the DCN is almost null.

In the first trial of the acquisition phase (Figure 8(b)), the robot hand is deviated by the additional load attached. The increased joint errors trigger the IO activity which rises consistently, although the IO population has a generally low

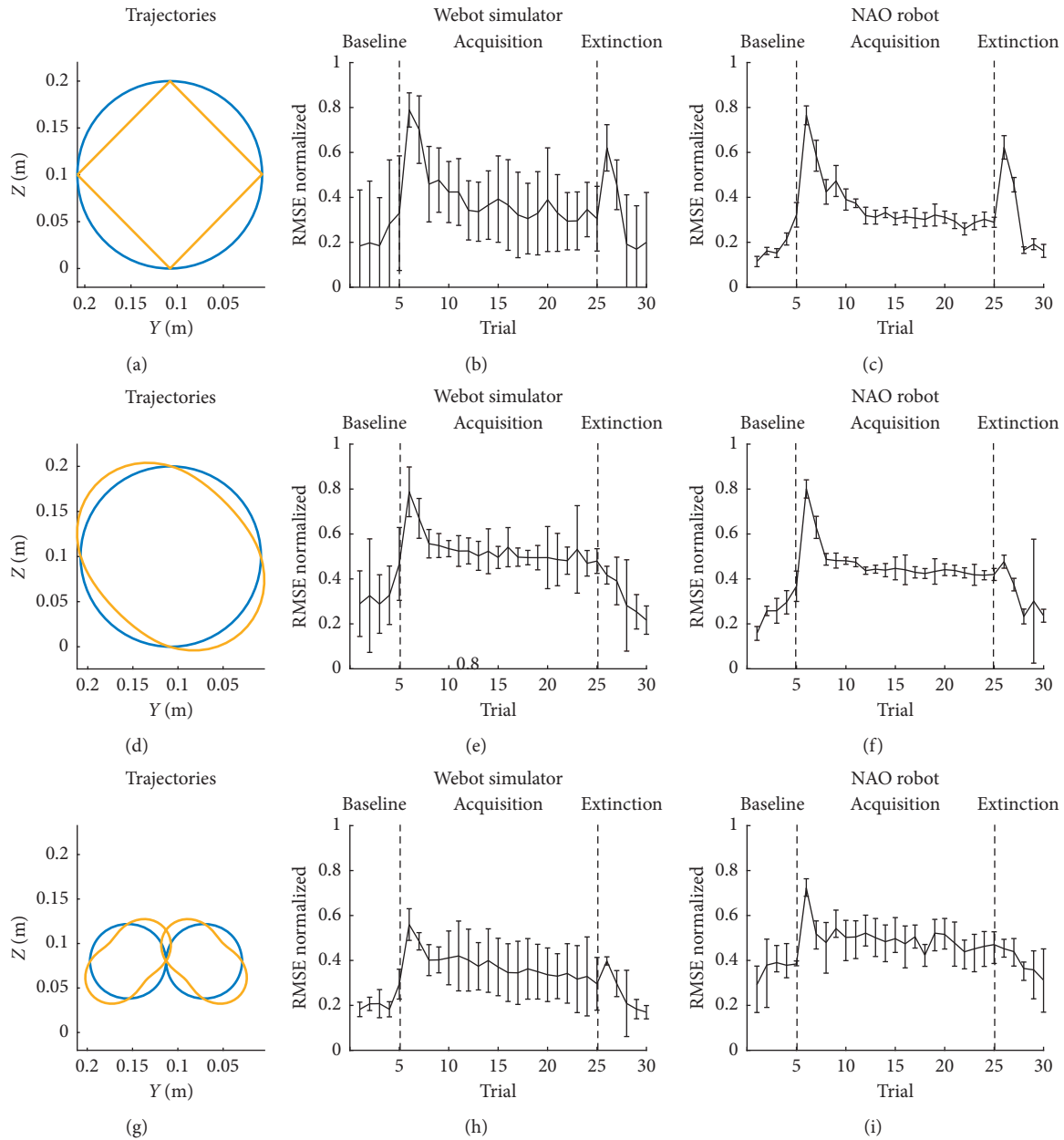


FIGURE 6: Transfer learning performances. (a, d, g) Ideal (blue) and perturbed (yellow) Cartesian trajectories in three cases: square, oval, and infinite, respectively. (b, e, h) Mean and SD of the RMSE computed for 10 tests with Webot simulator for the respective trajectories. (c, f, i) Mean and SD of the RMSE computed for 10 tests with NAO robot for the respective trajectories.

frequency ( $<10$  Hz). However, PC activity is still high, inhibiting the DCN. In the course of the trials the consistent activity of the IO reduces the PC's activity, reaching a point in which the DCN is free to fire as in the last trial of the acquisition (Figure 8(c)) where the PCs are selectively silent and the control signal generated by the DCN rises to compensate for the errors. From the Cartesian trajectories, the effect of the compensation in both the higher and the lower-left parts of the circumference is visible.

In the first trial of the extinction phase (Figure 8(d)), the additional load is removed, but the SNN network is still compensating for the error learned. This behaviour, generating errors in the opposite direction with respect to the

acquisition phase errors, is proper of the cerebellar adaptation and it is called after-effect. In the last trial of the extinction phase (Figure 8(e)), we can observe that the after-effect has been canceled, and the performed trajectory is nearer to the desired one. However, observing the neural activity, it is possible to notice a nonphysiological behaviour. Normally, one would expect the change in sign from the IO to trigger the LTP effect on the PC thus inhibiting again the DCN cells. Here, however, there is a further inhibition of the PCs, this time of the opposite sign, which triggers the response of the DCNs of opposite sign, which were not firing until the beginning of the extinction phase. As a result, the absence of correction is caused by the



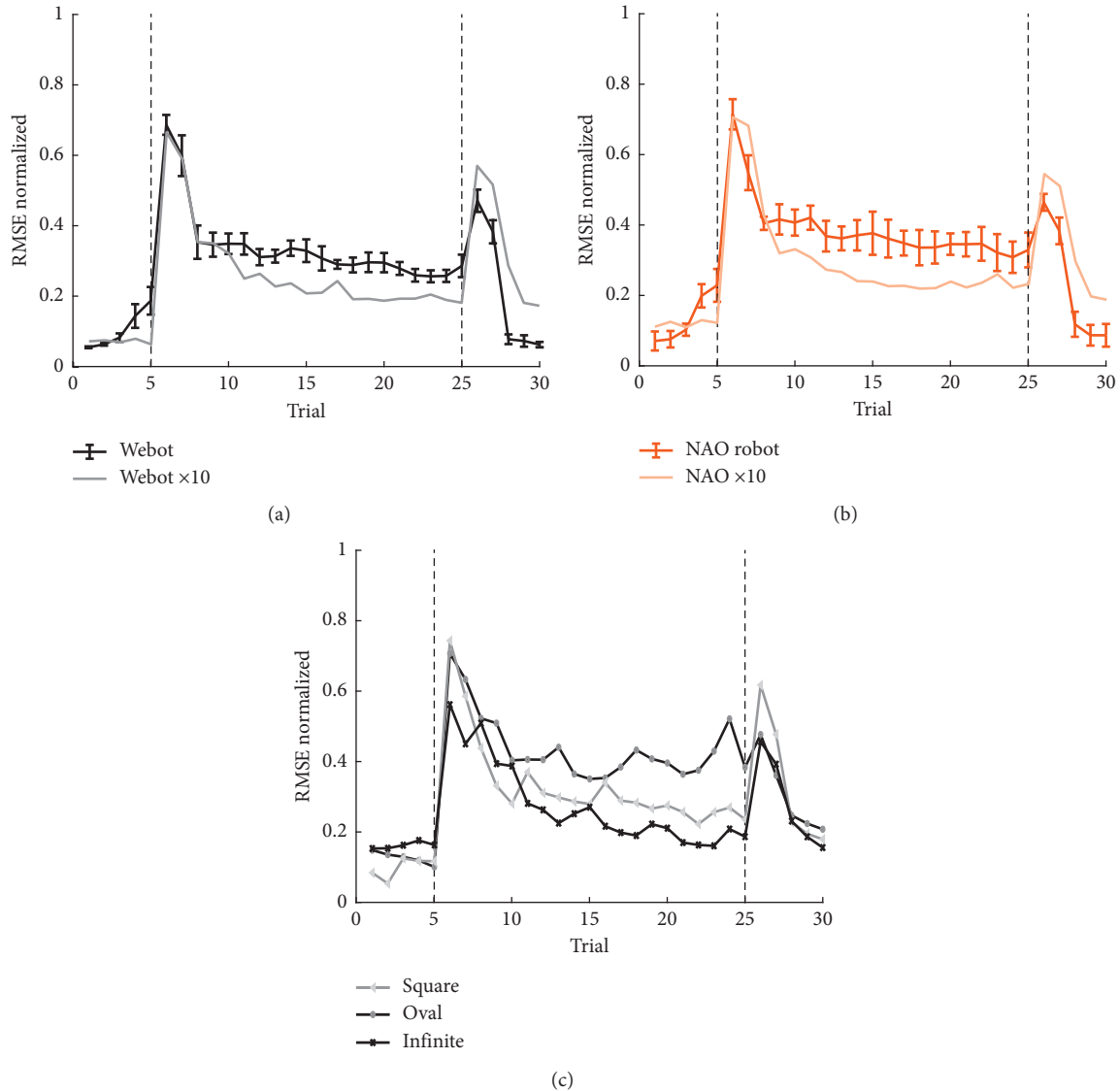


FIGURE 7: RMSE with the enhanced SNN. (a) Mean and SD of the RMSE computed for 10 tests with Webot simulator with the standard network (in black) and a single test with the enhanced tenfold SNN (in grey). (b) Mean and SD of the RMSE computed for 10 tests with NAO robot with the standard network (in orange) and a single test with the enhanced tenfold SNN (in light orange). (c) Mean and SD of the RMSE computed for three single tests performed with Webot simulator and with the three additional trajectories: square (light grey), oval (grey), and infinite (black).

cancellation of two opposite effects instead of a return to the initial DCN silence.

This unexpected result is probably due to the brevity of the protocol (only 20 acquisition trials) and to the cost function used for the parameter tuning, which rewarded higher values of LTD1 with respect to LTP1 for the cortical plasticity. This is visible from the steep slope of the RMSE in the first acquisition trials (Figure 3(c)). The low LTP1 values are not enough to restore the initial state of the network with only 5 trials for the extinction phase, and therefore the optimization process rewarded a configuration where LTD1 compensated for the error in opposite sign with the activity of the DCN of opposite sign (antagonist activity) instead of decreasing the current (agonist) DCN activity. This effect led to the nullification of the

agonist and antagonist neuron activity, with a net output near zero (i.e., near the desired network output during the extinction phase). This result suggests that even with an imbalance in the cortical LTP/LTD ratio, a system can be still able to learn and extinguish a motor adaptation. This hypothesis should be tested by ad hoc experiments where cortical LTP mechanisms have to be blocked or impaired (similar to what was done with mutant mice by Schoneville et al. [37]).

#### 4. Conclusions

In this work, we aimed at the integration of a bioinspired SNN in a NAO robot controller. In particular, the cerebellum has been chosen as the neural structure to emulate

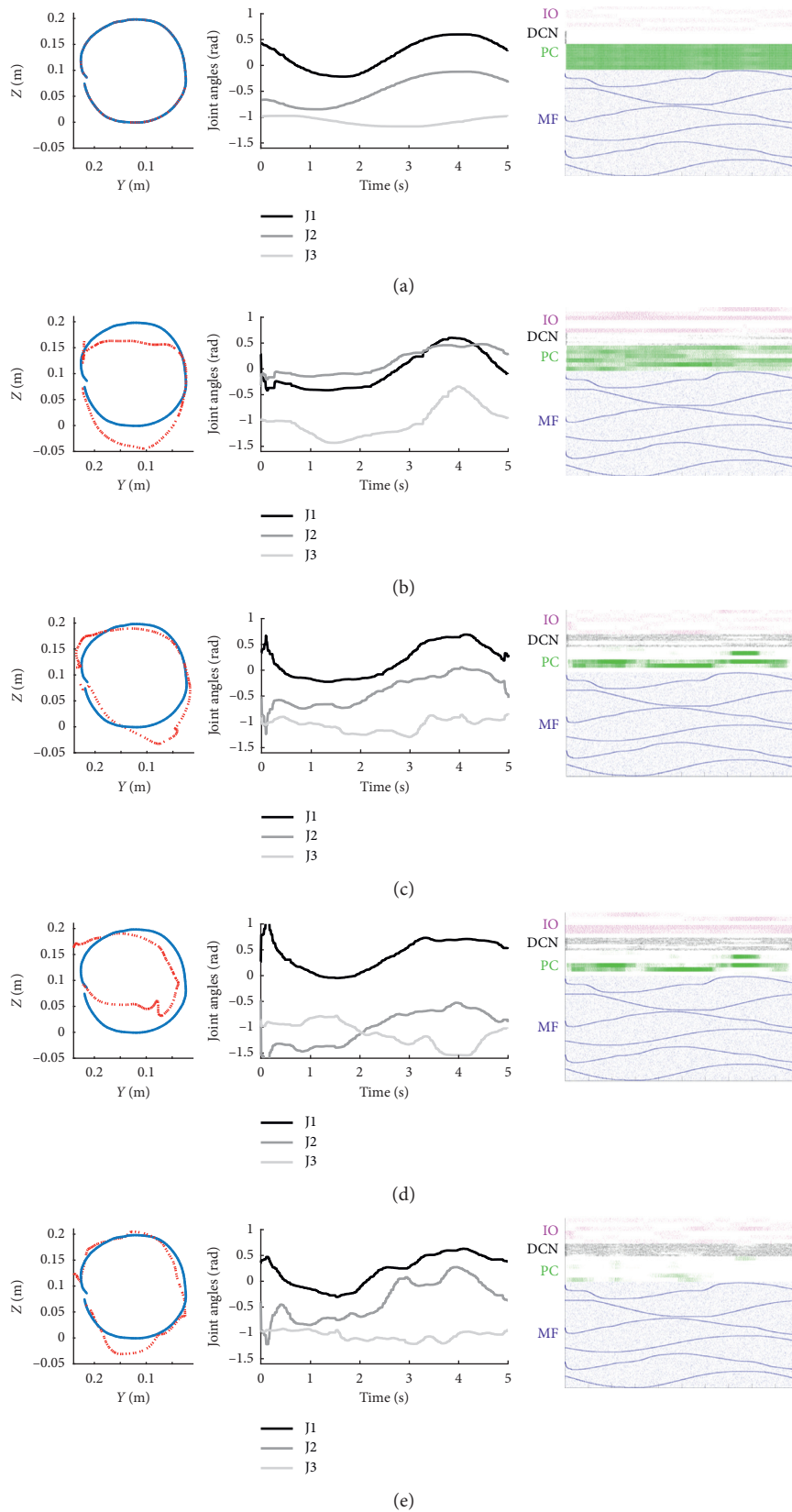


FIGURE 8: Cartesian and joint trajectories with the associated network activity for salient trials. Each row corresponds to a specific salient trial of the protocol: (a) Trial 1, when the test and the baseline phase starts; (b) Trial 6, when the acquisition phase starts; (c) Trial 25, the last trial of the acquisition phase; (d) Trial 26, the first trial of the extinction phase; (e) Trial 30, the last extinction trial and the last trial of the test. In each row, the first column represents the Cartesian trajectory in the  $y$ - $z$  plane, where the blue line is the ideal trajectory (without perturbation, as in Trial 1) and the red line is the actual trajectory performed during that trial. The second column represents the three joint trajectories (joints 1–3 in black, grey, and light grey, respectively) performed during the trial. The third column represents the raster plots of the neural spikes produced by the SNN during that trial (MFs, PCs, DCNs, and IOs in blue, green, black, and magenta, respectively).

for its critical role in motor learning task. The integration of a cerebellar structure in a robot could help in developing new paradigms and ways to perform robotic control in different motor tasks.

Our work was based on previous ones; here, we introduced a larger version of the network, able to control simultaneously three DoFs instead of a single one. This allowed the robot to be tested in a more complex task, using the SNN in an adaptation of the upper limb perturbed reaching protocol, usually used to test the cerebellar learning properties.

We obtained positive results, and the SNN performed well when tested with different trajectories, showing the cerebellar property of transfer learning (i.e., generalizability). The possibility to adapt to different motor task is a fundamental property for the aim of bioinspired robot controllers which will have to deal with different kinds of motor tasks.

One of the main limitations of our network was the low resolution in the output control signal. Tests carried out with a larger network (ten-fold). With this network, the larger number of DCN could produce a smoother output and deal better with small errors.

Further investigation on this network can be performed with the other typical cerebellar paradigms. As in [12], this SNN maintains a general purpose for other cerebellar related tasks. Therefore it would be possible to adapt both the network and the robot to Pavlovian conditioning or vestibulo-ocular reflex protocols.

The increase in the number of controlled joints as well as the good performances obtained with our test, suggests that a larger network would be ideal to tackle this kind of motor tasks. This is especially true if the SNN has to control a real system, in a world rich of unpredictable errors that lowered network performances. The real-time simulation of such large-scale SNN, to develop a real bioinspired controller for a physical robot, could be obtained uniquely by means of highly parallel computing (e.g., GPU) or neuromorphic hardware. This could help in the developing of better strategies of robot control, capable of motor learning and event correlation that would meet practical use in many fields, from the industry to artificial intelligence applications.

## Data Availability

The data generated by the optimization process and by simulations done with the Webot simulator and with the NAO robot have been deposited in the Harvard Dataverse repository. In addition, MATLAB scripts which reproduce all the figures presented in this work are provided (DOI: <https://doi.org/10.7910/DVN/HEPECM>).

## Conflicts of Interest

The authors declare that there are no conflicts of interest regarding the publication of this article.

## Acknowledgments

We are thankful to Eng. Paolo Borzatta of The European House-Ambrosetti for having lent the NAO robot, which

allowed us to perform the robotic experiments presented in this work. This research has received funding from the European Union's Horizon 2020 Framework Programme for Research and Innovation under Specific Grant Agreement nos. 720270 (Human Brain Project SGA1) and 785907 (Human Brain Project SGA2) and by the HBP Partnering Project (CerebNEST).

## Supplementary Materials

A supplementary video is provided, which illustrates the 3D motion task performed by the NAO robot, driven by the SNN controller, in the three experimental phases: 5 baseline trials (in an unperturbed condition); 20 acquisition trials (with a perturbation caused by a virtual load attached at NAO hand); and 5 extinction trials (where the additional load is removed). (*Supplementary Materials*)

## References

- [1] Y.-W. Tseng, J. Diedrichsen, J. W. Krakauer, R. Shadmehr, and A. J. Bastian, "Sensory prediction errors drive cerebellum-dependent adaptation of reaching," *Journal of Neurophysiology*, vol. 98, no. 1, pp. 54–62, 2007.
- [2] M. Kawato and D. Wolpert, "Internal models for motor control," *Novartis Foundation Symposia*, vol. 218, pp. 291–297, 1998.
- [3] G. T. Bartha and R. F. Thompson, "Cerebellum and conditioning," in *The Handbook of Brain Theory and Neural Networks*, pp. 169–172, MIT Press, Cambridge, MA, USA, 1998.
- [4] R. L. de N o, "Vestibulo-ocular reflex arc," *Archives of Neurology and Psychiatry*, vol. 30, no. 2, p. 245, 1933.
- [5] R. Shadmehr, M. A. Smith, and J. W. Krakauer, "Error correction, sensory prediction, and adaptation in motor control," *Annual Review of Neuroscience*, vol. 33, no. 1, pp. 89–108, 2010.
- [6] V. Braitenberg and R. P. Atwood, "Morphological observations on the cerebellar cortex," *Journal of Comparative Neurology*, vol. 109, no. 1, pp. 1–33, 1958.
- [7] D. Marr, "A theory of cerebellar cortex," *Journal of Physiology*, vol. 202, no. 2, pp. 437–470, 1969.
- [8] J. S. Albus, "A new approach to manipulator control: the cerebellar model articulation controller (CMAC)," *Journal of Dynamic Systems, Measurement, and Control*, vol. 97, no. 3, p. 220, 1975.
- [9] J. C. Houk, J. T. Buckingham, and A. G. Barto, "Models of the cerebellum and motor learning," *Behavioral and Brain Sciences*, vol. 19, no. 3, pp. 368–383, 2011.
- [10] D. M. Wolpert, R. C. Miall, and M. Kawato, "Internal models in the cerebellum," *Trends in Cognitive Sciences*, vol. 2, no. 9, pp. 338–347, 1998.
- [11] S. Nolfi and D. Floreano, "Synthesis of autonomous robots through evolution," *Trends in Cognitive Sciences*, vol. 6, no. 1, pp. 31–37, 2002.
- [12] C. Casellato, A. Antonietti, J. A. Garrido et al., "Adaptive robotic control driven by a versatile spiking cerebellar network," *PLoS One*, vol. 9, no. 11, Article ID e112265, 2014.
- [13] A. Antonietti, C. Casellato, J. A. Garrido et al., "Spiking neural network with distributed plasticity reproduces cerebellar learning in eye blink conditioning paradigms," *IEEE Transactions on Biomedical Engineering*, vol. 63, no. 1, pp. 210–219, 2016.

- [14] A. Antonietti, C. Casellato, E. D'Angelo, and A. Pedrocchi, "Model-driven analysis of eyeblink classical conditioning reveals the underlying structure of cerebellar plasticity and neuronal activity," *IEEE Transactions on Neural Networks and Learning Systems*, vol. 28, no. 11, pp. 2748–2762, 2016.
- [15] A. Antonietti, C. Casellato, J. A. Garrido, E. D'Angelo, and A. Pedrocchi, "Spiking cerebellar model with multiple plasticity sites reproduces eye blinking classical conditioning," in *Proceedings of 2015 7th International IEEE/EMBS Conference on Neural Engineering (NER)*, pp. 296–299, IEEE, Montpellier, France, July 2015.
- [16] S. Kuroda, K. Yamamoto, H. Miyamoto, K. Doya, and M. Kawato, "Statistical characteristics of climbing fiber spikes necessary for efficient cerebellar learning," *Biological Cybernetics*, vol. 84, no. 3, pp. 183–192, 2001.
- [17] G. T. Kenyon, "A continuous time model of synaptic plasticity in the cerebellar cortex," in *Computational Neuroscience*, pp. 99–105, Springer US, Boston, MA, USA, 1997.
- [18] J. Maruta, R. A. Smeets, and J. I. Simpson, "Intraburst and interburst signaling by climbing fibers," *Journal of Neuroscience*, vol. 27, no. 42, pp. 11263–11270, 2007.
- [19] M. L. Streng, L. S. Popa, and T. J. Ebner, "Climbing fibers control purkinje cell representations of behavior," *Journal of Neuroscience*, vol. 37, no. 8, pp. 1997–2009, 2017.
- [20] M. Junker, D. Endres, Z. P. Sun, P. W. Dicke, M. Giese, and P. Thier, "Learning from the past: a reverberation of past errors in the cerebellar climbing fiber signal," *PLoS Biology*, vol. 16, no. 8, article e2004344, 2018.
- [21] J. A. Garrido, N. R. Luque, E. D'Angelo, and E. Ros, "Distributed cerebellar plasticity implements adaptable gain control in a manipulation task: a closed-loop robotic simulation," *Frontiers in Neural Circuits*, vol. 7, p. 159, 2013.
- [22] E. D'Angelo, A. Antonietti, S. Casali et al., "Modeling the cerebellar microcircuit: new strategies for a long-standing issue," *Frontiers in Cellular Neuroscience*, vol. 10, p. 176, 2016.
- [23] Z. Gao, B. J. van Beugen, and C. I. De Zeeuw, "Distributed synergistic plasticity and cerebellar learning," *Nature Reviews Neuroscience*, vol. 13, no. 9, pp. 619–635, 2012.
- [24] W. Potjans, A. Morrison, and M. Diesmann, "Enabling functional neural circuit simulations with distributed computing of neuromodulated plasticity," *Frontiers in Computational Neuroscience*, vol. 4, p. 141, 2010.
- [25] E. Ros, R. Carrillo, E. M. Ortigosa, B. Barbour, and R. Agís, "Event-driven simulation scheme for spiking neural networks using lookup tables to characterize neuronal dynamics," *Neural Computation*, vol. 18, no. 12, pp. 2959–2993, 2006.
- [26] M. L. Hines and N. T. Carnevale, "Neuron: a tool for neuroscientists," *Neuroscientist*, vol. 7, no. 2, pp. 123–135, 2016.
- [27] M.-O. Gewaltig and M. Diesmann, "NEST (NEural Simulation Tool)," *Scholarpedia*, vol. 2, no. 4, p. 1430, 2007.
- [28] H. E. Plesser, M. Diesmann, M.-O. Gewaltig, and A. Morrison, "NEST: the neural simulation tool," in *Encyclopedia of Computational Neuroscience*, pp. 1849–1852, Springer, New York, NY, USA, 2015.
- [29] D. Goodman, "Brian: a simulator for spiking neural networks in Python," *Frontiers in Neuroinformatics*, vol. 2, p. 5, 2008.
- [30] K. Rabe, O. Livne, E. R. Gizewski et al., "Adaptation to visuomotor rotation and force field perturbation is correlated to different brain areas in patients with cerebellar degeneration," *Journal of neurophysiology*, vol. 101, no. 4, pp. 1961–1971, 2009.
- [31] O. Donchin, K. Rabe, J. Diedrichsen et al., "Cerebellar regions involved in adaptation to force field and visuomotor perturbation," *Journal of Neurophysiology*, vol. 107, no. 1, pp. 134–147, 2012.
- [32] F. R. Sarlegna, N. Malfait, L. Bringoux, C. Bourdin, and J.-L. Vercher, "Force-field adaptation without proprioception: can vision be used to model limb dynamics?," *Neuropsychologia*, vol. 48, no. 1, pp. 60–67, 2010.
- [33] C. Casellato, A. Antonietti, J. A. Garrido, G. Ferrigno, E. D'Angelo, and A. Pedrocchi, "Distributed cerebellar plasticity implements generalized multiple-scale memory components in real-robot sensorimotor tasks," *Frontiers in Computational Neuroscience*, vol. 9, 2015.
- [34] J. F. Medina, K. S. Garcia, and M. D. Mauk, "A mechanism for savings in the cerebellum," *Journal of Neuroscience*, vol. 21, no. 11, pp. 4081–4089, 2001.
- [35] M. D. Mauk and B. P. Ruiz, "Learning-dependent timing of Pavlovian eyelid responses: differential conditioning using multiple interstimulus intervals," *Behavioral neuroscience*, vol. 106, no. 4, pp. 666–681, 1992.
- [36] J. F. Medina and M. D. Mauk, "Computer simulation of cerebellar information processing," *Nature Neuroscience*, vol. 3, no. 11, pp. 1205–1211, 2000.
- [37] M. Schonewille, A. Belmeguenai, S. K. Koekkoek et al., "Purkinje cell-specific knockout of the protein phosphatase PP2B impairs potentiation and cerebellar motor learning," *Neuron*, vol. 67, no. 4, pp. 618–628, 2010.

## Research Article

# Neurofuzzy c-Means Network-Based SCARA Robot for Head Gimbal Assembly (HGA) Circuit Inspection

Somyot Kiatwanidvilai  and Rawinun Praserttaweelap 

*Department of Electrical Engineering, Faculty of Engineering, King Mongkut's Institute of Technology Ladkrabang, Ladkrabang, Bangkok, Thailand*

Correspondence should be addressed to Somyot Kiatwanidvilai; [somyot.ka@kmitl.ac.th](mailto:somyot.ka@kmitl.ac.th)

Received 27 September 2018; Accepted 29 October 2018; Published 2 December 2018

Academic Editor: Sergio Decherchi

Copyright © 2018 Somyot Kiatwanidvilai and Rawinun Praserttaweelap. This is an open access article distributed under the Creative Commons Attribution License, which permits unrestricted use, distribution, and reproduction in any medium, provided the original work is properly cited.

Decision and control of SCARA robot in HGA (head gimbal assembly) inspection line is a very challenge issue in hard disk drive (HDD) manufacturing. The HGA circuit called slider FOS is a part of HDD which is used for reading and writing data inside the disk with a very small dimension, i.e.,  $45 \times 64 \mu\text{m}$ . Accuracy plays an important role in this inspection, and classification of defects is very crucial to assign the action of the SCARA robot. The robot can move the inspected parts into the corresponding boxes, which are divided into 5 groups and those are “Good,” “Bridging,” “Missing,” “Burn,” and “No connection.” A general image processing technique, blob analysis, in conjunction with neurofuzzy c-means (NFC) clustering with branch and bound (BNB) technique to find the best structure in all possible candidates was proposed to increase the performance of the entire robotics system. The results from two clustering techniques which are K-means, Kohonen network, and neurofuzzy c-means were investigated to show the effectiveness of the proposed algorithm. Training results from the 30x microscope inspection with 300 samples show that the best accuracy for clustering is 99.67% achieved from the NFC clustering with the following features: area, moment of inertia, and perimeter, and the testing results show 92.21% accuracy for the conventional Kohonen network. The results exhibit the improvement on the clustering when the neural network was applied. This application is one of the progresses in neurorobotics in industrial applications. This system has been implemented successfully in the HDD production line at Seagate Technology (Thailand) Co. Ltd.

## 1. Introduction

Robotics and AI especially in neurorobotics play an important role in a number of manufacturing processes because of their fast processing time, good accuracy, intelligence, and high repeatability. In contrary, in the case of manual operation, users must have enough knowledge and experience for working with the processes. The manual operation typically results in inconsistency and cannot control the variations in accuracy and repeatability. Currently, HDD manufacturing processes are under development to be fully autonomous process by the implementation of Artificial Intelligence (AI) into the automation machine to replace the manual process from human. One of the most difficult processes is the visual inspection that has long been

performed by experienced operators. The inspection requires many techniques since the human can naturally deal with the complex problem better than the machine. In addition, the decision of inspection based on the apparent image is still a challenging issue for the intelligent machine. To enhance the performance and accuracy of this process, AI techniques such as neural network, fuzzy system, and unsupervised learning are attempted to apply to the manufacturing, particularly in the visual inspection and control of robotics process. In this study, the HGA circuit inspection which is composed of visual inspection, SCARA robot, and classified boxes is developed. This process starts from the load-in of the incoming part, then the assembly process, and outgoing inspection using robot control. Before the development, the outgoing inspection inspects the FOS

using the 30x microscope via the human eyes and then manually controls the robot to move the part into the corresponding box. This research aims to develop a neuro-fuzzy-based decision technique for this system to automatically control the SCARA robot for the HGA circuit inspection. Vision Pro program, which is a popular tool in image processing, is adopted as the platform of image processing in this study.

As stated in [1], blob detection is a simple but robust technique which was applied in many research studies such as field-programmable gate array with blob, fingertip blob recognition, and optimization [2, 3]. In our work, the simple blob is utilized as the tool for seeking the image features to apply in the next processes of classification and robot control. In general, the unsupervised learning on clustering techniques was widely adopted in many applications, and these were, for example, K-means clustering, K-means combined with PSO for document clustering [4], K-means and fuzzy *c*-means for document clustering [5], K-means applied on image clustering on the graphics processing unit (GPU) platform in [6]. As seen in [6], the developed platform could improve the processing time to be faster than the ordinary techniques. In [7], K-means clustering was applied to the map reduction framework, which is a huge data management to find the best value in the application. In [8], weighted least-squares model-based (WLSMB) with K-means was applied to enhance the ability of classification. Kohonen, which is one of the clustering techniques, has been proved in the application for the 3-dimensional data; in addition, the new model with iteration process could further help to improve the result [9]. The Kohonen map approach has been tested in [10] to solve the estimation problem, and the results showed a better performance than the basic belief assignment. One of the most popular clustering techniques is the fuzzy *c*-means. In terms of data envelopment analysis (DEA), the Kohonen neural network has been applied in [11]. In [12], fuzzy double *c*-means performed clustering well with different datasets on the data clustering and image segmentation. In medical area, the fuzzy *c*-means was applied for the magnetic resonance brain imaging [13], and experimental results exhibited the improved performance. In [14], the neurofuzzy *c*-means clustering algorithm showed the better robustness system on the experiment based on the synthetic datasets with suitable iteration. In the problem of software quality [15], the neurofuzzy *c*-means was applied to the fault prediction problem. Unsupervised and supervised data were tested on the training process in the model. Probability of detection is the key parameter for performance checking. However, the multiple clustering for new feature finding is required for future work. In terms of technology, the driver vigilance predictions on smartwatch-based driver or smart mobile device using neurofuzzy *c*-means were tested [16]. This research combined the measurement data from the sensor and clustering data for prediction. Neurofuzzy *c*-means clustering [17], which applies the Euclidean distance to the clustering technique, was utilized in many applications such as brain tumor in MRI images [18], remote sensing images [19], data clustering with image segmentation [20], and processing time improvement

without performance effect [21]. In [22], branch and bound (BNB) was used for cyclic scheduling of timed Petri nets (TPN) based on the manufacturing systems. The speed of solving the block relocation problem [23] was improved by using the branch and bound algorithm. The concept is to minimize the number of necessary relocations; however, it still requires the future work to support the relaxed constraint. Also, BNB was applied in the model selection [24], the hand-eye calibration [25], the nonlinear integer programming with large-scale problem [26], the multiuser in wireless systems [27], and the maximum of weighted sum-rate for interfering links set [28]. All of the aforementioned techniques and applications were successful in the previous scopes. In this paper, a new improved classification technique for HGA circuit inspection using NFC and branch and bound technique are proposed to enhance the accuracy of inspection and increase the production rate. When the classification or groups of inspecting object has been decided, the action to move the SCARA robot will be the next process to transfer the object to the corresponding box.

## 2. Head Gimbal Assembly

Read and write processes of HDD are occurred from magnetic field changing on the disc. Inside the HDD, it may contain several discs which have a rotational speed during 7,200–15,000 rpm. The summary of the HDD manufacturing process flow is shown in Figure 1. As seen in this figure, the processes of the 30x microscope and slider placing on suspension are the main processes in HDD manufacturing. In addition, HGA is a part of HDD, which holds an electrical circuit inside the slider. Reader, writer, heater, temperature-activated circuits (TA), and microactuator are connected by the electrical circuits. Testing, sorting, and assembly process are the next steps to assemble the HGA stacks.

## 3. Image Processing and Feature Selection

In the automatic visual inspection system, there are two general sections needed to be considered and those are hardware selection and developing software for image processing techniques. In this study, a well design of image processing hardware has been considered and expected to provide good results for imaging. The field of view is a criterion to choose a camera, depending on the size of the slider and the depth of field (DOF) required. DOF is the minimum and maximum of the distance between the camera lens and the object that can yield clear image. Magnification is calculated by the ratio of camera working area and field of view as follows:

$$m = \frac{W_{\text{camera}}}{W_{\text{FOV}}} \quad (1)$$

Based on the careful consideration in selecting the hardware devices, camera, lens, and lighting were selected to achieve enough resolution, high sensitivity, and high contrast ratio with the robustness against the environment change. XC-56 with VGA-class resolution (647 × 493) is

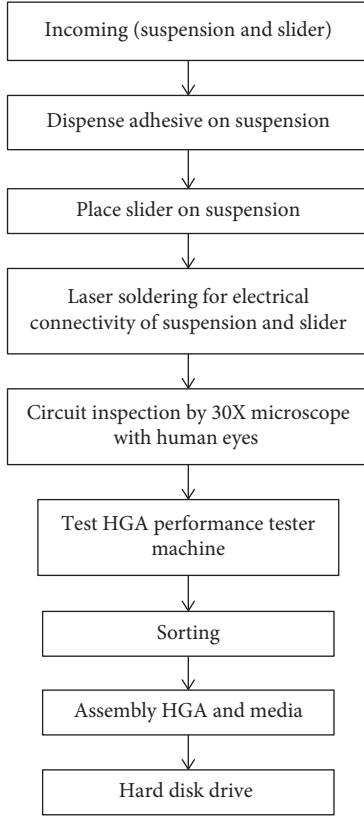


FIGURE 1: HDD manufacturing process flow.

a monochrome camera module in this research. It was mounted with a lens with C-mounting.

In this process, the threshold value was applied to the image transformation from grayscale image to binary image, and the value was specified based on considering the histogram at the preprocessing. As seen in Figure 2, the threshold value, 148.05, on the histogram can separate the group of pixel clearly to maximize the contrast of the captured image. The general image processing technique, i.e., noise elimination, “closing,” was also applied to the image preprocessing.

The feature extraction techniques were applied to find the candidate features on images. In this work, angle, area, inertia, center of mass, acircularity, perimeter, and elongation were determined. Examples of image feature calculation are shown in Equations (2) and (3), and these are area and acircularity, respectively:

$$A = \sum_{i=1}^N x_i y_i, \quad (2)$$

$$C = \frac{P^2}{4\pi A}. \quad (3)$$

To find the best features to be used in the clustering technique, the popular technique, “Branch and Bound (BNB)” was applied. The BNB process starts from the objective function, branches the big problem, and divides it into small group problems. Then, the process analyzes the

bound of problem and removes some results, which cannot provide the best results evaluated from the objective function. The process is repeated until finding the best solution.

#### 4. Clustering and the Proposed Technique

Classification is the method to classify data into particular groups by the model construction. All data are separated into 2 sets: training set and validation set. The training set is used for constructing the clustering structure and parameters, while the validation set is used for verifying the performance of the model. There are a number of techniques applied to clustering such as Euclidean distance. In this research, the performance of the proposed technique neuro-fuzzy *c*-means was investigated in comparison with those from the K-means and Kohonen clustering techniques. The following section describes the brief concept of each clustering technique applied in this research work.

**4.1. K-Means Clustering.** The K-means clustering technique defines the K value to represent the group member of the cluster, and the centroid value on each cluster is set for initial value. A point that shows the minimum summation distance between members and the centroid will be set as the center of that group. The process will be repeated and calculated to perform the new centroid on each cluster until the centroid value is not changed (convergence). Figure 3 shows the steps of the K-means clustering technique.

The Euclidean distance as shown in (4) is used to calculate the K values and the centroid cluster as shown in (5):

$$\text{Min} \left[ D(c_i, x_i) = \sqrt{\sum_{i=1}^n (c_i - x_i)^2} \right], \quad (4)$$

$$c_i = \frac{1}{|S_i|} \sum_{x_i \in S_i} x_i. \quad (5)$$

where  $S$  is the total data point,  $c_i$  is the centroid cluster, and  $x_i$  is the data point.

**4.2. Kohonen Clustering.** The Kohonen clustering starts by assigning the weight randomly and defines the learning rate and the dataset. The minimum distance is the winning node, and then, a new weight will represent each cluster. The new weight is calculated using the following equation:

$$w_{ij, \text{NEW}} = w_{ij, \text{CURRENT}} + \eta(x_{mi} - w_{ij, \text{CURRENT}}), \quad (6)$$

where  $w_{ij, \text{NEW}}$  is the new weight matrix,  $w_{ij, \text{CURRENT}}$  is the current weight matrix,  $x_{mi}$  is the  $n^{\text{th}}$  data, and  $\eta$  is the learning rate. The updating calculation is repeated until the convergence condition is met. The steps of Kohonen mentioned above are shown in Figure 4.

**4.3. Neurofuzzy *c*-Means Clustering.** The neurofuzzy *c*-means clustering starts with an initial value and updates this value until achieving the stopping condition. The

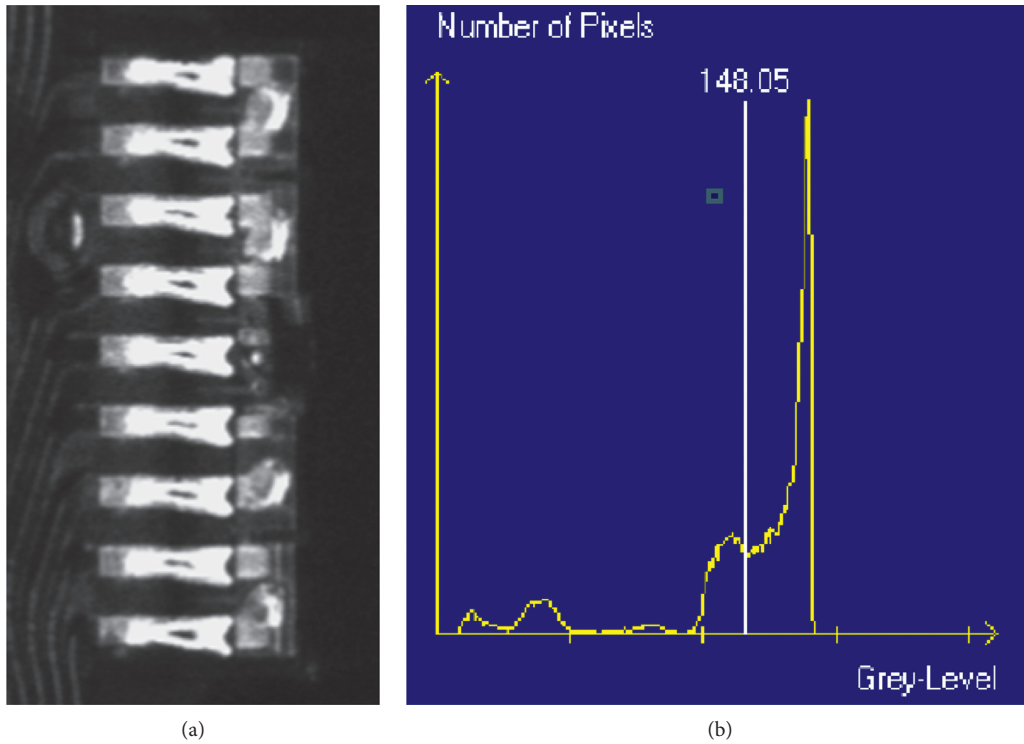


FIGURE 2: (a) Typical image of slider circuit on HGA. (b) Histogram of the typical image [3].

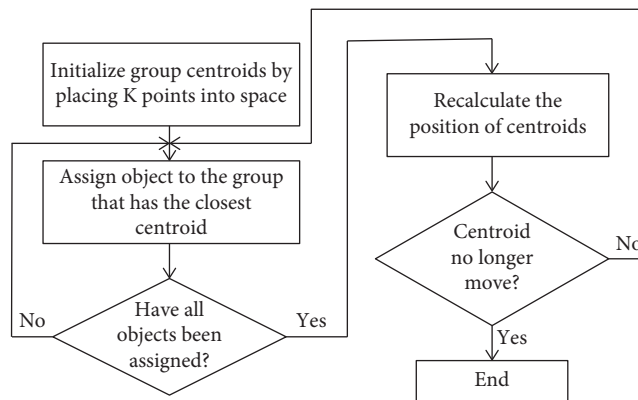


FIGURE 3: K-means clustering.

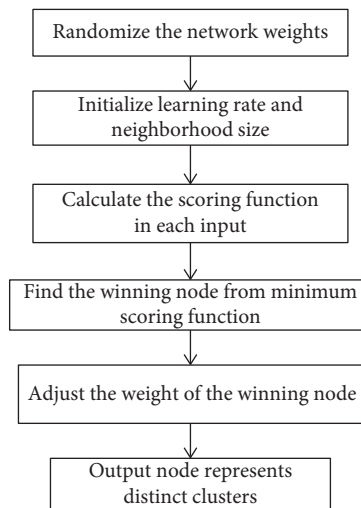


FIGURE 4: Kohonen clustering.



objective function in (7) is used for finding the optimal distance value (smallest value):

$$J_{FCM} = \sum_{i=1}^N \sum_{j=1}^C u_{ij}^m \|x_i - c_j\|^2, \quad (7)$$

where  $u_{ij}$  is the membership function,  $N$  is the number of data,  $c_j$  is the centroid of the clustering, and  $x_i$  is the  $i$ th data. The membership function can be calculated from the following equation:

$$u_{ij} = \frac{1}{\sum_{k=1}^C \left( \frac{\|x_i - c_j\|}{\|x_i - c_k\|} \right)^{(2/(m-1))}}. \quad (8)$$

Clustering centers are given by the normalized and defuzzification technique (8):

$$c_j = \frac{\sum_{i=1}^N u_{ij}^m \cdot x_i}{\sum_{i=1}^N u_{ij}^m}. \quad (9)$$

The steps of the neurofuzzy c-means clustering are shown in Figure 5. As seen in this figure, the objective function has been minimized to achieve the optimal values of the clustering center.

## 5. System Preparation and Experimental Results

The lighting installation system is applied to illuminate the slider circuit and make the best contrast image of the HGA circuit, as shown in Figure 6. The selected type of lighting technique is the diffusion illumination.

The element on the HGA circuit was made from Au (gold). Since the slider is considered as the curve surface with medium reflection, the diffusion lighting technique was applied on this experiment with the ring light (LED) that is suitable because of its long lifetime, flexible application, and high brightness. Lens and camera selection were done by considering the field of view and depth of field. The HGA circuit area is  $45 \times 64 \mu\text{m}$  ( $280 \times 210$ ), and the depth of field is  $80 \mu\text{m}$ . The selected camera is XC-56, having the total pixel as  $659 \times 464$ . Thus, the magnification of the lens can be calculated using (1) as

$$m = \frac{659 \times 464}{280 \times 210} = 5.20. \quad (10)$$

The lens Infinitube FM-75 PL-18 Series with working distance 15 mm was selected. The 5 groups of HGA circuit classification are “good,” “bridging,” “missing,” “burn,” and “no connection” as shown in Figure 7.

Cognex Vision Pro Version 7.2 was applied as the image processing tool, and the master image from the Seagate Company is used for training the neurofuzzy c-means for reference searching (Figure 8).

After the above process, the blob tool is used to separate the region of interest (ROI) and the background with the threshold value. As shown in Figure 2, 40% of the pixels are on the left-hand side, and 60% are on the right-hand side, which can effectively be separated by the threshold value. By

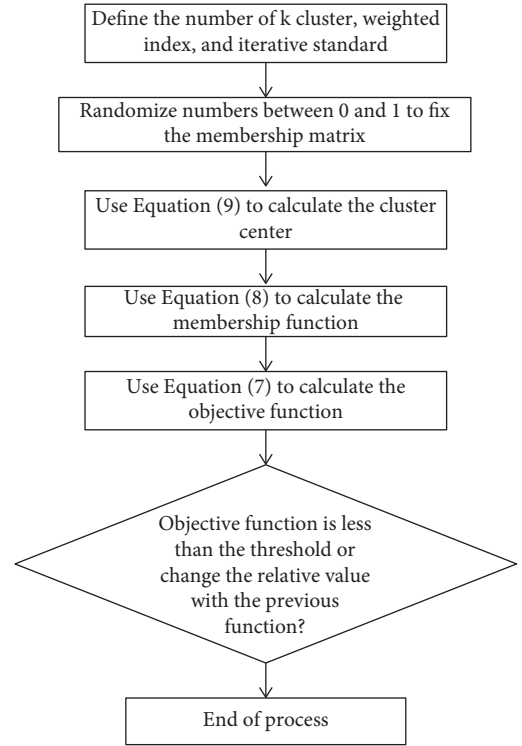


FIGURE 5: Neurofuzzy c-means clustering.

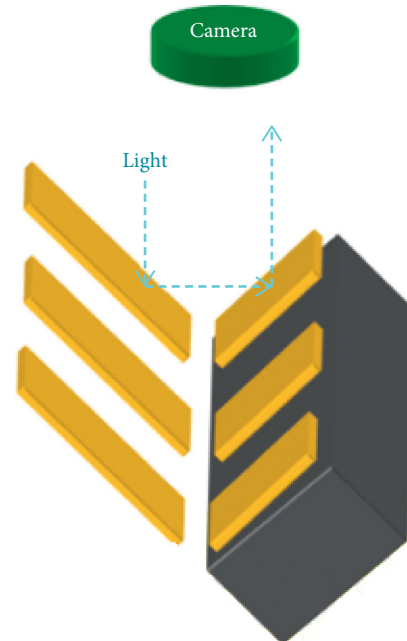


FIGURE 6: Visual inspection system on HGA circuit.

using this relative threshold value, the vision process robustness is gained when the lighting changes.

After preprocessing and blob exporting, 8 image feature variables, which are area, moment of inertia, perimeter, acircularity, center of mass X, center of mass Y, elongation, and angle, were exported. Figure 9 shows preprocessing to define the ROI and using blob to find the interesting

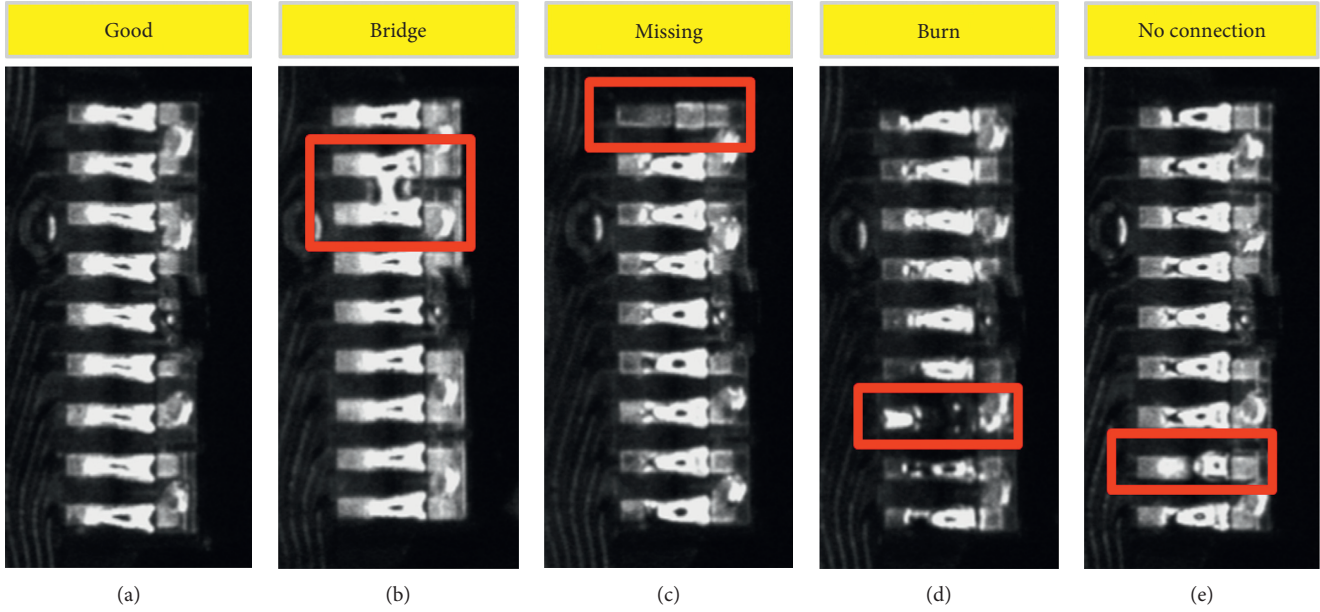


FIGURE 7: Image of HGA circuit in 5 groups: (a) good, (b) bridging, (c) missing, (d) burn, and (e) no connection.

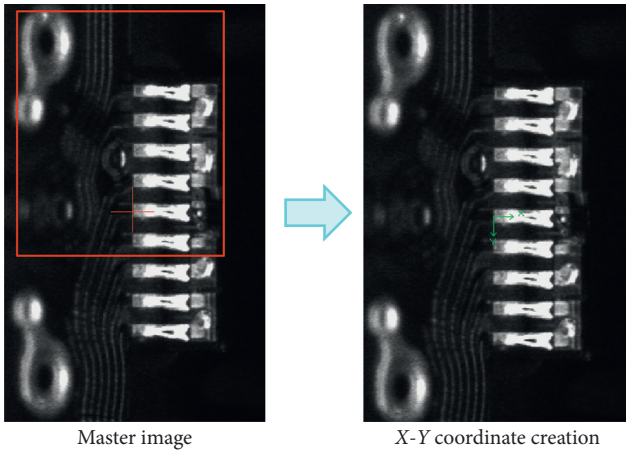


FIGURE 8: Master image and X, Y coordinate creation.



FIGURE 9: Image on blob processing.

features. The objective function in the proposed technique to be utilized in BNB is shown in the following equation:

$$\text{objective function} = \frac{\text{count of correct class index}}{\text{total data}} * 100. \quad (11)$$

Objective function is defined as the percentage of the accuracy when comparing with the results by human eyes

classification using the 30x microscope. The event that obtains the best value (highest objective function value) is the best classification structure for this application. Three clustering techniques were applied to the system which are used to calculate the accuracy sets to find the best classification technique and best features. Through the BNB technique with the 3 classification techniques, 8 image features, 5 classification groups, and 300 samples, the optimal centroid values for 5 predefined classification groups were evaluated. The results show the best accuracy of 99.667% by the neurofuzzy c-means clustering. Figure 10 and Table 1 illustrate the details of the results.

Table 1 shows the top 10 of best accuracy and their details.

The best accuracy can be achieved by the NFC technique, and the 3 image feature variables are area, moment of inertia, and perimeter. Clearly, the design using the neurofuzzy c-means achieves the best performance and can be adopted to command the SCARA robot to classify the quality of the product after slider attachment process.

As shown in Figure 11(a), the red circle is the group of “Good,” the blue circle is “Bridging,” the pink circle is “Missing,” the dark blue circle is “Burn,” and the black circle is “No connection.” Figure 11(b) shows the centroid of each group, and Table 2 shows the optimal centroid of each group.

In the validation process, the selected variables, which are area, moment of inertia, and perimeter, with NFC clustering were adopted. 300 new samples were tested on this validation process, and 3 visual inspection machines, machine no. 17, no. 23, and no. 101, were used to perform the test to ensure the performance on different machines using the same technique. 100 samples per each machine were tested, and it was found that the accuracy achieved on machine no. 17, 23, and 101 were 100%, 99.21%, and 99.12%, respectively. Clearly, the above results show the accuracy

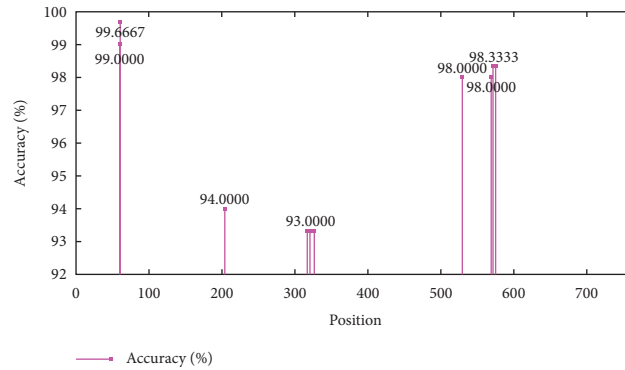


FIGURE 10: Top 10 of best accuracy value chart.

TABLE 1: Top 10 of best accuracy and details.

Order	Axis	Clustering	Best variable
1 (61st)	3	NFC	Area, moment of inertia, perimeter
2 (60th)	3	K-means	Area, moment of inertia, acircularity
3 (517th)	3	NFC	Area, moment of inertia ,perimeter
4 (575th)	3	NFC	Area, center of mass X, perimeter
5 (529th)	2	NFC	Area, acircularity
6 (568th)	3	NFC	Area, moment of inertia, center of mass X
7 (204th)	5	K-means	Area, moment of inertia, center of mass Y, acircularity, perimeter
8 (317th)	3	Kohonen	Area, moment of inertia, elongation
9 (321st)	3	Kohonen	Area, center of mass X, elongation
10 (327th)	3	Kohonen	Area, perimeter, elongation

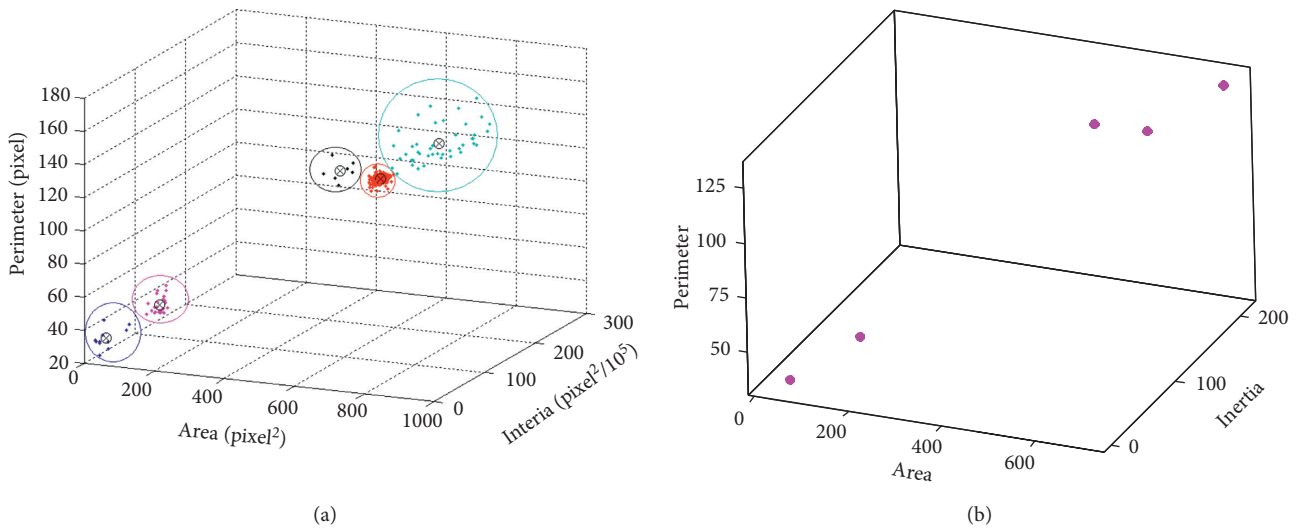


FIGURE 11: Clustering results of best accuracy (61st): (a) clustering groups and data and (b) centroid of each clustering group.

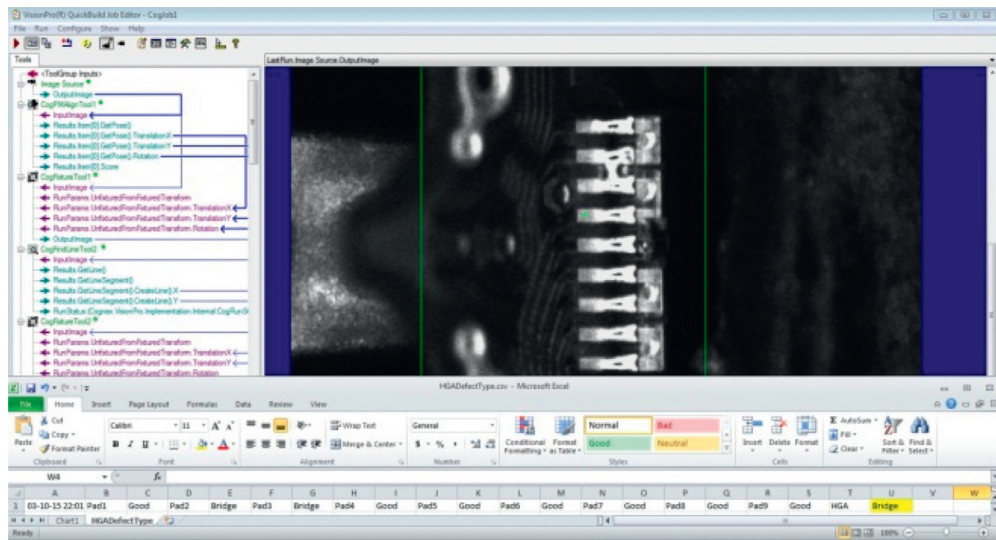
more than 99% (achieved the Seagate’s criteria) for the 3 vision systems, and the technique can be implemented in the actual production line. The example of image construction and real implementation in production line, clustering by NFC, is shown in Figure 12. Also, the SCARA robot in the machine which is used to transfer the slider based on the evaluation results of the NFC is shown in Figure 12(b).

## 6. Conclusion

As shown in the experiment results, the excellent performance with 99.67% accuracy can be achieved from the neurofuzzy c-means clustering with three best features of area, moment of inertia, and perimeter in the training process. The accuracy was investigated by comparing with

TABLE 2: Centroid values of 5 groups from the best clustering results (61st clustering structure).

Group	Area (pixel <sup>2</sup> )	Moment of inertia (pixel <sup>2</sup> /10 <sup>5</sup> )	Perimeter (pixel)
Good	556.7256	200.5483	108.4784
Bridging	708.2615	211.1732	131.5751
Missing	198.7688	11.3017	57.9568
Burn	60.4703	1.8718	36.1733
No connection	474.0023	178.3713	115.4271



(a)



(b)

FIGURE 12: (a) Image processing and CSV file exporting and (b) cleanroom type SCARA robot used in the slider movement machine.

the results from the 30x microscope inspection using human operations. In the validation process, the accuracy of more than 99% with the 3 different vision systems can be achieved. This confirms that the proposed method can be applied to the inspection of the Head Gimbal Assembly circuit classification. In addition, the command to move the slider works well with the SCARA robot to move the HGA stack to the classified boxes correctly.

## Data Availability

The images from the SCARA robot in this article were analyzed in the proposed algorithm which is shown in numerical data as double type. All numerical data are the output from the vision algorithm and tested in the clustering algorithm in the MATLAB program. This research used the image from the SCARA robot for analysis which is included

in the article and as supplied by Seagate Technology (Thailand) Co., Ltd. and so cannot be made freely available. Request for access to these data should be made to Veerasak Phana-ngam via mail (veerasak.phana-ngam@seagate.com).

## Conflicts of Interest

The authors declare that they have no conflicts of interest.

## Acknowledgments

This work was supported by the KMITL Research Funds, RRI, Thailand Research Fund, and Seagate Technology (Thailand) Co., Ltd.

## References

- [1] A. Bochem, R. Herpers, and K. B. Kent, "Hardware acceleration of BLOB detection for image processing," in *Proceedings of 2010 Third International Conference on Advances in Circuits, Electronics and Micro-Electronics*, pp. 28–33, Venice, Italy, July 2010.
- [2] P. Pal, S. Vikas, and P. Raju, "Implementation of multiple fingertip blob recognition on image processing based touchscreen for surface computers," in *Proceedings of 2014 5th International Conference of Confluence The Next Generation Information Technology Summit (Confluence)*, pp. 663–668, Noida, India, November 2014.
- [3] P. C. Ravoor, B. S. Ranjani, and S. R. Rupanagudi, "Optimized fingertip blob recognition for image processing based touchscreens," in *Proceedings of 2012 International Conference on Recent Advances in Computing and Software Systems (RACSS)*, pp. 104–108, New York, NY, USA, April 2012.
- [4] P. Jaganathan and S. Jaiganesh, "An improved K-means algorithm combined with particle swarm optimization approach for efficient web document clustering," in *Proceedings of 2013 International Conference on Green Computing, Communication and Conservation of Energy (ICGCE)*, pp. 772–776, Chennai, India, December 2013.
- [5] V. K. Singh, N. Tiwari, and S. Garg, "Document clustering using K-means, heuristic K-means and fuzzy C-means," in *Proceedings of 2011 International Conference on Computational Intelligence and Communication Systems*, pp. 297–301, Gwalior, India, October 2011.
- [6] J. Sirotkovic, H. Dujmic, and V. Papic, "K-means image segmentation on massively parallel GPU architecture," in *Proceedings of 35th International Convention MIPRO*, pp. 489–494, Opatija, Croatia, May 2012.
- [7] K. D. Garcia and M. C. Naldi, "Multiple parallel mapReduce k-means clustering with validation and selection," in *Proceedings of 2014 Brazilian Conference on Intelligent Systems*, pp. 432–437, Sao Paulo, Brazil, October 2014.
- [8] H. Zifen, Z. Zhaolin, and Z. Yinhuai, "WLSMB halftoning based on improved K-means cluster algorithm using direct binary search," in *Proceedings of 2013 Fifth Conference on Measuring Technology and Mechatronics Automation*, pp. 1310–1313, Hong Kong, China, January 2013.
- [9] S. P. Lim and H. Haron, "Cube Kohonen Self-Organizing Map (CKSOM) model with new equations in organizing unstructured data," *IEEE Transactions on Neural Networks and Learning Systems*, vol. 24, no. 9, pp. 1414–1424, 2013.
- [10] I. Hammami, G. Mercier, A. Hamouda, and D. Jean, "Kohonen's map approach for the belief mass modeling," *IEEE Transactions on Neural Networks and Learning Systems*, vol. 27, no. 10, pp. 2060–2071, 2016.
- [11] L. A. Alves and J. C. C. B. S. Mello, "Weights based clustering in data envelopment analysis using kohonen neural network: an application in brazilian electrical sector," *IEEE Latin America Transactions*, vol. 13, no. 1, pp. 188–194, 2015.
- [12] J. Gu, L. Jiao, S. Yang, and F. Liu, "Fuzzy double C-means clustering based on sparse self-representation," *IEEE Transactions on Fuzzy Systems*, vol. 26, no. 2, pp. 612–626, 2018.
- [13] A. Namburu, S. K. Samayamantula, and S. R. Edara, "Generalised rough intuitionistic fuzzy c-means for magnetic resonance brain image segmentation," *IET Image Processing*, vol. 11, no. 9, pp. 777–785, 2017.
- [14] K. Zhang, W. Kong, P. Liu et al., "Partition region-based suppressed fuzzy C-means algorithm," *Journal of Systems Engineering and Electronics*, vol. 28, no. 5, pp. 996–1008, 2017.
- [15] A. Arshad, S. Riaz, L. Jiao, and A. Murthy, "Semi-supervised deep fuzzy C-mean clustering for software fault prediction," *IEEE Access*, vol. 6, pp. 25675–25685, 2018.
- [16] B. G. Lee, J. H. Park, C. C. Pu, and W. Y. Chung, "Smartwatch-based driver vigilance indicator with kernel-fuzzy-C-means-wavelet method," *IEEE Sensors Journal*, vol. 16, no. 1, pp. 242–253, 2016.
- [17] B. Mohaned, T. Ahmed, H. Lassad, and C. Abdelkader, "A new extension of fuzzy C-means algorithm using non euclidean distance and Kernel methods," in *Proceedings of 2013 International Conference on Control, Decision and Information Technologies (CoDIT)*, pp. 242–249, Hammamet, Tunisia, May 2013.
- [18] Parveen and A. Singh, "Detection of brain tumor in MRI images, using combination of fuzzy C-means and SVM," in *Proceedings of 2015 2nd International Conference on Signal Processing and Integrated Networks (SPIN)*, pp. 98–102, Noida, India, February 2015.
- [19] P. S. S. Aydav and S. Minz, "Generalized fuzzy C-means with spatial information for clustering of remote sensing images," in *Proceedings of 2014 International Conference on Data Mining and Intelligent Computing (ICDMIC)*, pp. 1–5, New Delhi, India, September 2014.
- [20] B. K. Tripathy, A. Tripathy, and K. G. Rajulu, "Possibilistic rough fuzzy C-means algorithm in data clustering and image segmentation," in *Proceedings of 2014 IEEE International Conference on Computational Intelligent and Computing Research (ICIC)*, pp. 1–6, Coimbatore, India, December 2014.
- [21] W. Wang, Y. Zhang, Y. Li, and X. Zhang, "The global fuzzy C-means clustering algorithm," in *Proceedings of 6th World Congress on Intelligent Control and Automation (WCICA)*, pp. 3604–3607, Dalian, China, January 2006.
- [22] C. Jung, H. J. Kim, and T. E. Lee, "A branch and bound algorithm for cyclic scheduling of timed Petri Nets," *IEEE Transactions on Automation Science and Engineering*, vol. 12, no. 1, pp. 309–323, 2014.
- [23] S. Tanaka and K. Takii, "A faster branch-and-bound algorithm for the block relocation problem," *IEEE Transactions on Automation Science and Engineering*, vol. 13, no. 1, pp. 181–190, 2016.
- [24] N. Thakoor and J. Gao, "Branch and bound for model selection and its computational complexity," *IEEE Transactions on Knowledge and Data Engineering*, vol. 23, no. 5, pp. 655–668, 2011.
- [25] J. Heller, M. Havlena, and T. Pajdla, "Globally optimal hand-eye calibration using branch-and-bound," *IEEE Transactions*

- on Pattern Analysis and Machine Intelligence*, vol. 38, no. 5, pp. 1027–1033, 2016.
- [26] H. D. Chiang and T. Wang, “A novel TRUST-TECH guided branch-and-bound method for nonlinear integer programming,” *IEEE Transactions on Systems, Man, and Cybernetics: Systems*, vol. 45, no. 10, pp. 1361–1372, 2015.
- [27] L. T. N. Landau and R. C. de Lamare, “Branch-and-Bound precoding for multiuser MIMO systems with 1-bit quantization,” *IEEE Wireless Communications Letters*, vol. 6, no. 6, pp. 770–773, 2017.
- [28] P. C. Weeraddana, M. Codreanu, M. Latva-aho, and A. Ephremides, “Weighted sum-rate maximization for a set of interfering links via branch and bound,” *IEEE Transactions on Signal Processing*, vol. 59, no. 8, pp. 3977–3996, 2011.

## Research Article

# Multilayer Hybrid Deep-Learning Method for Waste Classification and Recycling

**Yinghao Chu** <sup>1</sup>, **Chen Huang**,<sup>1</sup> **Xiaodan Xie**,<sup>2</sup> **Bohai Tan**,<sup>3</sup> **Shyam Kamal** <sup>4</sup>,  
**and Xiaogang Xiong** <sup>5</sup>

<sup>1</sup>AIATOR Co., Ltd., Block 5, Room 222, Qianwanyilu, Qianhai, Shenzhen, China

<sup>2</sup>Department of Industrial and Systems Engineering, Ohio University, Athens, OH, USA

<sup>3</sup>Sagacity Environment (China) Co. Ltd., A201 Qianwanyilu, Qianhai, Shenzhen, China

<sup>4</sup>Indian Institute of Technology (BHU), Varanasi, Uttar Pradesh 221005, India

<sup>5</sup>Harbin Institute of Technology (Shenzhen), Shenzhen 518055, China

Correspondence should be addressed to Xiaogang Xiong; [xiong@ctrl.mech.kyushu-u.ac.jp](mailto:xiong@ctrl.mech.kyushu-u.ac.jp)

Received 12 August 2018; Accepted 24 September 2018; Published 1 November 2018

Guest Editor: Uma Seeboonruang

Copyright © 2018 Yinghao Chu et al. This is an open access article distributed under the Creative Commons Attribution License, which permits unrestricted use, distribution, and reproduction in any medium, provided the original work is properly cited.

This study proposes a multilayer hybrid deep-learning system (MHS) to automatically sort waste disposed of by individuals in the urban public area. This system deploys a high-resolution camera to capture waste image and sensors to detect other useful feature information. The MHS uses a CNN-based algorithm to extract image features and a multilayer perceptrons (MLP) method to consolidate image features and other feature information to classify wastes as recyclable or the others. The MHS is trained and validated against the manually labelled items, achieving overall classification accuracy higher than 90% under two different testing scenarios, which significantly outperforms a reference CNN-based method relying on image-only inputs.

## 1. Introduction

Globally, the annual solid waste is expected to reach 2.2 billion tonnes by 2025, which would cost \$375.5 billion in waste management [1]. Improper waste management will have enormous adverse impacts on the economy, the public health, and the environment [1]. Municipal solid waste (MSW) recycling has been recognized as the second “most environmentally sound” strategy for dealing with urban waste by the Environmental Protection Agency (EPA) [2]. Effective waste recycling is both economic and environmentally beneficial. It can help in recovering raw resource, preserving energy, mitigating greenhouse gaseous emission, water pollution, reducing new landfills, etc [1, 3–5].

In developing country, MSW recycling relies on household separation via scavengers and collectors who trade the recyclables for profits [6–8]. In developed countries, communities are more involved in recycling program [9]. Several techniques, such as mechanical sorting and chemical sorting, are available in developed countries for

automatic waste sorting [10]. However, there is huge potential to improve waste recycling even in the developed country. The municipal recycling rates of the USA and European Union are around 34% and 50%, respectively, which are significantly lower than the target recycling rate of 75% [5, 11].

The key obstacles to waste recycling include the following: (1) government plan and budget: insufficient government regulation and budget for MSW management; (2) household education: households are unaware of the importance of self-waste recycling; (3) technology: lack of effective recycling technology; and (4) management expense: the high cost of manual waste classification [1, 8, 9].

The recent progress in deep learning has contributed to unprecedented improvements in computer vision. Convolutional neural network (CNN) is one of the most recognized deep-learning algorithms for its wide application in image classification, segmentation, and detection [12–15]. Therefore in this literature, CNN is proposed to perform waste classification.

Awe et al. [16] propose an experimental project using a Faster R-CNN model to classify waste into three categories: paper, recycling, and landfill. This method achieves a mean average precision of 68%. Thung and Yang [17] deployed support vector machine (SVM) and a convolutional neural network (CNN) to classify waste into six categories. It achieves an accuracy rate of 63% for SVM and 23% for CNN. Rad et al. [18] developed a GoogLeNet-based vision application to localize and classify urban wastes. The study claims to have an accuracy rate ranging from 63% to 77% for different waste types. Donovan [19] proposed to use Google's TensorFlow and camera capturing to automatically sort waste objects as compost and recyclable. However, as a conceptual project, there is no experimental result so far. Mittal et al. [20] designed a project to detect whether an image contains garbage or not. This project employs the pretrained AlexNet model and achieves a mean accuracy of 87.69%. However, this project aims at segmenting garbage in an image without providing functions of waste classification.

As reviewed, the automatic classification methodologies available in the literature solely deploy image-based CNN and result in limited accuracy. In this work, we propose a multilayer hybrid method (MHS) to perform waste classification in public areas. Waste images associated with other numerical information measured by sensors are fed into the system. The system can automatically sort the waste item as recyclable or the others. The proposed MHS achieves a mean accuracy higher than 90%, which significantly outperforms reference image-based method.

The specific contributions of the paper are:

- (i) Firstly, this study achieves an excellent accuracy that is useful for in-field applications: the experimental results indicate that MHS achieves an overall accuracy higher than 90%, which outperforms all reference waste classification methods in the literature.
- (ii) Secondly, this study proposes an innovative architecture to simulate the sensory and intellectual process of human inspections. While most of current waste classification methods take images as the sole input, the proposed method makes use of an AlexNet CNN to act as "human eyes" to visualize and extract key image features from its last dense layer. The system also utilizes sensors to act as "ears" and "nose" to detect other numerical feature information, which are barely discussed in the literatures. Ultimately, multilayer perceptrons (MLP) act as a response center (the "human brain") to classify the waste object by consolidating information collected from diverse channels.

The paper is organized as follows: Section 2 introduces the inspected waste items, hardware, and data; Section 3 presents the proposed methods, including CNN, MLP, the multilayer hybrid system, and evaluation metrics; Section 4 presents the results and corresponding discussions; and conclusion are given in Section 5.

## 2. Hardware and Data

This study focuses on wastes found in urban public areas, including parks, street cleaning, landscaping, and other recreational areas. These wastes are mostly disposed of by individual visitors, pedestrians, commuters, and occasionally from commercial events. Unlike industry or household waste, the majority of municipal solid wastes are separated singular items e.g., a singular bottle or a singular lunch box [1].

This study analyzes a total of 50 different waste items that are commonly found in the investigated area [1]. Among which, 40 are recyclable and 10 are the others. The recyclable wastes are grouped into 4 main categories: paper, plastic, metal, and glass; the "others" class consists of fruit/vegetable/plant, kitchen waste, and others (Table 1). Each group is made up of representative items: the paper group, for instance, consists of books, magazines, cups, boxes, etc. Table 2 presents the detailed information of waste items' quantity, corresponded group, and class.

*2.1. Hardware.* The proposed system consists of a high-resolution camera (model 0V9712), a bridge sensor (model HX711AD), and an inductor (model TL-W3MB1 PNP) (Table 3). The system hardware is selected based on availability, low-cost, effectiveness, and easy installation.

The camera captures images of study objects, and the images will be transferred to a PC end via USB 2.0. The bridge sensor is used to measure the weight of study object, and the inductor can detect whether the waste is made from metal or not. To our knowledge, few studies employ sensing systems for waste classification in the literature of MSW, such as applications of medical waste and wastewater sorting using weight, density, and texture detection [3]. Therefore, we propose to deploy the bridge sensor and inductor to facilitate classification of solid waste, particularly for MSW waste. Digital information measured by sensors are received and processed via an Arduino board first. The Arduino board serves as a microcontroller, which can read the outputs from the sensors, convert them into proper numerical form, and then transfer information to the PC end.

In the experiment, the investigated waste items are placed in an enclosed box with a dark grey background. The camera is placed at the upper front-right of the experiment box to maximize the marginal angle of view. Waste objects are rotated for the camera to capture views from different angles, so to simulate a three-dimension effect. The bridge sensor and the inductor are placed directly under the study object to measure their corresponding feature information.

*2.2. Data.* A total of 100 RGB images are captured for each investigated item, and 5000 (50 × 100) images in total are collected in JPG format. Each waste image is grouped with its counterpart numerical feature information as a data



TABLE 1: Representative waste images.

	
Paper	Plastic
	
Metal	Glass
	
Fruit/vegetable/plant	Others

instance, which is then manually labelled as either recyclable or not for training/testing purpose.

To enhance image features and to remove unwanted noise, images captured by the camera are preprocessed under the Keras framework: <http://keras.io/>. The original images (e.g., Figure 1) are  $640 \times 480$  pixels in resolution while the processed images are  $240 \times 240$ . During training, 9 augmented images (Table 4), including image rotation, height/width shifting, size rescaling, zooming etc., are generated for each data instance to enhance the universality of the training model [21].

The training model has been tested twice to validate the system performance. Firstly, each waste item is placed into the system with predefined position and each item is tested for 3 times. A total of 150 ( $50 \times 3$ ) test set are generated for the first test. Secondly, each item is placed randomly in the

system for 3 times and another set of 150 data is generated. In sum, 300 test data are created, and the system classifies each of them as recyclable or the others.

### 3. Method

A multilayer hybrid method (MHS), which consists of several subsystems, is proposed to perform waste classifications. The core of this system includes a convolutional neural network (CNN) and multilayer perceptrons (MLP). Evaluation metrics to access system performance are also discussed in this section.

**3.1. CNN.** Convolutional neural networks (CNN) are widely applied in analyzing visual image [12–15]. Generally, CNN

TABLE 2: Waste item.

Class	Group	Item	Quantity	
Recyclable	Paper	Books	5	
		Cups	5	
		Boxes	4	
	Plastic	General bottles	6	
		Shampoo bottles	4	
		Pen	1	
		Watch	1	
	Metal	Cans	7	
		Key	1	
		Scissor	1	
	Glass	Beer cap	1	
		Bottle	4	
<b>Sum</b>	<b>4</b>	<b>12</b>	<b>40</b>	
Others	Fruit/vegetable/plant	Apple	1	
		Banana	1	
		Carrot	1	
		Cabbage	1	
		Rose	1	
		Others	1	
	Kitchen waste	Egg	1	
		Lunch box	1	
	Others	Trash bag	1	
		Bowl	1	
	<b>Sum</b>	<b>3</b>	<b>10</b>	<b>10</b>

takes images containing investigated items as inputs and classify images into different categories.

CNN is unique in its 3D volumes of a neuron: width, height, and depth. The CNN consists of a series of convolutional layers, polling layers, fully connected layers, and normalization layers [12–15]. The neurons in the convolutional layer will only connect to a small region of the previous layer. In fully connected layers, the activation neurons of the layer are fully connected to all activation neurons in the previous layer. The fully connected function can be expressed as the following forward and backward propagation rules in mathematical form:

$$\begin{aligned}
 X_i^{L+1} &= \sum_j W_{ji}^{L+1} X_j^L, \\
 g_i^L &= \sum_j W_{ji}^{L+1} g_j^{L+1},
 \end{aligned}
 \tag{1}$$

where  $X_i^L$  and  $g_i^L$  represent the activation and the gradient of neurons  $i$  at layer  $L$  and  $W_{ji}^{L+1}$  is the weight connecting neurons  $i$  at layer  $L$  to neurons  $j$  at layer  $L + 1$ .

The capability of CNN can be controlled by varying dimensional parameters and local architecture structure [12]. In recent years, different CNN architecture variations emerge [12, 15]. In considering the computational cost and in-field application limitations, AlexNet [12] is employed in this work.

**3.2. AlexNet.** AlexNet [12] came to the spot in the 2012 ImageNet Challenge (ILSVRC) by significantly reducing the image classification top-5 error from 26% to 15.3%. It is well-recognized for its highly capable architecture.

AlexNet contains 8 learning layers: the first five convolutional followed by three fully connected layers. The output of the last layer is fed into the 1000-way softmax which can create 1000 class labels. The kernels of the second, fourth, and fifth layers are connected to those kernels in previous layers sharing the same GPU. Kernels in the third layer, however, are fully connected to the kernels in the second layer. Response-normalization layer is associated with the first and second layers. Max-pooling layers are placed after both response-normalization layers and the fifth layer. The ReLU nonlinearity is associated with each learning layer. The neurons in the fully connected layers are connected to all neurons in the previous layer, with 4096 neurons each [12].

In this work, the network is constructed with following details:

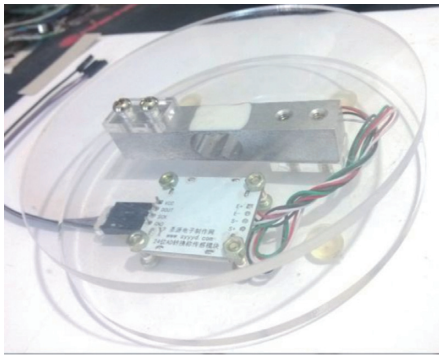
- (i) Layer 0: input image of size  $240 \times 240$
- (ii) Layer 1: convolution with 96 filters, size  $11 \times 11$ , stride 4
- (iii) Layer 2: max-pooling with a size  $3 \times 3$  filter, stride 2
- (iv) Layer 3: convolution with 256 filters, size  $5 \times 5$ , stride 1
- (v) Layer 4: max-pooling with a size  $3 \times 3$  filter, stride 2
- (vi) Layer 5: convolution with 384 filters, size  $3 \times 3$ , stride 1
- (vii) Layer 6: convolution with 384 filters, size  $3 \times 3$ , stride 1
- (viii) Layer 7: convolution with 256 filters, size  $3 \times 3$ , stride 1
- (ix) Layer 8: max-pooling with a size  $3 \times 3$  filter, stride 2
- (x) Layer 9: fully connected with 512 neurons
- (xi) Layer 10: fully connected with 512 neurons
- (xii) Layer 11: fully connected with 22 neurons

The number of the neurons in the last layers is set to 22 to equalize the number of waste categories discussed in Section 2. An additional Layer 12, which contains 1 neuron with sigmoid activation function (recyclable as 1 and others as 0), is used during training. This layer is then removed when integrated into the multilayer hybrid system that ingests the 22 outputs from Layer 11 as image features. To do so, the CNN reduces the high dimension image to low-dimensional representation with robust features only. Also, it reserves the information of important identity features which may be wrapped by final classification [22]. This application is extensively adopted in human face verification problem and face recognition as a binary classification problem.

**3.3. MLP.** Multilayer perceptrons (MLP), one of the most established deep-learning structures for nonlinear classification and regression, are frequently used for modeling and forecasting [23–26].

Neurons, which are placed in layers, are the basic processing elements of MLP. The layers between the first layer (inputs) and the last layer (outputs) are called hidden layers. The MLP employed in this work has 1 hidden layer with 10 neurons as suggested in [25] that this network is able

TABLE 3: Experiment sensors.



Bridge sensor



Inductor



FIGURE 1: Example of the original image.

to fit any continuous function. Neurons on each layer sum the weighted inputs, add a bias to the sum, and then apply an activation function to process the sum and compute the outputs. The signal processing of neurons can be mathematically expressed as

$$Y_i = \int \left( \sum_{j=1}^M (W_{ij}X_j + \beta_{ij}) \right), \quad (2)$$

where  $Y_i$  is the output of the  $i^{\text{th}}$  neuron on current layer,  $w_{ij}$  and  $\beta_{ij}$  are the weight and bias of the  $j^{\text{th}}$  input on the  $i^{\text{th}}$  neuron,  $M$  is the number of inputs,  $X_j$  is  $j^{\text{th}}$  output from the previous layer, and  $f$  is the activation function, which is a sigmoid function in this work.

$$f(y) = \frac{1}{1 + e^{-y}}. \quad (3)$$

**3.4. Multilayer Hybrid System.** The multilayer hybrid system (MHS) developed in this work simulates human sensory and intelligence process system. This MHS is a combination of several interdependent subsystems, including: (1) image system (2) sensor system and (3) the central back-end classification system.

Figure 2 illustrates the multilayer hybrid system with three interacting subsystems and their associated components. The arrows indicate the processing flow and interaction of subsystems.

When a waste item is received into the hybrid system, the camera and sensors are activated to observe the item. The imaging system consists of a camera to capture an image, which is analyzed by the CNN. The sensor system, simultaneously, functions to obtain numerical information from the objects. The ultimate results (binary output) are obtained using MLP system, whose inputs are the 22 outputs from the CNN and the numerical information from sensors. In this respect, MLP system can be trained independently from CNN model, and the weight and bias parameters of CNN model can be kept unaffected. On the other hand, as the outputs of CNN are the inputs for MLP, these two models actually function simultaneously to generate the binary classification results.

**3.5. Evaluation Metrics.** Each classification prediction by the proposed system is compared to the manually classified label, which is set as the “truth”. The confusion matrix shown in Table 5 quantifies the hits and misses of the automatic classification system. A CNN-only model with exactly the same structure discussed above is trained and evaluated as a reference model.

The system performance is evaluated with accuracy, precision, and recall. The accuracy of classification is defined as the percentage of images that are correctly classified:

$$\text{accuracy} = \frac{(TP + TN)}{(TP + TN + FP + FN)} \times 100\%. \quad (4)$$

Precision, therefore, represents the correctness of classification prediction systems.

$$\text{Precision} = \frac{TP}{(TP + FP)} \times 100\%. \quad (5)$$

Recall represents the effectiveness of classification prediction systems.

$$\text{Recall} = \frac{TP}{(TP + FN)} \times 100\%. \quad (6)$$

Incorporating precision and recall can reduce the bias forecasting caused by the unbalanced dataset: the minority class is harder to learn and the model tends to over forecast the majority class with highly skew data [26].

TABLE 4: Example of images generated by the augmentation algorithm.

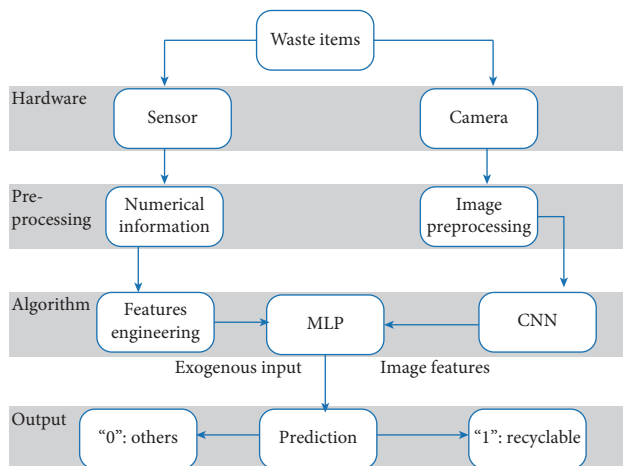
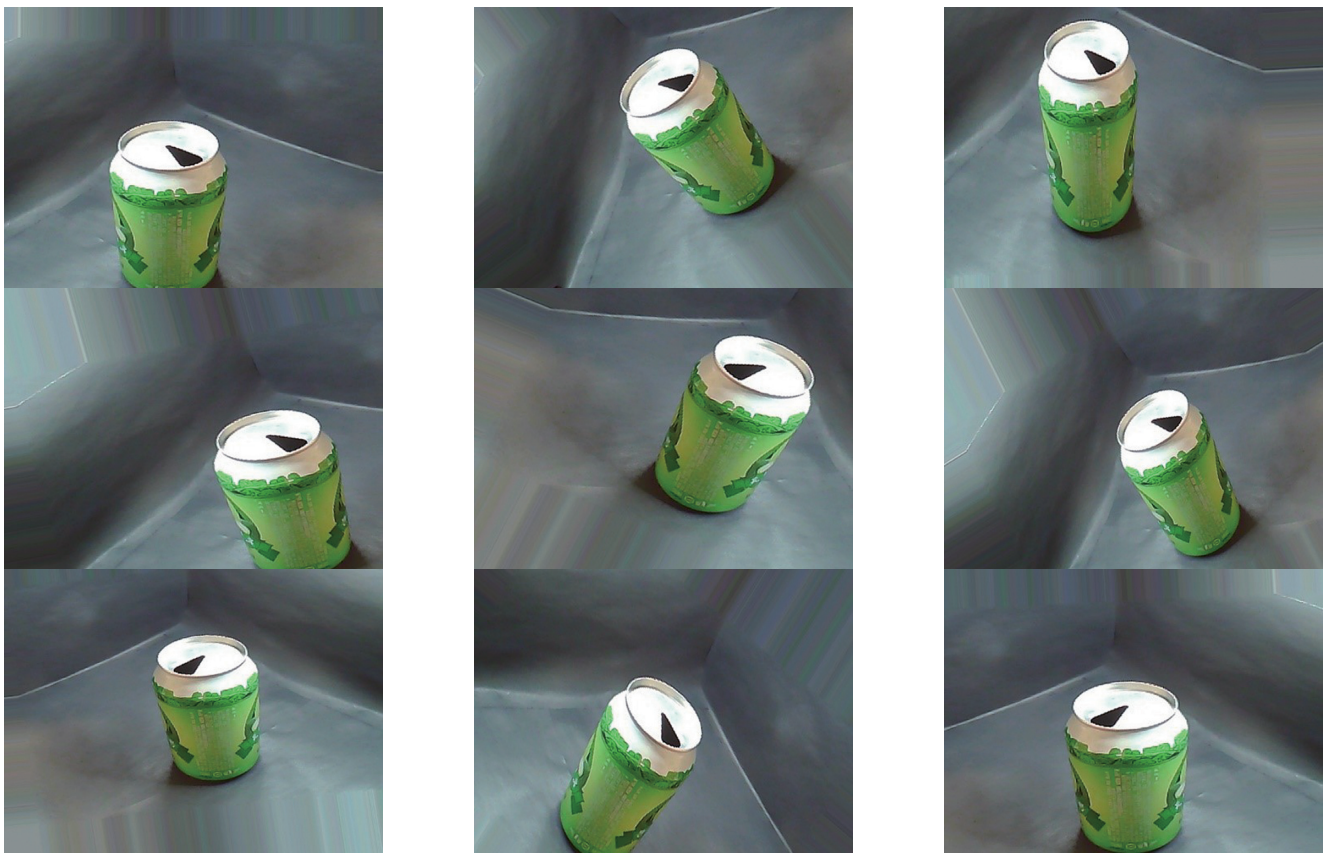


FIGURE 2: Multilayer hybrid system (MHS).

#### 4. Result and Discussion

The MHS model, which is trained using 5000 data instances, is evaluated under two different scenarios: the item is placed with fixed and random orientations. The model performances are compared with a CNN model that takes the images as the only input. The classification results from each model are presented in Table 6.

TABLE 5: Confusion matrix of automatic waste classification for each category.

Automatic classification	Manual classification	
	Recyclable	Others
Recyclable	True positive (TP)	False positive (FP)
Others	False negative (FN)	True negative (TN)

The evaluation results presented in Table 6 indicate that MHS significantly outperforms CNN-only model in terms of all three matrices (accuracy, precision, and recall), particularly for the “others” category.





MHS achieves accuracy rates above 90% for both the first and second tests, which are 10% higher than the CNN-only model (Table 6). The MHS model also achieves higher precision rate of 98.5%, 97.1% to 88.6%, 85.9%, respectively, indicating MHS model’s effectiveness in predicting recyclable items. In addition, the MHS model shows great performance in recall (99% and 92%, respectively, for the first and second tests), showing that MHS is highly sensitive in identifying dedicated recyclable waste items.

The following tables display three sets of representative items returning from testing results. Table 7 represents items that are correctly classified by both MHS and CNN; Table 8 represents items that are correctly classified by the MHS but incorrectly classified by the CNN. Table 9 consists of items with low classification accuracy in both models.

TABLE 6: Confusion matrices for different classification models.

Evaluation metrics	MHS model		CNN model	
	1 <sup>st</sup> test	2 <sup>nd</sup> test	1 <sup>st</sup> test	2 <sup>nd</sup> test
Accuracy (%)	98.2	91.6	87.7	80.0
Precision (%)	98.5	97.1	88.6	85.9
Recall (%)	99.3	92.3	96.8	89.2

TABLE 7: Representative waste items that are correctly classified by both MHS and CNN.

MHS	CNN		
✓	✓		
			

It can be noticed that both MHS and CNN perform well when investigated items have strong image features (Table 7). However, CNN performs poorly when waste items lack distinctive image features, especially for “other” waste.

For instance, the images of beer cap and the transparent box (Table 8) are weak to be distinguished from the experiment background. It is difficult for the CNN to extract their imagery features in training, thus fail in testing. The cabbage item is irregular in appearance showing different figures for different orientations of placement. The CNN model itself is not sufficient enough to construct the feature patterns for accurate classification. The egg’s figure, on the other hand, is too simple to transfer sufficient information for training model resulting in a limited performance.

CNN relies on image information only, and if the study items are weak in imagery features, its classification performance will be adversely affected. MHS can address the problem by integrating both image and other feature information. In situations where the image information is insufficient, MHS is able to take advantages of other useful feature to make the most appropriate classification decision. Nevertheless, for items whose image features and other

numerical features are weak, their MHS classification error may increase. For instance, the MHS accuracy rate of the cup is about 60% (Table 9). After inspecting each individual misclassification case, we found that the major reason to cause these errors is that these objects have cylinder shapes, which are usually misclassified as bottles that are recyclable.

## 5. Conclusion

An automatic classification system based on multilayer hybrid deep learning (MHS) is proposed to classify disposal of waste in the urban public area. The system simulates human sensory and intelligence process system by deploying a high-resolution camera together with multiple functional sensors. The multilayer hybrid method consists of three interdependent sub-systems, including an image processing system, a numerical sensor system, and a multilayer perceptrons (MLP) system. The image processing system deploys AlexNet CNN to extract waste imagery information as inputs for the MLP. The sensor system aims at measuring other waste features as numerical input for MLP. The MHS is used to automatically classify the waste item as either recyclable or the others by consolidating information from both image and sensory channels.

TABLE 8: Representative waste item that are correctly classified by the MHS but incorrectly classified by the CNN.





MHS	CNN		
✓	X		
			

TABLE 9: Representative waste item with low accuracy in MHS and CNN.

MHS	CNN		
X	X		

A total of 50 waste items are used to evaluate the performance of MHS, which is also compared with a CNN-only model that only takes images as input. The result indicates that the MHS achieves a significantly higher classification performance: the overall performance accuracies are 98.2% and 91.6%, (the accuracy of the reference model is 87.7% and 80.0%) under two different testing scenarios.

This study demonstrates the potential of the proposed MHS in improving waste classification's efficiency and effectiveness. In considering the continually increased volume of waste globally and the urgent requirements for environmentally friendly waste processing, the proposed MHS is both economically and environmentally beneficial.

### Data Availability

The image and numerical data used to support the findings of this study are available from the corresponding author upon request.

### Conflicts of Interest

The authors declare that they have no conflicts of interest.

### Acknowledgments

The authors gratefully acknowledge the support provided by Shiwei Qin, Xin Zhao, and Xianyue Feng who assisted in the

collection of waste items, hardware preparation, data analysis, and algorithm optimization. The authors also gratefully acknowledge the technique advice from Yuanhui Tang and the laboratory and platform support from Dongguan University of Technology. This work was partly financially supported by the National Natural Science Foundation of China (Grant no. 11702073), Shenzhen Key Lab Fund of Mechanisms and Control in Aerospace (Grant no. ZDSYS201703031002066), and the Basic Research Plan of Shenzhen (Grant nos. JCYJ20170413112645981 and JCYJ20170811160440239).

## References

- [1] D. Hoornweg and P. Bhada-Tata, *What a Waste: A Global Review of Solid Waste Management*, World Bank, Washington, DC, USA, 2012.
- [2] R. E. Sanderson, *Environmental Protection Agency Office of Federal Activities' Guidance on Incorporating EPA's Pollution Prevention Strategy into the Environmental Review Process*, EPA, Washington, DC, USA, 1993.
- [3] P. T. Williams, *Waste Treatment and Disposal*, Wiley, West Sussex, UK, 2005.
- [4] T. H. Christensen, E. Gentil, A. Boldrin, A. W. Larsen, B. P. Weidema, and M. Hauschild, "C balance, carbon dioxide emissions and global warming potentials in LCA-modelling of waste management systems," *Waste Management & Research*, vol. 27, no. 8, pp. 707–715, 2009.
- [5] US EPA, *Facts and Figures about Materials, Waste and Recycling*, EPA, Washington, DC, USA, 2018, <https://www.epa.gov/facts-and-figures-about-materials-waste-and-recycling/advancing-sustainable-materials-management-0>.
- [6] O. Kofoworola, "Recovery and recycling practices in municipal solid waste management in Lagos, Nigeria," *Waste Management*, vol. 27, no. 9, pp. 1139–1143, 2007.
- [7] J. Tai, W. Zhang, Y. Che, and D. Feng, "Municipal solid waste source-separated collection in China: a comparative analysis," *Waste Management*, vol. 31, no. 8, pp. 1673–1682, 2011.
- [8] A. M. Troschinetz, *Twelve Factors Influencing Sustainable Recycling of Municipal Solid Waste in Developing Countries*, Michigan Technological University, Houghton, MI, USA, 2005.
- [9] N. Kollikkathara, H. Feng, and E. Stern, "A purview of waste management evolution: special emphasis on USA," *Waste Management*, vol. 29, no. 2, pp. 974–985, 2009.
- [10] S. Al-Salem, P. Lettieri, and J. Baeyens, "Recycling and recovery routes of plastic solid waste (PSW): a review," *Waste Management*, vol. 29, no. 10, pp. 2625–2643, 2009.
- [11] European Environment Agency, *Waste Recycling*, 2018, <https://www.eea.europa.eu/data-and-maps/indicators/waste-recycling-1/assessment>.
- [12] A. Krizhevsky, I. Sutskever, and G. E. Hinton, "ImageNet classification with deep convolutional neural networks," in *Proceedings of Neural Information Processing System Conference*, Lake Tahoe, CA, USA, December 2012.
- [13] P. Sermanet, D. Eigen, X. Zhang, M. Mathieu, R. Fergus, and Y. Lecun, "OverFeat: integrated recognition, localization and detection using convolutional networks," in *Proceedings of International Conference on Learning Representations*, Banff, Canada, April 2014.
- [14] M. D. Zeiler and R. Fergus, "Visualizing and understanding convolutional neural networks," in *Proceedings of 13th European Conference on Computer Vision (ECCV)*, Zurich, Switzerland, September 2014.
- [15] K. He, X. Zhang, S. Ren, and J. Sun, "Deep residual learning for image recognition," in *Proceedings of Conference on Computer Vision and Pattern Recognition*, Las Vegas Valley, NV, USA, June 2016.
- [16] O. Awe, R. Mengistu, and V. Sreedhar, "Smart trash net: waste localization and classification," arXiv Preprint, 2017.
- [17] G. Thung and M. Yang, "Classification of trash for recyclability status," arXiv Preprint, 2016.
- [18] M. S. Rad, A. V. Kaenel, A. Droux et al., "A computer vision system to localize and classify wastes on the streets," in *Computer Vision System*, pp. 195–204, Springer, Cham, Switzerland, 2017.
- [19] J. Donovan, *Auto-Trash Sorts Garbage Automatically at the TechCrunch Disrupt Hackathon*, 2018, <https://techcrunch.com/2016/09/13/auto-trash-sorts-garbage-automatically-at-the-techcrunch-disrupt-hackathon/>.
- [20] G. Mittal, K. B. Yagnik, M. Garg, and N. C. Krishnan, "SpotGarbage: smartphone app to detect garbage using deep learning," in *Proceedings of the 2016 ACM International Joint Conference on Pervasive and Ubiquitous Computing*, New York, NY, USA, 2016.
- [21] S.-T. Bow, *Pattern Recognition and Image Preprocessing*, Taylor & Francis, Abingdon, UK, 2002.
- [22] Y. Taigman, M. Yang, M. Ranzato, and L. Wolf, "DeepFace: closing the gap to human-level performance in face verification," in *Proceedings of Computer Vision and Pattern Recognition (CVPR), 2014 IEEE Conference*, Columbus, OH, USA, 2014.
- [23] S. Haykin, *Neural Networks: A Comprehensive Foundation*, Prentice-Hall, Inc., Upper Saddle River, NJ, USA, 2008.
- [24] C. M. Bishop, "Neural networks and their applications," *Review of Scientific Instruments*, vol. 65, no. 6, pp. 1803–1832, 1994.
- [25] M. Nielsen, *Neural Networks and Deep Learning*, Determination Press, 2015.
- [26] F. Provost, "Machine learning from imbalanced data sets 101," in *Proceedings of AAAI'2000 Workshop on Imbalanced Data Sets*, Menlo Park, CA, USA, 2000.